Integrated optical isolators and circulators on an InP membrane platform

Integrated optical isolators and circulators on an InP membrane platform

PROEFSCHRIFT

ter verkrijging van de graad van doctor aan de Technische Universiteit Eindhoven, op gezag van de rector magnificus Prof.dr.ir. F.P.T. Baaijens, voor een commissie aangewezen door het College voor Promoties, in het openbaar te verdedigen op dinsdag 20 december 2022 om 11:00 uur

door

Rui Ma

geboren te Baoji, China

Dit proefschrift is goedgekeurd door de promotoren en de samenstelling van de promotiecommissie is als volgt:

voorzitter:	prof.dr.ir. A.B. Smolders
1e promotor:	dr. J.J.G.M. van der Tol
co-promotor:	dr. Y. Jiao
leden:	prof.dr. B. Koopmans
	prof.dr.ir. D.A.I. Marpaung (Universiteit Twent)
	dr. B. Dagens (Université Paris-Saclay)
	prof.dr. K.A. Williams
adviseur:	dr. Y. Shoji (Tokyo Institute of Technology)

Het onderzoek of ontwerp dat in dit proefschrift wordt beschreven is uitgevoerd in overeenstemming met de TU/e Gedragscode Wetenschapsbeoefening.

Integrated optical isolators and circulators on an InP membrane platform by Rui Ma.

Keywords: Photonic integrated circuits, Indium Phosphide, Magneto-optic materials, Optical isolators, Optical circulators.

A catalogue record is available from the Eindhoven University of Technology Library.

ISBN: 978-90-386-5595-6

This work is part of the research programme Zwaartekracht, which is financed by the Dutch Research Council (NWO).

Typeset using LaTeX, printed in the Netherlands.

Summary

Integrated optical isolators and circulators on an InP membrane platform

With the rapid growth in global data networks, high-performance and high-density photonics integrated circuits (PICs) are in continuous demand for optical communications. Optical non-reciprocal devices, like optical isolators and optical circulators, are key components in PICs. Optical isolators allow the transmission of light in only one direction. They are needed to protect lasers from unwanted back-reflections, which could undermine their performance. Optical circulators are extensions of isolators, as they separate signals travelling in opposite directions, e.g., supporting bi-directional transmission. In theory, the key to achieve optical isolation is to break the Lorentz reciprocity. However, due to the reciprocal nature of most semiconductor and dielectric materials, the integration of optical isolators and circulators with other integrated optical components presents crucial design and fabrication challenges.

This thesis demonstrates integrated optical isolators and circulators on an InP membrane platform, on which integrated active and passive photonic components, including amplifiers and lasers, have already been demonstrated. The fabrication process of the integrated isolators and circulators is compatible with laser integration. It provides a step forward towards multi-functional and high-density PICs in telecommunication and sensing systems. A heterogeneous integration technique for the integrated optical isolators and circulators on the InP membrane platform is used. Epitaxially grown Cerium-doped Yttrium Iron Garnet (Ce:YIG) on a substituted Gadolinium Gallium Garnet (SGGG) substrate is chosen as a magneto-optic material to provide a non-reciprocal phase shift (NRPS). A Ce:YIG-die-to-InP-membrane adhesive bonding procedure is developed. An ultra-thin Benzocyclobutene (BCB) bonding layer is achieved to adhesively bond multiple Ce:YIG dies to the InP membrane. This heterogeneous integration technique also offers the potential of bonding other functional materials on the InP membrane platform.

In PICs, back reflections from optical components could contain signals with unknown polarization states. Hence, we propose two integrated nonreciprocal devices. First, an integrated optical isolator based on nonreciprocal polarization conversion (NRPC) is proposed. It contains two TE-pass polarizers and a non-reciprocal polarization converter. A nonreciprocal polarization converter is fabricated in the IMOS platform. A maximum nonreciprocal polarization conversion efficiency (PCE) of 9.8%

and 12.6 dB nonreciprocal transmission for the TE mode are measured. Second, an integrated polarization-independent optical isolator/circulator based on nonreciprocal phase shift (NRPS) is demonstrated, a first to the best of our knowledge, by connecting PCs with a MZI structure and adhesive bonding of a Ce:YIG layer on the InP platform. Simulations in a 3D finite-difference time domain solver are carried out for the proposed design. Over 40 dB optical isolation for both transverse electric (TE) mode input and transverse magnetic (TM) mode input is obtained. In experiment, the device shows maximum optical isolations of 27.0 dB TE mode input and 34.0 dB for TM mode input. The device could also work as a 4-port optical circulator. Optical isolations of at least 18.6 dB and 16.4 dB are measured between each circulator port pair for TE and TM mode input, respectively.

To achieve integrated optical isolators and circulators with high performance, several new building blocks are developed. Firstly, polarization-independent 2×2 multimode interferometers (MMIs) are proposed to evenly split TE/TM mode light into two branches. Secondly, integrated polarization converters (PCs) are implemented as key components in the device. Thirdly, optical delay lines are implemented in order to improve the optical bandwidth. Fourthly, deep etched waveguides are partly replaced with shallow etched ones, by including shallow-to-deep etch transitions. This not only reduces the propagation loss, but also increases the interaction between the waveguides and the Ce:YIG layer. Fifthly, thermo-optic phase shifters are implemented to tune the reciprocal phase shift. Finally, electromagnets are made directly onto the devices to integrate the source of magnetic fields. The implement of the electromagnets not only shrinks the footprint of the devices, but also makes the NRPS controllable.

The developments and results presented in this thesis open up new opportunities in PICs such as optical transmitters, wavelength division multiplexing networks, optical coherence tomography systems, and optical sensor interrogators. They are also promising for larger scale integration in PICs.

Contents

Acronyms

ALD Atomic layer deposition

BB building block

BCB benzo-cyclo-butene

Bi:YIG Bismuth substituted Yttrium Iron Garnet

CCW counter clockwise

Ce:YIG Cerium substituted Yttrium Iron Garnet

CMOS complementary metal-oxide-semiconductor

CW clockwise

DFB distributed feedback

EBL electron beam lithography

EME eigenmode expansion

EOF external optical feedback

FDE finite difference eigenmode

FDTD finite-difference time-domain

FGC focusing grating coupler

FOM figure of merit

FSR free spectral range

HPWG hybrid plasmonic waveguide

HWP half-wave plate

IMOS indium-phosphide-membrane-on-silicon

InGaAsP indium gallium arsenide phosphide

InP indium phosphide

IPA Isopropylalchohol

LHP left hand polarized

MMI multi mode interference

MO magneto-optic

MOKE Magneto-optic Kerr effect

MZI Mach-Zehnder interferometer

NLE nonlinear effect

NRL nonreciprocal loss

NRPC nonreciprocal polarization conversion

NRPS nonreciprocal phase shift

PBS polarization beam splitter

PC polarization converter

PCE polarization conversion efficiency

PD photodiode

PECVD plasma-enhanced chemical vapor deposition

PER polarization extinction ratio

PI polyimide

PIC photonic integrated circuit

PLD pulsed laser deposition

QPM quasi-phase matching

QW quantum well

RHP right hand polarized

RIE reactive-ion etching

RIG rare-earth-doped iron garnet

RPS reciprocal phase shift

SEM scanning electron microscope

SGGG (Ca, Mg, Zr) substituted gadolinium gallium garnet

SMSR side-mode suppression ratio

SOA semiconductor optical amplifier

SOI silicon-on-insulator

STM spatiotemporal modulation

TE transverse electric

TM transverse magnetic

UPW ultra pure water

YIG Yttrium Iron Garnet

Chapter 1

Introduction

1.1 Optical isolation

In photonic integrated circuits (PICs), semiconductor lasers are one of the most important building blocks (BBs), as they generate light with high spectral purity. The most common type of semiconductor lasers is a Fabry Perot (FP) laser. As shown in Fig. 1.1, a FP laser consists of three main elements: the gain medium, the pump and the resonator [1]. The resonator is composed of a cavity with two fully or partially reflecting mirrors so that photons can pass through the gain medium multiple times. This provides positive feedback for the creation of photons through stimulated emission which generates coherent radiation and increases the output power.

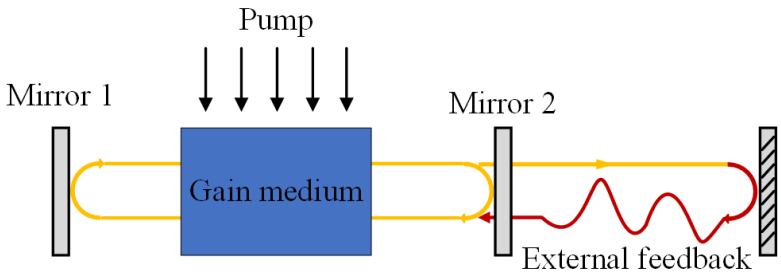

Figure 1.1: The basic schematic of a FP laser with external optical feedback (EOF).

External optical feedback (EOF) is defined as any kind of light returned into the laser cavity after leaving the laser cavity originally [2]. The behavior of lasers, especially on-chip semiconductor lasers, can be significantly affected by EOF due to the same positive feedback mechanism [3]. In PICs, abrupt interfaces, like active to passive transitions, waveguide crossings, and regrowth interfaces, may provide EOF to on-chip lasers [4]. This unwanted feedback causes severe problems, such as increasing intensity noise of the laser [5], narrowing or broadening of the spectrum [6] and degrading of the modulation response characteristics [7].

Optical isolators are devices that block light in one direction but allow light to pass in the opposite direction [8]. Conventionally, bulk optical isolators are placed between laser modules and other devices to avoid EOF. However, such bulk isolators are equipped in module level, which results in a significant proportion of volume and package cost. In the meanwhile, reflection-insensitive on-chip lasers have been investigated to bypass the requirement for optical isolation in PICs [9]. A reflection insensitive quantum dot laser on Si operating up to -7.4 dB optical feedback has been demonstrated [10]. However, as the integration density and complexity of PICs are increasing rapidly, this method becomes more and more challenging. So, it is crucial to develop integrated optical isolators in order to prevent unintended feedback from reaching the on-chip lasers, thus maintaining their stability.

Optical circulators are extensions of isolators, as they separate signals travelling in opposite directions, e.g., supporting bi-directional transmission. Thus, beyond protecting lasers from EOF, optical circulators are widely used in numerous applications, such as add-drop multiplexers, wavelength division multiplexer, optical frequency domain reflectometers, and fiber optic sensors. For the next-generation optical networks, integrated optical isolators and circulators become important in achieving multi-function, high-performance, large-scale, and low-cost PICs [11].

1.2 Optical nonreciprocal devices

Nonreciprocal optical devices, like optical isolators and circulators, are indispensable in optical systems. As extensions of optical isolators, optical circulators can not only protect lasers from EOF, but also separate signals traveling in opposite directions, e.g., supporting bi-directional transmission. Integrated optical circulators are promising for the next level up with single chip implementations for fiber sensor interrogators, optical imaging systems and transceivers.

In this section, the Faraday effect is explained, which is the basis of the conventional bulk optical isolators and circulators. Then, introductions for optical isolators and circulators are given.

1.2.1 Faraday effect

The key component in conventional optical isolators and circulators is a magneto-optic (MO) medium, in which the Faraday effect presents under the influence of a magnetic field in the z direction, as shown in Fig. 1.2.

In 1845, Michael Faraday first observed the rotation of the polarization of light as it propagated through a MO medium in the same direction as an external magnetic field. The Faraday rotation angle θ_F can be expressed as:

$$\theta_F = VBd \tag{1.1}$$

where V is the Verdet constant [12], which depends on the wavelength. B is the magnetic flux density in the propagation direction, and d is the length of the MO medium. Ferrimagnetic garnets such as single crystalline rare-earth-doped iron garnet

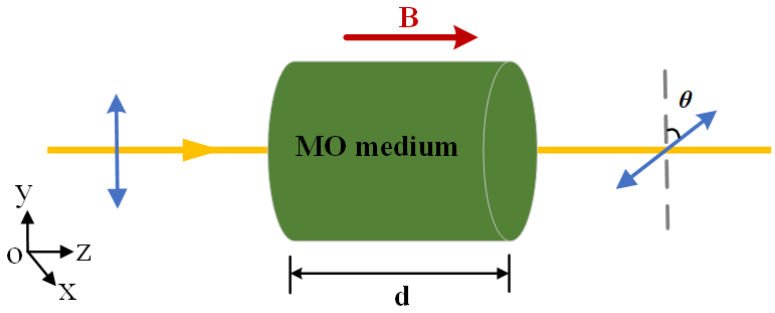

Figure 1.2: Principle of a Faraday rotator.

(RIG) films are widely used in commercial optical isolators and circulators because of their large Verdet constant. When the magnetic field is in the z direction, the permittivity tensor of these kinds of garnets can be written as:

$$\hat{\varepsilon} = \begin{bmatrix} \varepsilon_0 & \varepsilon_{xy} & 0 \\ -\varepsilon_{xy} & \varepsilon_0 & 0 \\ 0 & 0 & \varepsilon_0 \end{bmatrix} \tag{1.2}$$

where $\varepsilon_{xy} = ig_z$, g_z is the gyration vector of the garnet medium in the z direction. $\varepsilon_0 = n_0^2$, n_0 is the refractive index of the RIG film.

When the incident light is linearly polarized, its electric field and magnetic field can be expressed as:

$$E = E_0 e^{i(\vec{k}\cdot\vec{r}-\omega t)} \tag{1.3}$$

$$H = H_0 e^{i(\vec{k}\cdot\vec{r}-\omega t)} \tag{1.4}$$

By solving Maxwell's equation, the linearly polarized light can be decomposed as a superposition of the right hand polarized (RHP) and left hand polarized (LHP) states of light [13]:

$$E_{\mathrm{RHP}} = \frac{1}{\sqrt{2}} \begin{bmatrix} 1 \\ -i \end{bmatrix} e^{-i\omega(\frac{n_+}{c} z - t)} \tag{1.5}$$

$$E_{\mathrm{LHP}} = \frac{1}{\sqrt{2}} \begin{bmatrix} 1 \\ i \end{bmatrix} e^{-i\omega(\frac{n_-}{c} z - t)} \tag{1.6}$$

where $n_\pm^2 = \varepsilon \pm g_z$. From a quantum mechanical point of view, the difference in refractive index for RHP and LHP light derives from the splitting of energy levels in

the MO medium. This splitting depends on the spin of the particle, which is related to the handedness of the polarization [14].

According to equations 1.4 and 1.5, a phase difference presents between RHP and LHP light after propagating over an interaction length d. This phase difference shows as the polarization plane of the light rotates with an angle θ_F , which can be expressed as:

$$\theta_F = \frac{\pi d}{\lambda}(n_+ - n_-) \tag{1.7}$$

1.2.2 Bulk optical isolators and circulators

Conventional bulk optical isolators are widely used in optical networks for packaged lasers. They can achieve over 30 dB optical isolation with less than 1 dB optical loss in the near infrared wavelength region.

The principle of a bulk isolator is illustrated in Fig. 1.3. The isolator is composed of a polarizer oriented at 0°, a Faraday rotator and a polarizer oriented at 45°. In the forward direction, light excited from the laser becomes polarized 0° after travelling through the 0° polarizer. Then, the polarization plane of the light is rotated by 45° in the Faraday rotator in the presence of an external magnetic field. The light can then pass through the 45° polarizer since its polarization plane is parallel to the axis of the analyzer. In the backward direction, after travelling through the 45° polarizer and Faraday rotator, the reflected light is rotated by 90° again but in opposite direction, and thus, it is perpendicular to the axis of the 0° polarizer. Therefore, the light will be blocked.

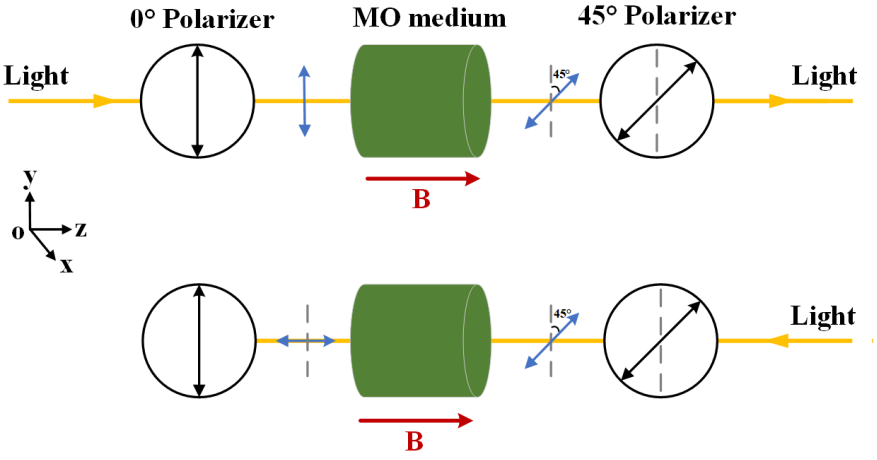

Figure 1.3: Principle of a bulk isolator.

Bulk optical circulators are not only used in telecommunication systems for increasing transmission capacity of existing networks, but also are widely used in optical set-ups and sensing systems. The working principle of a bulk circulator is shown

in Fig 1.4. For light input from port 1, only vertically polarized light can enter the Faraday rotator after passing through the first polarization beam splitter (PBS). The vertically polarized light will be rotated by 45° in the Faraday rotator and be rotated by -45° in the half-wave plate (HWP). It will be excited from port 2 after passing through the second PBS. For light injected into port 2, it will be excited from port 3 because of the nonreciprocal polarization rotation in the Faraday rotator.

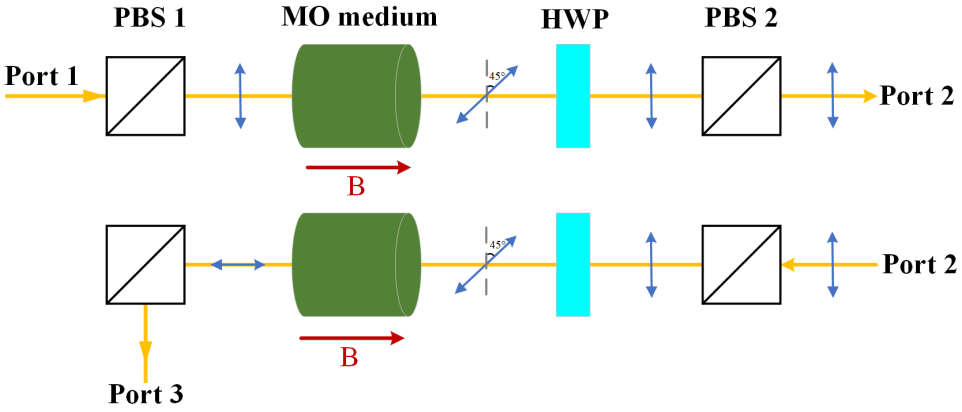

Figure 1.4: Principle of a bulk circulator.

The optical isolators and circulators shown in Fig 1.3 and Fig 1.4 are polarization dependent because the input light should be aligned with the polarizer. As the density and complexity of optical systems increases, optical signals with unknown polarization states may exist and disturb the performance of the system. Hence, polarization independent optical isolators and circulators are needed at multiple locations in the system, not only in front of the lasers.

Polarization independent optical isolators and circulators can be achieved by replacing the polarizers with wedge-shaped birefringent crystals. Commercial polarization independent optical isolators and circulators have shown over 40 nm wavelength range, over 30 dB isolation and less than 1 dB insertion loss [15, 16].

1.2.3 Integrated optical isolators and circulators

Integrated optical isolators and circulators in PICs are highly desired for the next-generation optical networks. However, the integration of optical isolators and circulators on semiconductor platforms still presents crucial design and fabrication challenges [17].

In general, integrated optical isolators and circulators are mainly based on three different principles [18]: i) applying nonlinear effect (NLE), ii) by spatiotemporal modulation (STM), and iii) using MO materials.

Various NLEs, like stimulated Raman amplification [19], stimulated Brillouin scattering [20] and parametric amplification [21] are used. Optical nonreciprocity can be achieved by interacting propagating light with travelling wave excitations. For

devices based on nonlinear effects, no additional materials are needed besides from what is already offered in the semiconductor platforms. However, the optical isolation of this kind of devices depends on the optical power of the incident light. This is not practical because the EOF to the lasers should be eliminated for any input power [22].

For devices based on STM, the optical nonreciprocity is achieved by modulating the refractive index of the waveguide. The modulation can act differently for light propagating in forward and backward directions. This can be achieved by implementing a microwave [23] or acoustic signal [24]. Like the devices based on nonlinear effects, no modifications to the semiconductor platforms are needed for this kind of devices. Integrated optical isolators, based on radio frequency-modulated electro-refractive modulators, have been demonstrated [25] in 2011. However, these devices have high power consumption because of the high-speed drive circuits. They also suffers from small optical bandwidth and low optical isolation.

For devices using MO materials, they are based on the interaction between light and the MO materials. Lorentz reciprocity can be broken because of the inherent asymmetric dielectric tensor of MO materials when an external magnetic field is applied. As discussed in the previous section, bulk optical isolators and circulators using MO materials are widely used in optical systems. Integrated optical isolators and circulators using MO materials have made great progress in the past few decades. Optical isolators on Si with over 30 dB optical isolation and less than 2 dB insertion loss have been demonstrated [26].

Compared with devices based on NLE and STM, MO devices show performances comparable with conventional bulk isolators, and they do not have the drawbacks mentioned above. There are several challenges for integrated MO devices:

- MO materials are incompatible with the semiconductors because of lattice mismatch. Different techniques for heterogeneous integration of high-quality MO films and semiconductors have been developed [26].

- Bulk isolators and circulators exhibit excellent performance (over 30 dB isolation and less than 1 dB insertion loss and 40 nm operating wavelength range). To date, integrated isolators and circulators with comparable performance have not been demonstrated.

- To increase the integration density in PICs, integrated isolators and circulators at multiple locations in a circuit are needed. It is more practical to use polarization independent isolators and circulators because of the potential unknown polarization states in the circuit. However, to date, MO devices can only operate for either TE or TM mode light. Integrated polarization-independent optical isolators and circulators have not been experimentally developed yet.

- An external magnetic field is required to operate MO devices. In a conventional isolator, a permanent magnet is packaged with other components. This is not practical for PICs due to its large footprint. Methods for applying a magnetic field need to be developed.

1.3 The InP membrane platform

In this thesis, the integrated optical isolators and circulators are based on the InP membrane platform. This section gives an overview of the platform and a summary of the developed building blocks, which will be implemented for the demonstration of the integrated optical isolators and circulators.

1.3.1 The IMOS concept

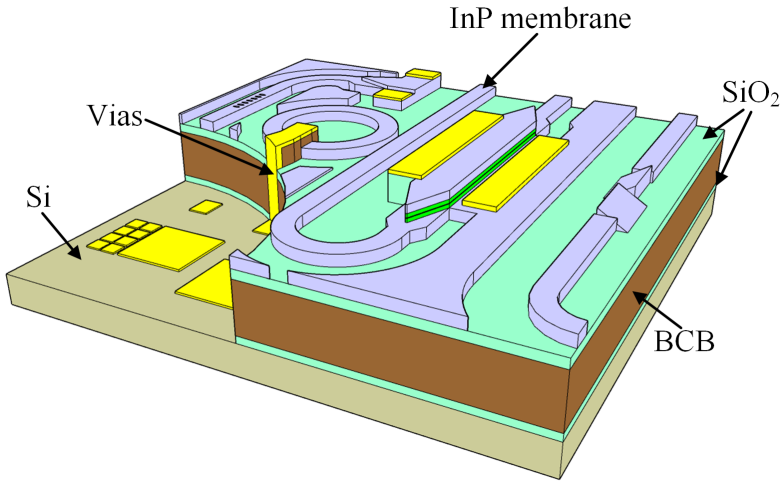

Figure 1.5: Schematic of the IMOS platform [27].

The indium-phosphide-membrane-on-silicon (IMOS) platform is regarded as the next generation generic InP photonic integration platform [28]. As shown in Fig 1.5, the indium phosphide (InP) membrane is adhesively bonded onto a Si wafer. Benzocyclo-butene (BCB) is used as an adhesive. Two SiO_2 layers are used on both the Si and the InP membrane to improve the adhesion of BCB. Compared with the generic InP platform, the IMOS platform has the following advantages: i) The refractive indexes of InP and BCB are 3.17 and 1.54, respectively. The high refractive index contrast between InP and BCB creates a high confinement of the modes. Optical components with compact dimensions can therefore be achieved in the IMOS platform. It provides a step forward towards a high-density PIC. ii) The BCB bonding process allows the IMOS membrane to be processed from both sides, which brings high flexibility to device design [29]. iii) Electrical connections between InP membrane and Si can be created through metal vias. This makes the IMOS platform promising for co-integration with complementary metal-oxide-semiconductor (CMOS) electronics [30].

1.3.2 The IMOS building blocks

Designs and performance of several key components in the IMOS platform are presented in this section.

- Waveguide

  The IMOS waveguide is 400 nm in width and 300 nm in height. The high refractive index contrast between InP and BCB creates a high confinement of the modes. Only fundamental transverse electric (TE) and transverse magnetic (TM) modes can exist. The optical mode intensity profiles of the fundamental TE and TM modes are shown in Fig 1.6. The typical waveguide loss for TE mode light is around 15 dB/cm using electron beam lithography (EBL). The lowest propagation loss for TE mode light obtained so far is 1.8 dB/cm [31] using 193 nm deep UV lithography in combination of an optimized reactive-ion etching (RIE) process [32].

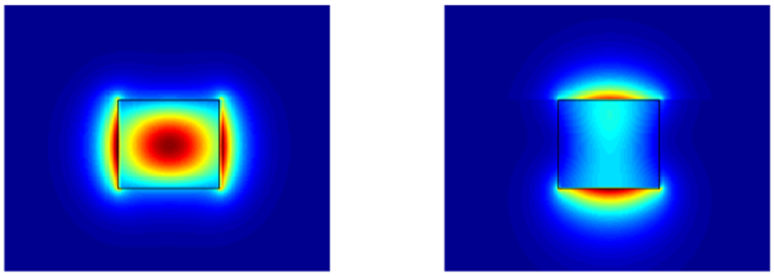

(a) TE mode (b) TM mode

Figure 1.6: Optical mode intensity profiles of the fundamental TE and TM modes.

- Focusing grating coupler

  Focusing grating couplers (FGCs) are used to couple light between the InP membrane and an optical fiber [33]. As shown in Fig 1.7. FGCs are realized with shallow etch into the membrane, with a depth of 120 nm. FGCs for both TE and TM polarizations can be realized by varying the period width. The typical insertion losses of FGCs are between 5 and 8 dB for both TE and TM input light, at a wavelength of 1550 nm [27].

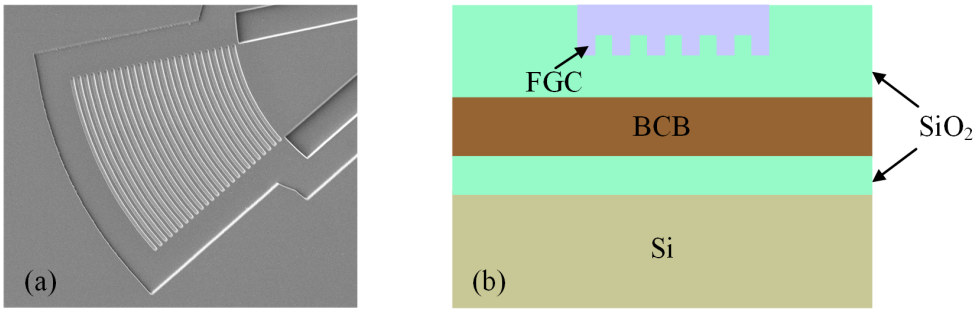

Figure 1.7: (a) Top view of the FGC before bonding. (b) Cross section of the FGC after bonding.

- Multi mode interference coupler

  MMI couplers are used to split and combine optical power into different ports. In the IMOS platform, both 1×2 MMI and 2×2 MMI are designed and fabricated, as is shown in Fig. 1.8. For the 1×2 MMI, the insertion loss for TE and TM modes is around 0.5 dB at 1550 nm [27]. For the 2×2 MMI, an imbalance of less than 1 dB for the TE and TM modes is achieved [27].

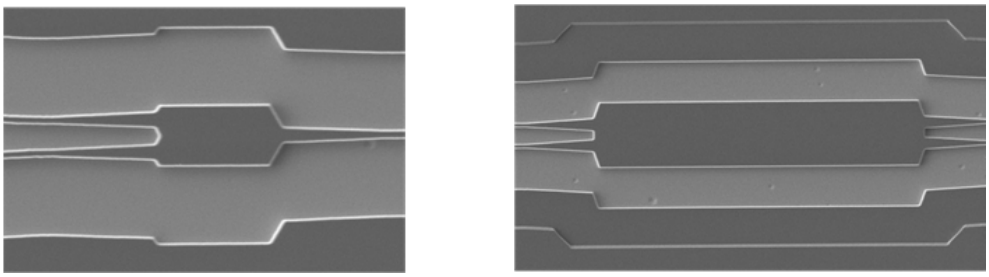

Figure 1.8: (a) Top view of the 1×2 MMI. (b) Top view of the 2×2 MMI.

- Polarization converter

  As shown in Fig. 1.9, the polarization converter (PC) contains two triangular waveguides with one small rectangular waveguide section in-between. Measurements show a polarization conversion efficiency of over 99% with insertion losses of less than 1.2 dB at a wavelength of 1.53 μm [34].

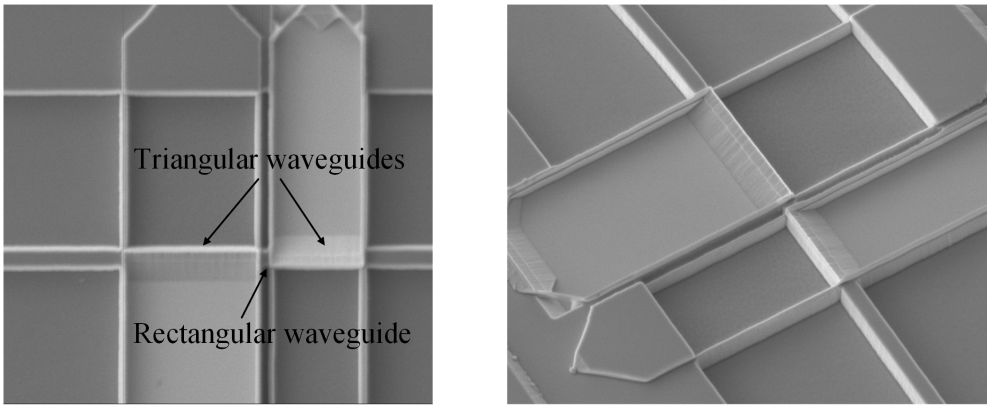

Figure 1.9: (a) Top view of the PC. (b) Side view of the PC.

- Distributed feedback laser

  Distributed feedback (DFB) lasers have been demonstrated on the IMOS platform [35]. Fig. 1.10 shows a schematic of the DFB laser. The gratings are shallow etched (120 nm in depth) in the InP waveguide layer. The laser operates in single mode with over 60 dB side-mode suppression ratio (SMSR). The output power is approximately 1 mW at 10°C [35].

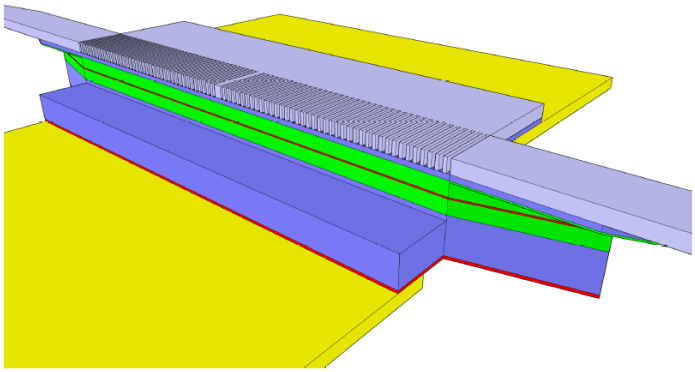

Figure 1.10: Schematic of the DFB laser [27].

This thesis will focus on the development of integrated optical isolators and circulators, which aim to integrate the aforementioned component in a circuit level. It is also worth to mention that other passive and active devices, like arrayed waveguide gratings [36], photodetectors [37], electro-optical modulators [38], are also demonstrated in the IMOS platform.

1.4 Outline of this thesis

The IMOS platform is promising for the next-generation PIC with compact footprint and low power consumption. Multiple functionalities, like light generation, amplification, modulation and detection, have been developed on this platform [39]. However, optical isolation and circulation are still absent. This absence becomes a bottleneck in achieving a high-density functional PIC.

This thesis is aiming at the demonstration of integrated optical isolators and circulators with important functions, including the ability for co-integration with passive and active photonic components, high optical isolation ratio, low insertion loss, and broadband operation. In the meanwhile, polarization independence is also a crucial feature, as back reflections in a PIC could contain signals with unknown polarization states. To the best of the author's knowledge, integrated polarization-independent optical isolators and circulators have not been experimentally developed yet.

To achieve all these functions, the following research questions in terms of device design combined with materials development and integration need to be answered:

- What are the approaches used to achieve integrated optical isolators and circulators? Which approach is the most suitable one for the IMOS platform? (Chapter 2)
- How to solve the incompatibility between the MO material and the IMOS platform? (Chapter 3)
- What circuit architecture is needed to achieve an integrated optical isolator in the IMOS platform? (Chapter 4)
- How to achieve polarization independence in isolators and circulators for the first time? (Chapter 5)
- How to get rid of the bulk permanent magnet, which is used to provide a static magnetic field to magnetize the MO material? (Chapter 6)
- How to increase the optical isolation bandwidth and tune the operation wavelength? (Chapter 6)
- How to integrate isolators and circulators with active BBs, especially lasers, in the IMOS platform? (Chapter 6)

The structure of the thesis is as follows:

Chapter 2 covers the background behind using magneto-optic materials to achieve optical isolation. An overview of commonly used MO materials in integrated photonics is given. The origin of magnetism and the theory behind the MO effect in integrated photonics are explained. Integrated optical isolators based on Faraday rotation, nonreciprocal loss, and nonreciprocal phase shift (NRPS) are studied. The state of the art of integrated optical isolators and circulators using NRPS is evaluated.

Chapter 3 covers the heterogeneous integration technology of Ce:YIG in the IMOS platform. A Ce:YIG-die-to-InP-membrane adhesive bonding procedure is developed.

An ultra-thin BCB bonding layer is achieved to adhesively bond multiple Ce:YIG dies to the InP membrane. This heterogeneous integration technique also offers the potential of bonding other functional materials on the InP membrane platform.

Chapter 4 covers the design, simulation, fabrication methodology, and characterization of an integrated optical isolator based on nonreciprocal polarization conversion (NRPC). It contains two TE-pass polarizers and a non-reciprocal polarization converter. The non-reciprocal polarization converter makes use of the NRPS effect and contains two asymmetric waveguide sections (triangular waveguides) as partial polarization converter and a rectangular waveguide section, on which a Ce:YIG layer is adhesively bonded.

Chapter 5 covers the design, simulation, fabrication methodology, and characterization of the integrated polarization-independent isolators and circulators. A polarization-independent isolator/circulator, by connecting PCs with a Mach-Zehnder interferometer (MZI) structure and adhesive bonding of a Ce:YIG layer, is demonstrated in the IMOS platform.

Chapter 6 proposes several BBs to further improve the performance and to reduce the footprint of the nonreciprocal devices. An integrated electromagnet is designed and fabricated in the IMOS platform. The electromagnet can replace the bulk permanent magnet to provide a sufficient magnetic field. A thermal phase shifter is implemented in the device to tune the operation wavelength. Two shallow-to-deep transition tapers are designed. The transition tapers are compatible with the IMOS process flow. The optical isolation bandwidth of the device can be improved by reducing the unbalance of the MZI structure. A method to integrate the optical nonreciprocal devices with active devices in the IMOS platform is proposed.

Chapter 7 concludes the work presented in this thesis. An outlook for improvements of integrated optical isolators and circulators is given, as well as proposals for future research.

Chapter 2

Magneto-optic effects in integrated photonics

2.1 Magneto-optic materials for integrated photonics

A material is classified as MO when it affects the propagation characteristics of light in the presence of an external magnetic field. In general, MO materials can be divided into four different types: diamagnetic, paramagnetic, ferromagnetic and ferrimagnetic [40], depending on the orientation of magnetic moments of the atoms. A detailed overview of the MO materials can be found in [41].

For the applications of integrated optical isolators and circulators, three aspects should be considered when using MO materials:

- Faraday rotation coefficient. This refers to the rotation angle of the polarization in units of degrees per centimeter. A material with a larger Faraday rotation coefficient can be used to achieve optical isolators with a more compact size.
- Optical loss. This mainly refers to the absorption loss of the material. For optical isolators working in the near infrared wavelength in that wavelength region, a material with low optical loss is required.
- The integration ability with semiconductors. Most of the MO materials are incompatible with semiconductors. Different techniques, such as deposition techniques and bonding techniques, have been discovered for heterogeneous integration [26]. More details about the bonding technique are described in Chapter 3.

The quality of the MO materials can be evaluated by the MO figure of merit (FOM), which is defined as [42]:

$$\mathrm{FOM} = \frac{\Theta}{\alpha}\ (\mathrm{deg/dB}) \tag{2.1}$$

where Θ and α are the Faraday rotation coefficient and the optical absorption of the material. For an optical isolator, a larger FOM indicates that the propagation loss is lower to achieve 45° Faraday rotation. A list of the MO materials used for integrated optical isolators at 1550 nm is shown in Table 2.1.

Ce:YIG film on Si/Silica has been developed by using pulsed laser deposition (PLD) [43] or sputtering [44], as listed in Table 2.1. However, the performance of the Yttrium Iron Garnet (YIG) film is limited due to lattice mismatch and thermal mismatch between the YIG film and Si/Silica. A high FOM of 769 deg/dB has been demonstrated in Bismuth substituted Yttrium Iron Garnet (Bi:YIG) deposited on Si [45]. This technique is promising for monolithic integration of optical isolators on Si. However, it is still in doubt whether this technique is suitable for a large-scale production because several issues, like cracks, secondary phases, grain boundaries, all of which may appear during the deposition process [42]. These issues degrade the performance of the Ce:YIG/Bi:YIG film. Furthermore, this technique cannot be applied in the InP platform because the annealing temperature for YIG crystallization is over 800°C, which is beyond the epitaxial growth temperature of III/V semiconductor.

Cobalt ferrite ($CoFe_2O_4$) is also used in the demonstration integrated optical isolators [46]. Because it shows much larger Faraday rotation coefficients as compared to magnetic garnets in the near infrared wavelength region. However, the optical loss of the $CoFe_2O_4$ film is over 1000 dB/cm, due to optical scattering and absorption [47].

Faraday rotation has been demonstrated in an InP waveguide with magnetic dopants [48]. The measured Faraday rotation coefficient is 125 deg/cm at 1 Tesla magnetic field when the iron doping concentration is up to 10^{17} cm^{-3}.

MO material	Figure of merit (deg/dB)	Optical loss (dB/cm)	Deposition method
Ce:YIG on SGGG [49]	943	6	PLD
Ce:YIG on SGGG [50]	321	14	Sputtering
Ce:YIG on Si [43]	22	58	PLD
Ce:YIG on Silica [44]	56	48	Sputtering
Bi:YIG on Si [45]	769	2.6	PLD
$CoFe_2O_4$ [47]	<24	>1000	Sputtering
Fe:InP [48]	26	1	Doping
Fe:InGaAsP [51]	75	1.66	Doping

Table 2.1: Comparison of different MO materials.

Among the MO materials listed above, Ce:YIG on (Ca, Mg, Zr) substituted gadolinium gallium garnet (SGGG) shows the highest FOM. This material is widely used in conventional bulk isolators and circulators. Its excellent MO performance was first found in the 1980s [52, 53] by sputtering a layer of Ce:YIG film on the SGGG substrate. A PLD growth method is discovered later to further improve the performance [49, 54]. Because the high-quality Ce:YIG film is sputtered on a lattice matched SGGG substrate, it is difficult to integrate it with semiconductors due to lattice and thermal mismatch. Bonding techniques, such as surface-activated direct bonding [55] and adhesive bonding [56] have been developed to overcome this ma-

terial incompatibility. These techniques are compatible with the existing multi-die-to-wafer bonding technique, which are developed for heterogeneously integrated photonic devices [57,58]. More details of the bonding techniques will be given Chapter 3.

Property	Value
Lattice constant	12.57 Å
Annealing temperature	800°C
Refractive index	2.2
Saturation magnetization (in plane)	50 Oe
Saturation magnetization (out of plane)	2000 Oe
Thermal conductivity	7.2 W/m·K

Table 2.2: Properties of Ce:YIG.

In this thesis, Ce:YIG on SGGG[1] is used for the development of integrated optical isolators and circulators. The Ce:YIG film is sputtered on a 3-inch SGGG substrate. The material properties of Ce:YIG on SGGG at 1550 nm are shown in Table 2.2.

2.2 Magneto-optic effects in integrated photonics

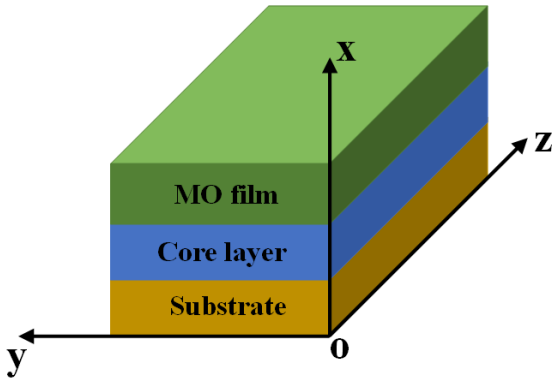

Figure 2.1: Schematic of a slab waveguide with a MO cladding.

In free space, the optical isolators and circulators are based on the Faraday effect, which is applied in a bulk MO medium when light propagation is parallel to the magnetic field direction. In integrated photonics, we consider a slab waveguide with a semiconductor layer as the core layer and a MO film as the top cladding, as shown in Fig 2.1.

[1] provided by Professor Yuya Shoji and Professor Tetsuya Mizumoto from the Tokyo Institute of Technology.

From a geometric optics point of view, the light follows a zigzag route because of total internal reflection at the core-cladding interface. Three different types of Magneto-optic Kerr effects (MOKEs) arise depending on the direction of the magnetic field, as shown in Fig 2.2.

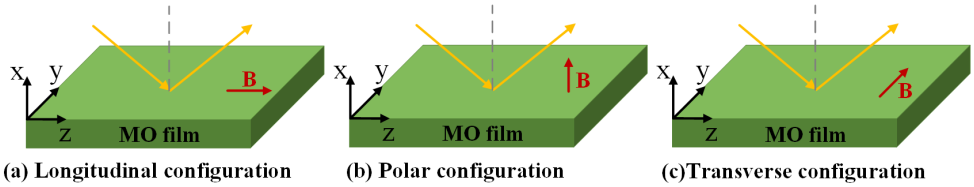

Figure 2.2: Three different types of MOKEs. (a) Longitudinal configuration. (b) Polar configuration. (c) Transverse configuration.

In the longitudinal and polar configurations, the reflected light rotates its polarization axis and gains a certain ellipticity [59]. This arises from the difference of the refractive index of RHP and LHP, as explained in section 1.2. An integrated photonic device for on-chip magneto-optical memory reading has been demonstrated exploiting the polar MOKE effect [60]. The device combines InP waveguides with ferromagnetic thin-film multilayers as top-claddings. An integrated optical isolator based on NRPC has been demonstrated exploiting the longitudinal MOKE effect [61]. More details are given in the next subsection.

In the Transverse configuration, the magnetic field is parallel to the surface of the MO film and perpendicular to the incidence plane of the light. A change in the effective refractive index is induced and results in either nonreciprocal loss (NRL) or NRPS depending on the properties of the MO material.

In integrated photonics, the change of the effective refractive index is treated as a perturbation. The NRL or NRPS can be determined quantitatively using perturbation theory [62].

2.2.1 Nonreciprocal polarization conversion

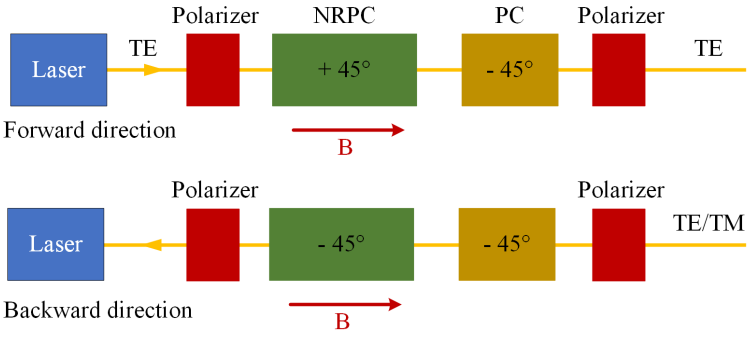

Figure 2.3: An integrated optical isolator based on NRPC.

An integrated optical isolator can be achieved by importing the Faraday rotation scheme in bulk isolators. The key component in that scheme is a nonreciprocal polarization converter, which can be achieved by applying the longitudinal MOKE. For a MO film like RIG, the ellipticity can be ignored. So, the polarization plane is rotated in the presence of a magnetic field in the z direction in Fig 2.2 (a).

The principle of an integrated optical isolator based on NRPC is illustrated in Fig 2.3. In the forward direction, the TE light emitted from the laser passes the first polarizer. Then, it is rotated by 45°after NRPC. After the reciprocal PC, the light is rotated by -45°. So, the output light is still in the TE polarization. In the backward direction, the TE mode is converted to the TM mode, and be filtered by the polarizer before reaching the laser module.

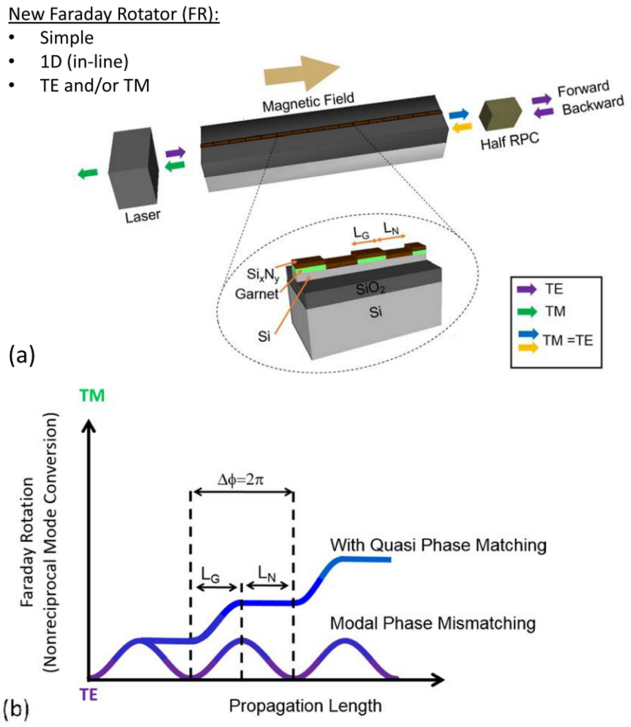

Figure 2.4: (a) Schematic of the NRPC based isolator using quasi-phase matching (QPM). (b) Faraday rotation with and without QPM. [63]

The main challenge of this design derives from the birefringence in the waveguide, which means that TE and TM modes have different propagation constants. As a result, a beating effect between the two polarizations [64] is induced. A QPM technique has been proposed to overcome the waveguide birefringence of the device [65]. QPM is achieved using alternating MO and non-MO segments with lengths that match the characteristic beat length of the polarized modes, as shown in Fig 2.4 (a). The top cladding of the waveguide is varied spatially, such that the period of the MO material and the non-MO material corresponds to a modal phase offset of $\Delta\phi = 2\pi$ [63], as

shown in Fig 2.4 (b). This device shows 11 dB optical isolation and 4 dB loss for TE mode light.

However, three challenges still remain in the NRPC based optical isolators. Firstly, the bandwidth is on the order of a nanometer because QPM is an inherently wavelength dependent process. Secondly, although QPM is used to reduce shape-induced birefringence in the waveguide, stress-induced, and growth-induced birefringence will also affect the performance of the device. Thirdly, in PICs, back reflections may contain signals with unknown polarization states. The TM part of the backward signal will be converted to TE, which will affect the laser operation. An integrated polarizer is still needed to filter any non-TE mode light in the backward direction.

2.2.2 Nonreciprocal loss

The concept of an integrated isolator based on NRL is firstly shown in 1999 [66]. A ferromagnetic film is patterned on a semiconductor optical amplifier (SOA), as shown in Fig 2.5. This metal layer is not only used as an electrical contact for current injection, but also as a source of NRL. The device shows nonreciprocal loss for the TM mode in the presence of a magnetic field in the transverse direction.

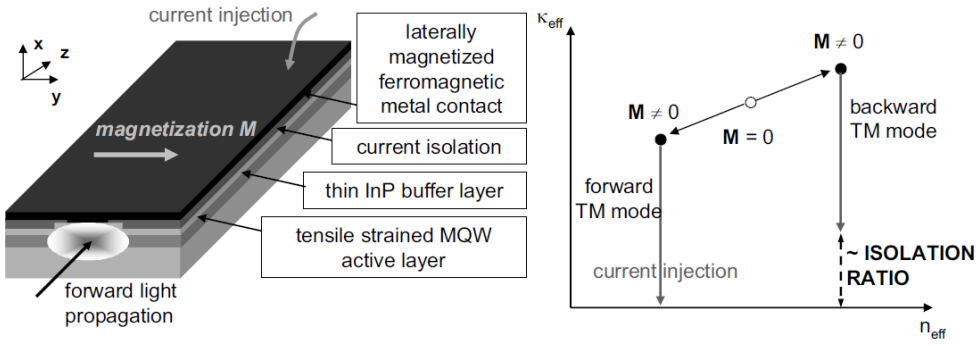

Figure 2.5: Principle of a NRL based optical isolator [66].

In the slab waveguide in Fig 2.1, the electric field and magnetic field of the TM mode can be expressed as:

$$E(x,z,t) = [E_x, 0, E_z]\exp(j\omega t - j\beta_{TM} z) \tag{2.2}$$

$$H(x,z,t) = [0, H_y, 0]\exp(j\omega t - j\beta_{TM} z) \tag{2.3}$$

The permittivity tensor of the MO film can be written as [67]:

$$\hat{\varepsilon} = \begin{bmatrix} \varepsilon_0 & 0 & \varepsilon_{xz} \\ 0 & \varepsilon_0 & 0 \\ \varepsilon_{xz} & 0 & \varepsilon_0 \end{bmatrix} \tag{2.4}$$

Where $\varepsilon_{xz} = ig_y$, g_y is the gyration vector of the garnet medium in the y direction. g_y is proportional to the Faraday rotation coefficient in the y direction and can be written as:

$$g_z = \frac{2\theta_F n_0}{k_0} \tag{2.5}$$

Where θ_F is the Faraday rotation coefficient of the MO material.

In this case, ε_{xz} can be treated as a perturbation since its much smaller than ϵ_0 [68]. According to the perturbation theory, the change of propagation constant of the TM mode for different propagation directions can be written as follow:

$$\Delta\beta_{TM} = -j\omega\epsilon_0 \frac{\iint g_y E_x E_z \mathrm{d}x\mathrm{d}y}{\iint (E_x H_y - E_y H_x)\mathrm{d}x\mathrm{d}y} \tag{2.6}$$

For the ferromagnetic film, the imaginary component of $\Delta\beta_{TM}$ dominates and leads to the nonreciprocal absorption for the TM mode [69]:

$$\Delta\alpha = 2\mathrm{Im}\left[\Delta\beta_{TM}\right] = -\frac{4\pi}{\sqrt{\mu_0/\epsilon_0}}\mathrm{Re}\left[\frac{\iint g_y E_x E_z \mathrm{d}x\mathrm{d}y}{\iint (E_x H_y - E_y H_x)\mathrm{d}x\mathrm{d}y}\right] \tag{2.7}$$

The biggest advantage of this device is that it is integrated with SOAs or lasers inherently. The first full integration of a DFB laser with a NRL based isolator is demonstrated in 2006 [70]. 4 dB optical isolation is achieved at a wavelength of 1543.8 nm. However, this device still suffers from the high optical absorption from the ferromagnetic metal layer. It is not practical for application purposes.

2.2.3 Nonreciprocal phase shift

For MO material such as Ce:YIG, the real component of $\Delta\beta_{TM}$ is more significant than the imaginary component. The NRPS for the TM mode can be rewritten as:

$$\Delta\beta_{TM} = 2\omega\epsilon_0 \frac{\iint g_y E_x \frac{\partial E_x}{\partial x} \mathrm{d}x\mathrm{d}y}{\iint (E_x H_y - E_y H_x)\mathrm{d}x\mathrm{d}y} \tag{2.8}$$

Similarly, the NRPS for the TE mode can be rewritten as:

$$\Delta\beta_{TE} = 2\omega\epsilon_0 \frac{\iint g_y E_y \frac{\partial E_y}{\partial y} \mathrm{d}x\mathrm{d}y}{\iint (E_x H_y - E_y H_x)\mathrm{d}x\mathrm{d}y} \tag{2.9}$$

For the slab waveguide as is shown in Fig 2.1, a Ce:YIG film is used as the top-cladding to provide a NRPS. Such a waveguide is symmetric in the y direction. The electrical field of the TE mode is even in the y direction, meaning $\partial E_y/\partial y = 0$. Hence,

there is no NRPS for the TE mode. On the contrary, the waveguide is asymmetric in the x direction, meaning the NRPS for the TM mode exists.

To exploit the NRPS also for the TE mode, an asymmetric waveguide structure in the y direction is need. This can be done by placing the MO film next to the core layer, as shown in Figure 2.6.

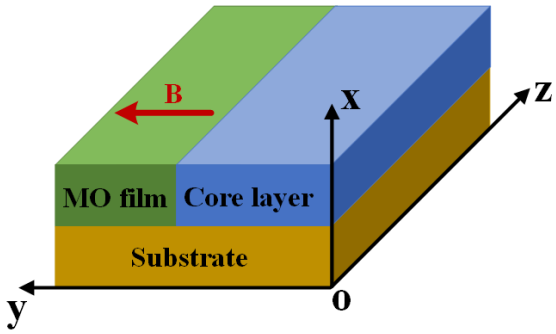

Figure 2.6: Schematic of a horizontally asymmetric waveguide.

In practice, Ce:YIG is usually chosen as the MO film to provide a NRPS because of its high Faraday rotation coefficient and low optical absorption in the near infrared wavelength region. Integrated optical nonreciprocal devices using Ce:YIG have been investigated for decades and an over 30 dB optical isolation has been obtained [71].

Compared with optical nonreciprocal devices based on NRPC and NRL, optical nonreciprocal devices based on NRPS do not need to meet the phase-matching condition between the TE and TM polarization or suffer from the high optical absorption loss. Optical nonreciprocal devices based on NRPS will be discussed and developed in this thesis.

2.3 Integrated optical isolators and circulators based on NRPS

As discussed in the previous section, NRPS can only happen for either TM or TE mode light in the MO waveguide, depending on the waveguide symmetry and the direction of the external magnetic field. Integrated optical nonreciprocal devices based on NRPS are extensively developed in interferometric structures [26], such as MZI and ring resonators. In this section, an overview of the integrated optical nonreciprocal devices, operating for TM mode, TE mode and both TE and TM modes, is given.

2.3.1 Integrated optical isolators and circulators for TM mode light

A typical MZI-based optical isolator for TM mode light is shown in Fig 5.3 [72]. The device is fabricated on the silicon-on-insulator (SOI) platform. A phase bias is

induced in one branch to provide a reciprocal phase shift (RPS) of $\pi/2+2m\pi$, where m is an integer. A Ce:YIG layer is directly bonded on the waveguides. Magnetic fields are applied perpendicular to the two branches with opposite directions. The nonreciprocal phase difference for the TM mode light is set to $\pi/2$ in one propagation direction and $-\pi/2$ in another propagation direction by changing the length of the waveguides covered with Ce:YIG.

In one direction, the input light will interfere constructively and output from the middle port of the 3×2 coupler. In another direction, the input light will interfere destructively and radiate from the side ports of the 3×2 coupler. An optical isolation of 30 dB at 1548 nm and a bandwidth of 1nm are achieved. By precisely controlling the length difference of the two branches, the phase bias is $\pi/2$ rather than $100\pi+\pi/2$ in [72]. Thus, the calculated bandwidth of this device can be increased to 39 nm using the same configuration [73].

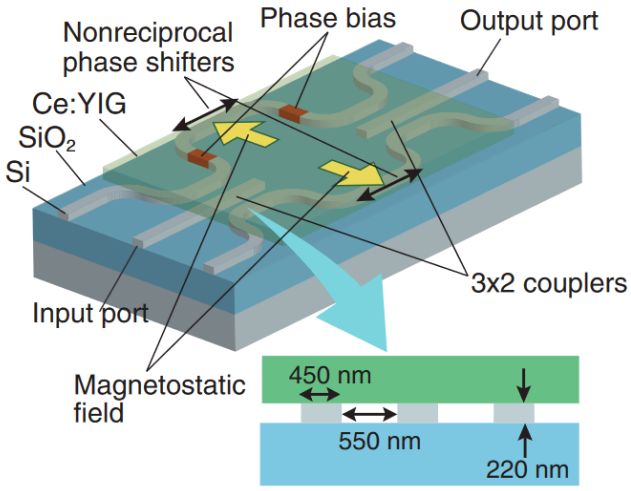

Figure 2.7: Schematic of a MZI-based optical isolator [72].

An optical circulator can be achieved by replacing the 3×2 couplers in Fig 2.8 with 3 dB directional couplers, as shown in Fig 2.8 [74]. For the TM mode light input from port 1, it will be divided into two branches after the 3 dB directional coupler. The RPS and NRPS in two arms will be canceled out so the light will output from port 2. For light input from port 2, it will experience a π phase difference in the two branches and output from port 3. Based on the same principle, a light input from port 3 will output from port 4, and the light input from port 4 will be directed to port 1. Hence, a four-port optical circulator is obtained.

An integrated optical isolator can also be achieved by introducing NRPS into a ring resonator, as shown in Fig 2.9 [75]. A ring resonator is fabricated on the SOI platform. a Ce:YIG die is directly bonded on the ring and the bus waveguide. An electromagnet is fabricated on the backside of the SGGG substrate, which is polished to 5 μm to reduce the distance between the electromagnet and the Ce:YIG layer. An NRPS for the TM mode light is introduced when the current is on. Thus, the

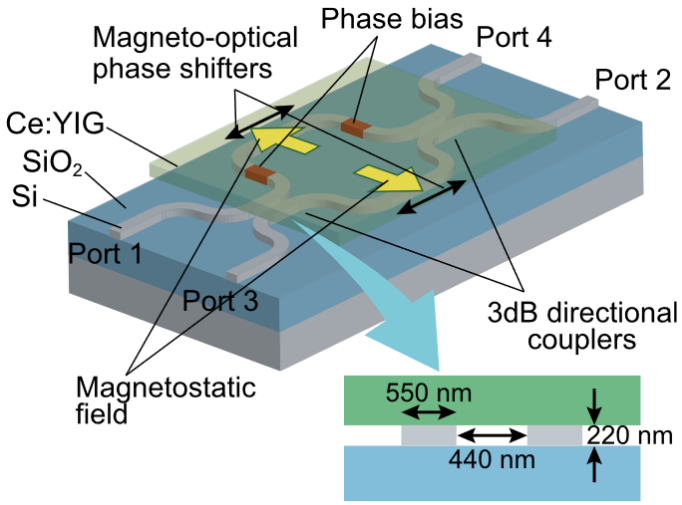

Figure 2.8: Schematic of a MZI-based optical circulator [74].

resonant wavelength of the ring resonator in clockwise (CW) and counter clockwise (CCW) directions is different. An optical isolation of 32 dB is achieved by keeping the forward propagating light on-resonance and the backward propagating light off-resonance. However, this device suffers from narrow operation bandwidth due to the resonant nature of the ring.

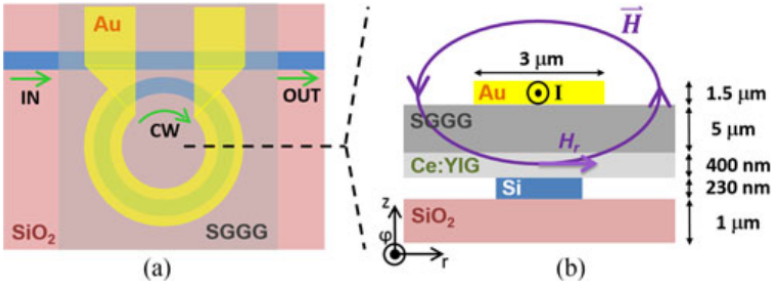

Figure 2.9: Schematic of a ring-based optical isolator [75].

Similarly, a four-port optical circulator can be achieved by adding a second bus waveguide to the ring-based isolator, as shown in Fig 2.10. The NRPS causes a split of resonance wavelength in CW and CCW directions. A maximum optical isolation of 14.4 dB and a 2.3 dB insertion loss have been achieved [76].

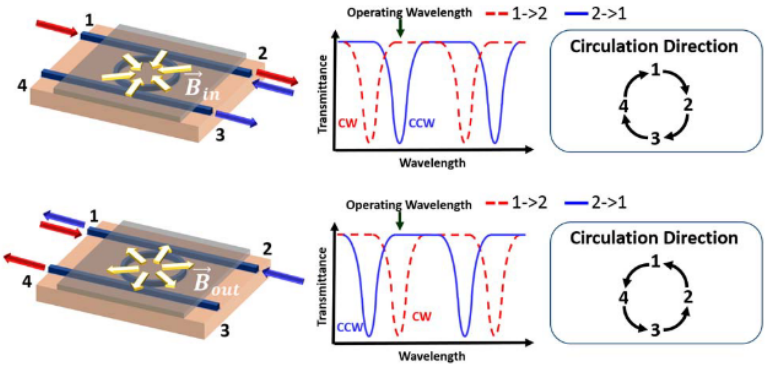

Figure 2.10: Schematic of a ring-based optical circulator [76].

2.3.2 Integrated optical isolators and circulators for TE mode light

The optical gain in typical semiconductor lasers or SOAs is polarization dependent. The output light from most lasers or SOAs are TE polarized because of the strain in indium gallium arsenide phosphide (InGaAsP) quantum wells (QWs) [77].

To achieve integrated optical isolators and circulators for TE mode light, mainly two solutions are developed:

1) A TE-TM mode converter is implemented with a TM-mode isolator, as shown in Fig 2.11 [78]. The TE light emitted from the laser will be rotated to the TM mode. Then, the TM mode light will experience a NRPS, and optical isolation is achieved as discussed in the last subsection. A maximum optical isolation of 26.7 dB is demonstrated.

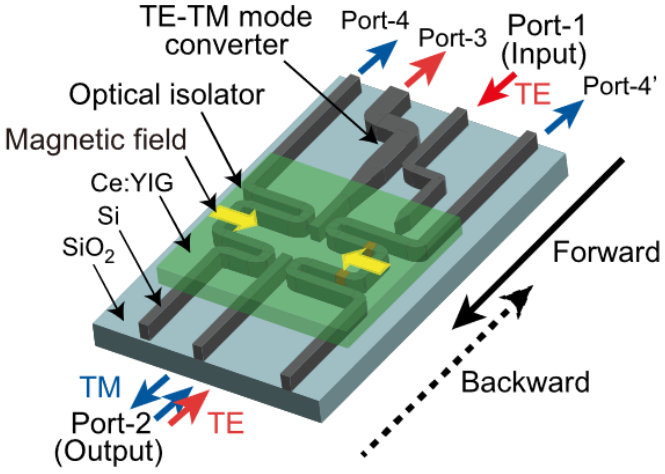

Figure 2.11: Schematic of a MZI-based optical isolator [78].

2) When a Ce:YIG film is deposited on one sidewall of the ring resonator on Si N, as shown in Fig 2.12, the TE propagating light will experience a NRPS under the influence of an out-of-plane magnetic field [79]. This device shows an insertion loss of 11.5 dB and an isolation ratio of 20.0 dB at resonance. Compared to the first solution, this solution does not require an additional mode converter and the device size is much more compact than the devices using the bonding technology. However, the saturated magnetic field of Ce:YIG is over 2000 Oe in the out-of-plane direction. This is not practical if an electromagnet is integrated to apply magnetic field.

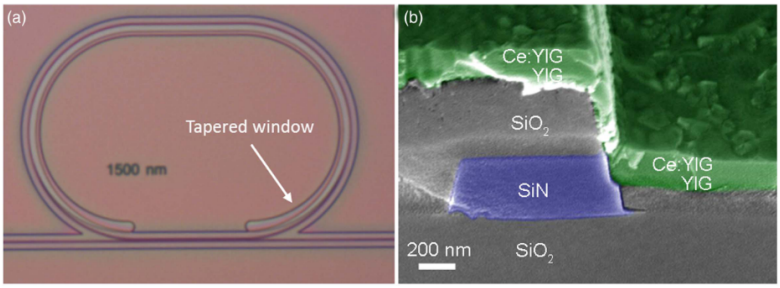

Figure 2.12: Schematic of a ring-based optical isolator [79].

Summaries of integrated optical isolators and circulators based on NRPS are covered in Table 2.3 and Table 2.4, respectively. In these two tables, PLD and bonding techniques are employed to integrate Ce:YIG films with semiconductors. For nonreciprocal devices based on PLD, a YIG layer is directly deposited on Si waveguides as a buffer layer. Then, a polycrystalline Ce:YIG layer is deposited on the YIG layer. A rapid thermal annealing process at 850°C is required to crystallize the Ce:YIG layer. Nonreciprocal devices based on PLD show the advantages of monolithic integration, good performance and compact footprint. However, they also have several drawbacks.

Firstly, the high annealing temperature is undesirable for the integration with other components, especially lasers. Therefore, it is difficult to add the PLD process into the current photonic chip process flow. Secondly, the MO properties of the Ce:YIG film on the Si substrate are impacted due to lattice and thermal mismatch.

For nonreciprocal devices using bonding technique, a relatively low thermal budget (280°C) is required compared with PLD. The laser performance will not be degraded at this temperature. Besides, A high-quality Ce:YIG film can be adopted. This film is sputtered on a SGGG substrate and has high MO qualities as discussed in section 2.2. However, to achieve a large-scale integration of isolators and circulators on PICs, several challenges, such as critical bonding surface quality requirement, bonding layer uniformity control and insertion loss reduction, still need to be overcome.

For nonreciprocal devices based on NRPS, optical isolation is achieved in either MZIs or ring resonators. From Table 2.3, these two kinds of isolators exhibit over 30 dB optical isolation. MZI isolators shows broader optical bandwidth, larger footprint and higher insertion loss than the micro-ring isolators. The optical isolation bandwidth is defined as the wavelength range for which the isolation ratio is more than 20 dB. A maximum 20 dB bandwidth of 8 nm has been achieved in a MZI isolator [81].

Device type	Fabrication method	Polarization	20 dB Bandwidth (nm)	Optical isolation (dB)	Insertion loss (dB)
MZI [56]	Adhesive bonding	TM	0.5	25	9.7
MZI [80]	Adhesive bonding	TE	0.5	32	22
MZI [81]	Direct bonding	TM	8	30	13
MZI [78]	Direct bonding	TE	1	26.7	33.4
MZI [79]	PLD	TM	2	30	5
MZI [79]	PLD	TE	1	30	9
Ring [82]	Direct bonding	TM	<0.1	32	2.3
Ring [18]	Direct bonding	TE	<0.1	25	6.5
Ring [83]	PLD	TM	<0.1	28	1
Ring [79]	PLD	TE	<0.1	20	11.5

Table 2.3: Comparison of integrated optical isolators based on NRPS.

Device type	Fabrication method	Polarization	20 dB Bandwidth (nm)	Optical isolation (dB)	Insertion loss (dB)
MZI [84]	Adhesive bonding	TM	-	22	10
MZI [72]	Direct bonding	TM	-	15.3	11.5
MZI [85]	Direct bonding	TE	1	30	18
MZI [83]	PLD	TM	2	32	2.3
MZI [83]	PLD	TE	1	30	3
Ring [76]	Direct bonding	TM	<0.1	14.4	10.1

Table 2.4: Comparison of integrated optical circulators based on NRPS.

The performance is approaching the requirements for practical applications. Optical isolators and ciculators need to be integrated with lasers to realize their functions. To date, monolithic integrated lasers are not available in the Si platform. Different approaches based on heterogeneous integration with III-V semiconductors have been investigated [86, 87]. However, these approaches bring new challenges (mismatch of waveguide dimensions, critical alignment accuracy) to the integration of isolators and lasers on Si. To the best of our knowledge, a full integration of lasers and isolators has not been realized because of material incompatibility and fabrication complexity.

This thesis aims to achieve integrated optical isolators and circulators in the IMOS platform, which allows the integration of active and passive photonic components, including amplifiers and lasers, on one platform. Design and fabrication of the integrated optical isolators and circulators with DFB lasers will be discussed in Chapter 6.

2.3.3 Integrated polarization-independent optical isolators and circulators

As discussed in section 2.2, the NRPS in a MO waveguide is polarization dependent. For the TM mode, a NRPS can be obtained if the device is asymmetric in the vertical direction and the magnetic field direction is in-plane. The TE mode will experience a NRPS if the device has horizontal asymmetry and the magnetic field direction is

out-of-plane. For the devices listed in Table 2.3 and Table 2.4, nonreciprocal devices based on NRPS can only operate for one polarization state since the magnetic field is fixed in one direction.

Since most semiconductor lasers emit TE mode light, integrated TE optical isolators can meet the needs of eliminating back reflections. Despite this, developing polarization-independent nonreciprocal devices are still attractive for circuit-level applications in PICs, like sensing and signal processing. It is important to prevent reflections with unknown polarization states from impacting the performance of optical components in a circuit.

A concept of a polarization-independent MZI-type integrated optical isolator was proposed in 1999 [88], by using horizontal and vertical magnetic domain walls in the waveguide to simultaneously induce TE and TM nonreciprocal phase shifts, as shown in Fig 2.13. Subsequently, a NRPS of a TE mode was observed in this design [89]. However, to obtain NRPS for the two polarization states, in this design, the direction of the external magnetic field should be perpendicular and transverse to the propagation direction of the light in the two branches, respectively. An optical isolator for both polarizations has not been achieved.

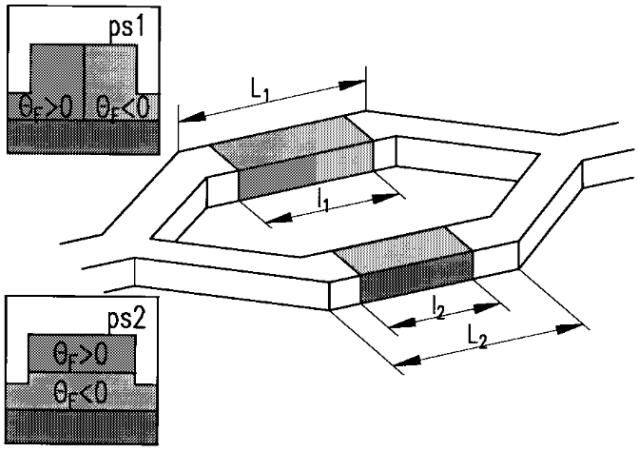

Figure 2.13: Schematic of a polarization-independent optical isolator [88].

Another approach to achieve polarization independence was proposed in 2007 [90]. As shown in Fig 2.14, the isolator is based on a MZI structure. Two PCs are implemented in the two branches. A nonreciprocal phase shifter is created by directly bonding a Ce:YIG layer on the waveguides. An external magnetic field, transverse to the propagation direction of light, is applied. The TM mode can obtain a nonreciprocal phase shift. Thus, a polarization independent optical isolator is achieved by creating phase differences between reciprocal TE and nonreciprocal TM modes in two branches. However, this design is not polarization maintaining. For example, the input TE mode is converted to the TM mode at the output.

To date, integrated polarization-independent optical isolators and circulators have not been experimentally demonstrated. This is therefore a goal of this thesis.

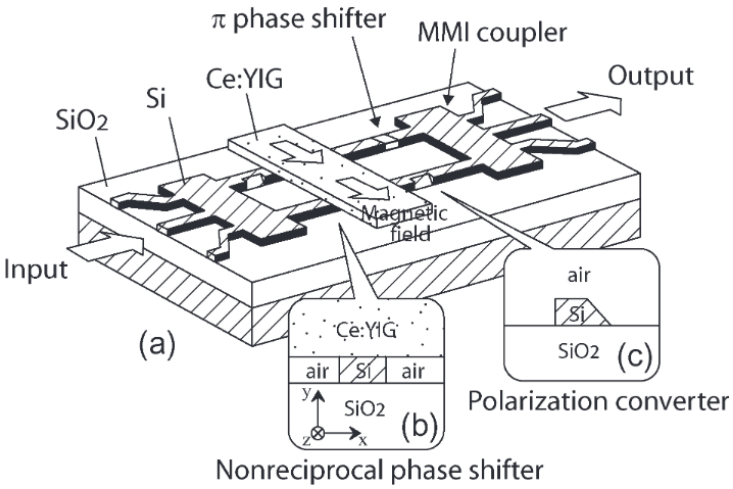

Figure 2.14: Schematic of a polarization-independent optical isolator [90].

2.3.4 Summary

In PICs, integrated optical isolators and circulators can be used to stabilize the lasers. The integration of optical isolators and circulators poses significant design and fabrication challenges, mainly from the incompatibility of magneto-optic material with the semiconductor platforms.

In this chapter, an overview of MO materials that can be implemented in integrated photonics is given. Several reasons behind choosing Ce:YIG for the developments of integrated optical nonreciprocal devices are explained. The origin of magnetism and the theory behind the MO effect in integrated photonics are explained.

Integrated optical isolators based on NRPC, NRL, and NRPS effect are studied. NRPS is preferred among the three effects considering the feasibility of the fabrication process and the device performance. The state of the art of integrated optical isolators and circulators using NRPS is summarized and evaluated. It can be seen that the performance of integrated optical isolators and circulators have made great progress. The achieved high optical isolation and low insertion loss of integrated isolators are comparable to the bulk isolators. However, an integrated optical nonreciprocal device, with broad bandwidth, tunable wavelength, polarization independence, and the ability of co-integrating with lasers, are still absent. This leads to the goal of this thesis: developing designs and technologies to meet these requirements.

Chapter 3

Heterogeneous integration of Ce:YIG with the IMOS platform

As discussed in Chapter 2, bonding techniques have drawn great attention for integrating epitaxial Ce:YIG (Cerium substituted Yttrium Iron Garnet) film grown on single crystalline SGGG ((Ca, Mg, Zr) substituted gadolinium gallium garnet) substrates with semiconductor platforms. Integrated nonreciprocal devices using such bonding techniques have shown great performance on the Si platform.

In this chapter, the question of how to integrate Ce:YIG in the IMOS platform will be answered. Comparison of two different bonding techniques (direct bonding and adhesive bonding) is covered. Simulations on optimizing the MO (magneto-optic) waveguide cross-section are carried out. A Ce:YIG-die-to-InP-membrane adhesive bonding procedure is developed. The observed problems and approaches to improve the bonding yield are also discussed.

3.1 Bonding techniques for heterogeneous integration

Bonding techniques for heterogeneous integration were initially developed to integrate III-V active devices with Si passive devices [91], to overcome the lack of efficient light emission in the latter. Other functional materials, such as $LiNbO_3$ and MO garnets are also bonded onto semiconductor platforms to combine the best properties of each material and to achieve multiple functionalities. There are mainly two bonding techniques developed for heterogeneous integration: direct bonding and adhesive bonding.

3.1.1 Direct bonding

Direct bonding refers to a bonding technique in which the flat surfaces of two dissimilar materials are attached and bonded without any intermediate layer in between.

A plasma-activated direct bonding process has been developed to bond Ce:YIG with Si [55]. The schematic process is illustrated in Fig 3.1. The Si wafer and the

Ce:YIG film are exposed to an oxygen plasma for 30 seconds to remove organic compounds from the surfaces. Fifteen 1.5×1.5 mm^2 Ce:YIG dies are arrayed on a holder. Subsequently, they are brought into contact under a pressure of 1 MPa, and are heated to 200 °C in high vacuum (10^{-4} Pa). The backside of the garnet is chamfered to apply the bonding pressure to the center of the chip and avoid stress concentration at the edge of the contact side. A photograph of samples of garnet dies bonded on SOI is shown in Fig 3.1(c).

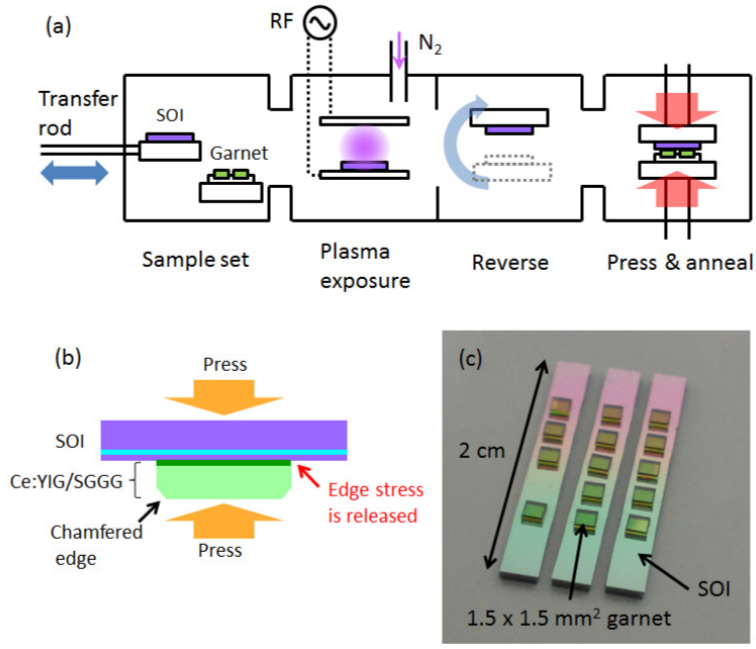

Figure 3.1: Schematic of the surface activated direct bonding process [55].

After the bonding process, a tight and uniform contact of a Ce:YIG cladding on a waveguide is created. A large NRPS (nonreciprocal phase shift) can be achieved for the TM mode light under the influence of a transverse magnetic field [92], because of the absence of the intermediate bonding layer. A 32 dB optical isolation has been achieved for optical isolators using this bonding technique [82].

However, there are also two drawbacks: (1) it requires critical (ultra-flat, clean and contamination-free) surface conditions before the two wafers can be bonded. (2) Cracks associated with thermal stress are observed in some waveguides. At least 30 dB propagation loss was measured due to the formation of cracks [93]. This is because the Ce:YIG film has a large thermal expansion coefficient (10.0 × 10^{-6}/K) [94] compared to Si (2.6 × 10^{-6}/K).

3.1.2 Adhesive bonding

Adhesive bonding is a bonding technique in which an intermediate adhesive layer is used between two dissimilar wafers. By far, BCB is widely used for adhesive wafer bonding. It shows excellent physical properties, such as low dielectric constant, low moisture absorption, low curing temperature, high degree of planarization, good thermal stability and excellent chemical resistance [57]. An integrated optical isolator on Si with 25 dB optical isolation using a 102 nm thick BCB bonding layer has been achieved [56]. Fig 3.2 shows a photograph of the SOI chip with the Ce:YIG die bonded on top and a SEM image of the cross-section of the bonded stack. A more detailed explanation of this bonding technique will be given in section 3.3.

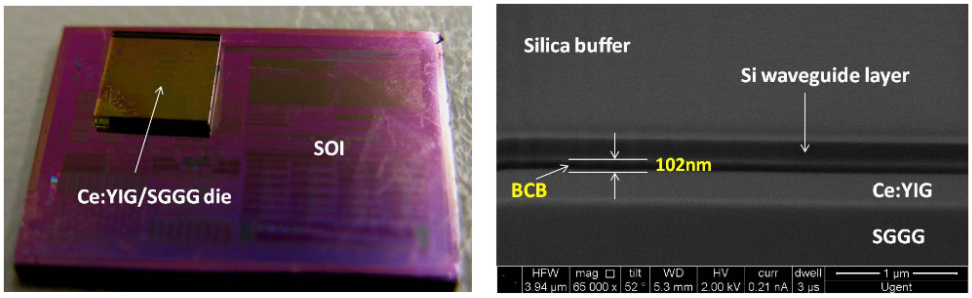

Figure 3.2: Schematic of the BCB adhesive bonding process.

During the bonding process, the liquid phase BCB can fill all the voids and gaps at the bonding interface, which makes this technique tolerant to surface topology, particle contamination and surface roughness. There is also less formation of cracks because of its relatively low thermal stress. This bonding technique is already in use for the IMOS platform.

3.1.3 Evaluation

Table 3.1 shows the comparison of two bonding techniques.

Property	Plasma-activated direct bonding	BCB adhesive bonding
Bonding temperature	200 °C - 300 °C	~250°C
Tolerance to surface topology	low	high
Tolerance to particle contamination	low	high
Planarization capability	no	yes
Interface thickness	1 nm - ~100 nm	10 nm - few μm

Table 3.1: Comparison of two bonding techniques.

Compared with the plasma-activated direct wafer bonding technique, the BCB adhesive bonding technique is less sensitive to surface roughness and particle contamination of the bonding surfaces. The planarization capability of this technique enables bonding Ce:YIG films on wafers with topology.

Light propagating in the waveguide bonded with the Ce:YIG will be evanescently coupled into the Ce:YIG cladding layer. Compared with the plasma-activated direct wafer bonding technique, the BCB layer will decrease the interaction between the evanescent wave and the Ce:YIG layer, so the footprint of devices using this bonding technique is larger.

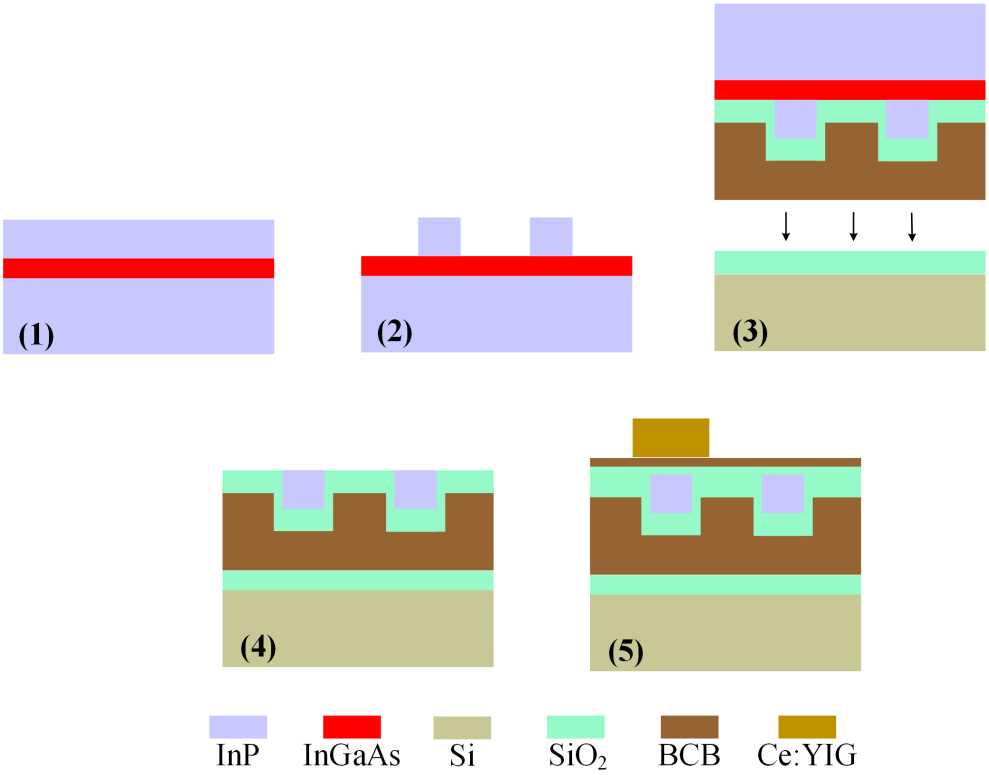

Figure 3.3: Schematic of the bonding process flow. (1) The passive layer stack of a passive IMOS wafer. (2) After waveguide definition. (3) Adhesive bonding of InP on Si. (4) Removal of the InP substrate and the etch-stop layer. (5) Adhesive bonding of Ce:YIG on the IMOS wafer.

The BCB adhesive bonding technique has been investigated and developed for the IMOS platform to adhesively bond the InP membrane to a Si wafer. Fig 3.3 shows the schematic of the bonding process flow in a passive IMOS platform. The passive IMOS wafer consists of an InGaAs etch-stop layer and an InP membrane waveguide layer. The InP waveguides are defined by a lithography step. A layer of SiO_2 is deposited on the membrane to increase the adhesion of BCB. Subsequently, a layer of BCB is

spun on the SiO_2 layer. Another layer of SiO_2 is deposited on the Si wafer. Then, the InP wafer is flipped, aligned and attached to the Si wafer. The InP substrate and the InGaAs sacrificial layer are wet chemically removed. Finally, a Ce:YIG die is attached on the IMOS wafer with a SiO_2 layer and a BCB layer in between.

In this chapter, an ultra-thin BCB adhesive bonding technique is developed for integrating the Ce:YIG dies with the InP membrane in order to enhance the MO interaction.

3.2 Optimization of the magneto-optic interaction

As is discussed in Chapter 2, the idea is to bond the Ce:YIG layer on the InP waveguide, so that the TM mode can be evanescently coupled to the Ce:YIG layer and experience NRPS. In order to achieve a sufficient NRPS, the design parameters, such as the thickness of the bonding layer and the length of the Ce:YIG layer, need to be optimized to enable strong evanescent coupling, while reducing optical absorption loss from the Ce:YIG layer. In the meanwhile, the presence of the bonded layer brings extra loss and reflection, due to mode mismatch at the interface. It is important to find a trade-off between these device performances and the footprint in simulations.

The typical InP waveguide in the IMOS platform is 400 nm in width and 300 nm in height. The electric field distributions of the fundamental TE and TM modes are analyzed using a finite difference eigenmode (FDE) solver and are shown in Fig 1.6. Once the BCB bonding process to the Si wafer is performed, another thin SiO_2 layer is deposited on the waveguide to enhance the adhesion between InP and BCB. In this thesis, the thickness of the SiO_2 is 50 nm deposited by a plasma-enhanced chemical vapor deposition (PECVD) tool. This thickness can be reduced by reducing the deposition time in PECVD or using an Atomic layer deposition (ALD) tool. Then, the InP waveguide is covered with a thin BCB layer. The target thickness of the BCB layer is 72 nm since in subsequent simulations it is found that this is required to achieve a sufficient NRPS for a 4 mm long Ce:YIG cladding. A 500 nm Ce:YIG layer (refractive index: 2.2) on a SGGG substrate (refractive index: 1.9) is bonded on top of the BCB and serves as a top-cladding layer.

The electric field profile of the fundamental TE mode is shown in Fig 3.4(a). Discontinuities of the electrical field are observed at different interfaces. The electrical distribution in the vertical direction is found in a vectorial mode solver and is shown in Fig 3.4(b). It can be seen that the TE mode is still mostly confined in the InP waveguide. The calculated confinement factor in the Ce:YIG layer is 5.3% if the thickness of the bonding layer is 122 nm and is 16.8% if there is no bonding layer beteen the InP waveguide and the Ce:YIG layer. Although there is no NRPS for the TE mode, as is discussed in Chapter 2, the evanescent coupling of the TE mode still contributes to extra insertion loss because of the optical absorption from the Ce:YIG layer.

The electric field profile and the electric field distribution in the vertical direction of the fundamental TM mode are shown in Fig 3.5(a) and (b), respectively. It can be seen that a large portion of the electrical field is confined in the bonding layer. For the TM mode, the confinement factor in the Ce:YIG layer is 17.4% if the thickness of the bonding layer is 122 nm and is 39.9% if there is no bonding layer. The optical

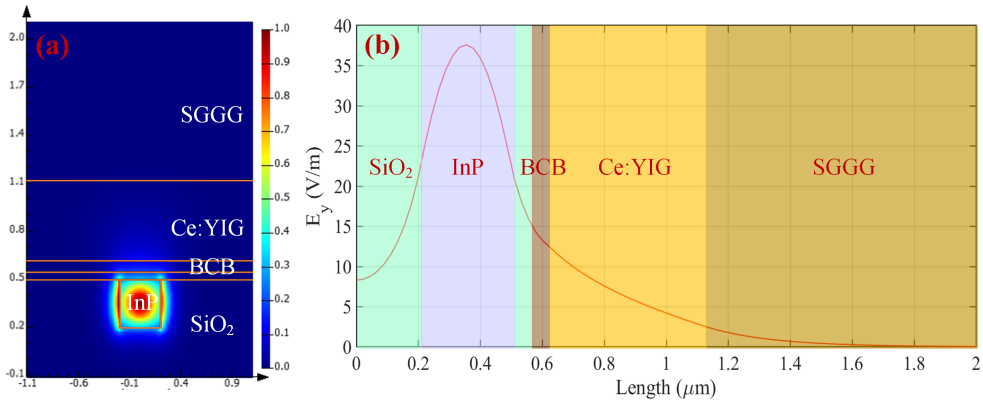

Figure 3.4: (a) Electrical field profile of the TE mode in a Ce:YIG covered waveguide. (b) Electric field distribution of the TE mode in the vertical direction.

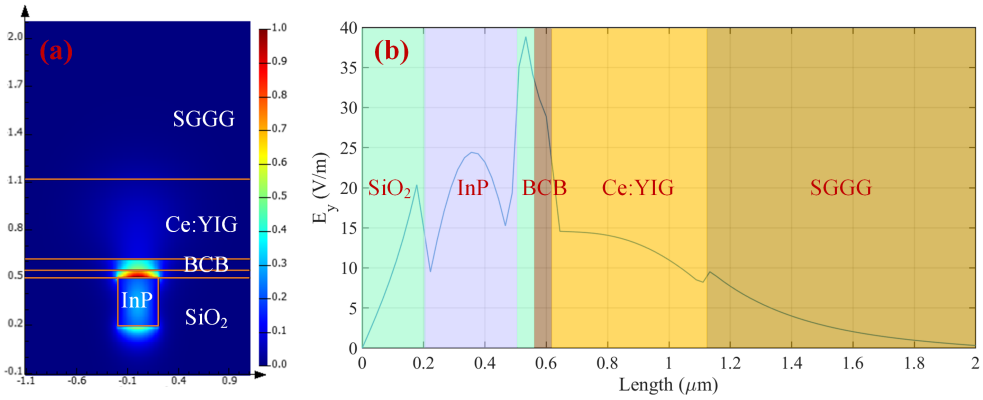

Figure 3.5: (a) Electrical field profile of the TM mode in a Ce:YIG covered waveguide. (b) Electric field distribution of the TM mode in the vertical direction.

absorption loss of the Ce:YIG at 1550 nm is 42 dB/cm [55]. So, the calculated absorption losses of the 4 mm long Ce:YIG are 2.9 dB and 6.7 dB. In the meanwhile, the calculated confinement factor of the TE mode is 5.3% if the thickness of the bonding layer is 122 nm and 16.8% if there is no bonding layer. The calculated absorption losses are 0.9 dB and 2.8 dB.

As analyzed in section 2.2, only the evanescent wave of the TM mode interacts with the Ce:YIG layer, and experiences a NRPS when the Ce:YIG layer is magnetized along the transverse direction. NRPS will be affected by several parameters (size of Ce:YIG die, Faraday rotation coefficient of Ce:YIG, BCB thickness). In this case, Ce:YIG is sputtered on a SGGG substrate and has a Faraday rotation coefficient of 4500 °/cm at 1550 nm. NRPS as a function of the thickness of BCB layer can be analyzed using a finite-difference time-domain (FDTD) solver.

To model the NRPS effect in the FDTD solver, two permittivity tensors for forward

and backward propagation fields are written as:

$$\varepsilon_{\text{forward}} = \begin{bmatrix} 2.2^2 & 0 & \varepsilon_{xz} \\ 0 & 2.2^2 & 0 \\ -\varepsilon_{xz} & 0 & 2.2^2 \end{bmatrix} \tag{3.1}$$

$$\varepsilon_{\text{backward}} = \begin{bmatrix} 2.2^2 & 0 & -\varepsilon_{xz} \\ 0 & 2.2^2 & 0 \\ \varepsilon_{xz} & 0 & 2.2^2 \end{bmatrix} \tag{3.2}$$

where $\varepsilon_{xz} = ig_y$ and g_y=0.009 corresponds to the 4500 °/cm Faraday rotation coefficient of Ce:YIG [95]. The TM mode light will experience different propagation constant in the forward and backward directions. The NRPS can be expressed as:

$$\text{NRPS} = (\beta_{\text{forward}} - \beta_{\text{backward}}) \cdot L \tag{3.3}$$

where β_{forward} and β_{backward} are the propagation constants of the TM mode light in forward and backward propagation, respectively. L is the length of the waveguide coated with Ce:YIG. NRPS at a wavelength of 1550 nm for different BCB thicknesses in opposite propagating directions is calculated and is shown in Fig 3.6.

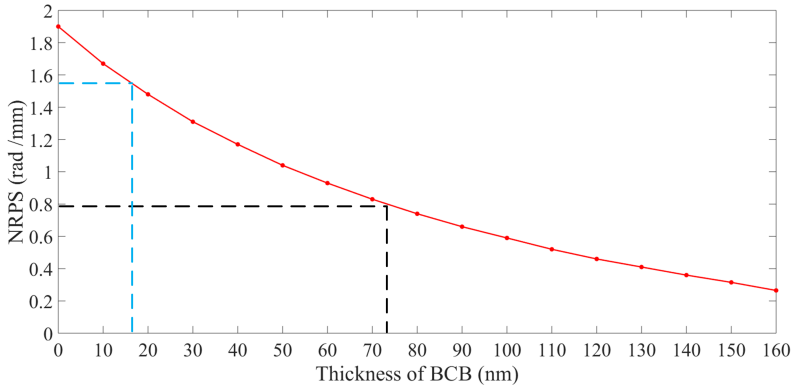

Figure 3.6: NRPS of TM mode as a function of BCB thickness at a wavelength of 1550 nm.

The simulation results show that the NRPS is decreasing with increased BCB thickness. A thin BCB layer is needed to achive an optical isolator with compact dimension. The NRPS decreases more slowly for thicker BCB layer. This means there will be more fabrication tolerance for thicker BCB layer. The black dashed line in Fig 3.6 indicates that at most a 72 nm thick BCB layer is needed to reach π NRPS for Ce:YIG with 4 mm length. The blue dashed line indicates that at most a 18 nm thick BCB layer is needed to reach π NRPS for Ce:YIG with 2 mm length.

Owing to the mode mismatch between the waveguide with air cladding and the waveguide with Ce:YIG cladding, loss and reflection are induced at the interface.

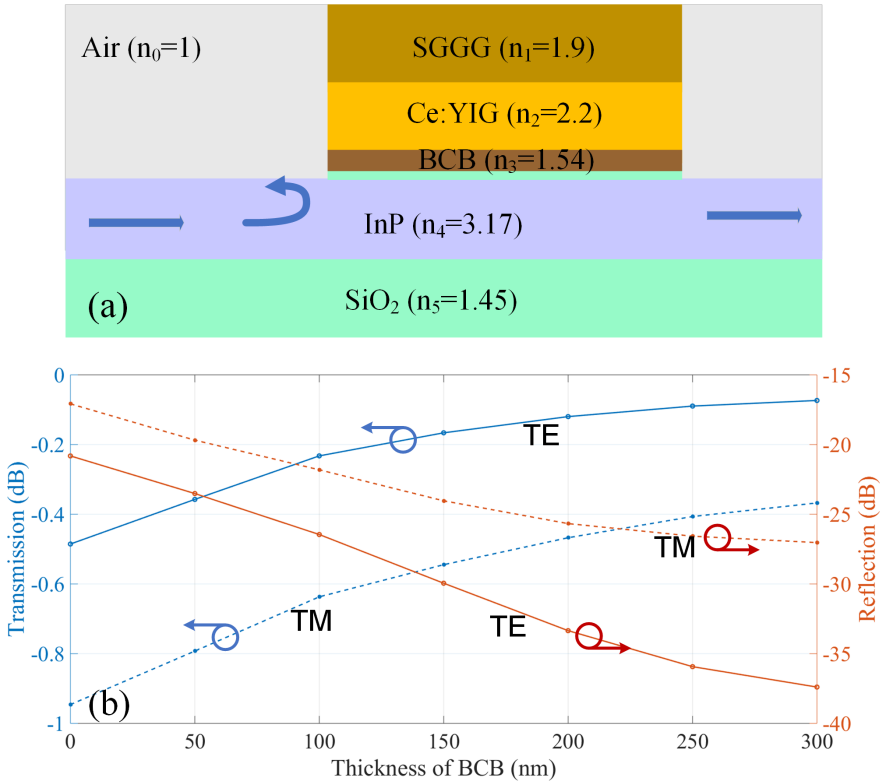

Figure 3.7: (a) Side view of the InP waveguide bonded with the Ce:YIG. (b) Transmission and reflection at the interface as a function of the BCB thickness.

This is affected by the thickness of the bonding layer, as indicated in Fig 3.7(a). In Fig 3.7(b), transmission and reflection at the interface as a function of the BCB thickness for the TE and TM mode at a wavelength of 1550 nm are simulated in a FDTD solver.

It can be seen that the transmission is increasing, and the reflection is decreasing with increasing BCB thickness for both TE and TM mode. The TM mode in the cladding undergoes more reflection than the TE mode because of its larger confinement factor. In simulation, it is assumed that the Ce:YIG layer has no optical absorption. When the thickness of BCB is 72 nm, the transmission loss in the waveguide with Ce:YIG cladding for the two polarization states is below 1 dB and the reflection is below 20 dB. In practice, the optical absorption of the Ce:YIG layer is about 5 dB/mm in the near infrared wavelength region [78], and an increased BCB thickness will also decrease the optical absorption in the Ce:YIG layer.

In summary, for a 4 mm long Ce:YIG die, a BCB thickness of 72 nm is found to guarantee sufficient NRPS while shortening the device dimension, reducing the insertion loss and maintaining the fabrication tolerance.

3.3 Ce:YIG-die-to-IMOS-wafer bonding process

The subject of this section is the development of a Ce:YIG-die-to-IMOS-wafer bonding process with the optimized design parameters found in simulations.

3.3.1 Description of the bonding procedure

A general description of the Ce:YIG-die-to-IMOS-wafer bonding process is illustrated in Fig 3.8.

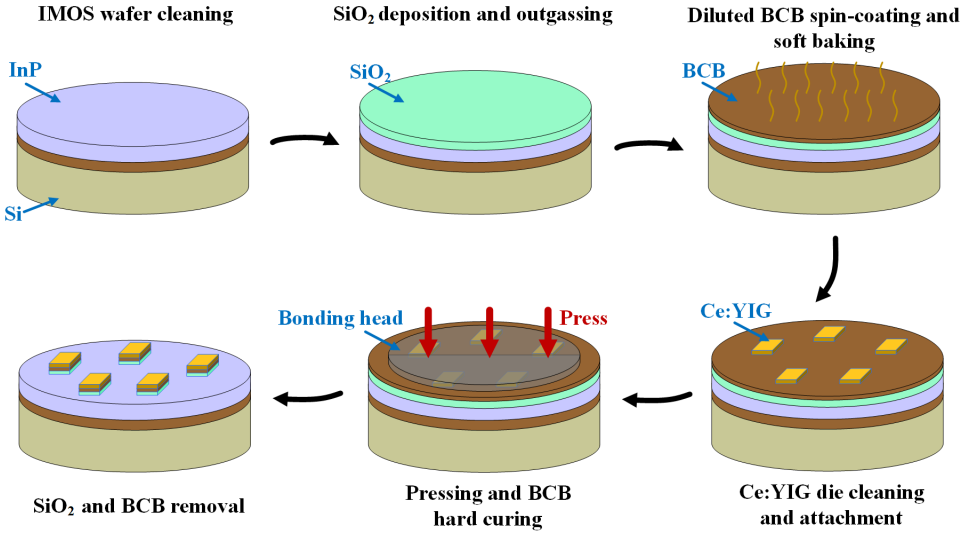

Figure 3.8: The Ce:YIG-die-to-IMOS bonding process.

First, a surface cleaning process is performed. A processed 3 inch IMOS wafer is rinsed in Acetone, Isopropylalchohol (IPA) and ultra pure water (UPW) consecutively to remove particles from the wafer surface. Immediately afterwards, an oxygen plasma stripping process is performed to remove organic residuals on the surface. Subsequently, a diluted H_3PO_4 rinsing step is used to remove semiconductor oxides after oxygen stripping.

A 50 nm SiO_2 layer is deposited on the wafer as an adhesion layer for BCB. Then, the wafer is baked at 280 °C in a vacuum oven in order to evaporate any water vapor and to remove remaining gaseous inclusions in SiO_2.

Before BCB spin-coating, a layer of adhesion promoter AP3000 is spin-coated and soft-baked at 135 °C for 5 minutes, to improve the adhesion of BCB on SiO_2. Then, a layer of diluted BCB is spin-coated on the SiO_2 layer. Next, the wafer is soft-baked to evaporate the remaining solvent from the BCB. The temperature for soft-baking is 135 °C, with a ramp of about 5 °C/min.

Multiple Ce:YIG dies (4×4 mm^2) are cleaned using Acetone and IPA. They are attached on the IMOS wafer using vacuum tweezers. The length of the InP waveguides

for Ce:YIG bonding is about 6 mm. Thus, a precise alignment of Ce:YIG dies on the InP waveguides is not required. The alignment has a tolerance of about 2 mm. In a microscope, the four corners of the Ce:YIG die can be aligned with the four markers on the IMOS wafer by mechanical tweezers, with a precision of about 1 mm. However, this process is time-consuming as all the Ce:YIG dies are attached and aligned manually. This process may also cause particle contamination, which could compromise the bonding quality. In the future, an automatic pick and place tool is expected to speed up this process and to avoid contamination.

Following the process of attachment and alignment, the Ce:YIG dies and the IMOS wafer are loaded in the bonder. The bonding process starts with evacuating the chamber to 1×10^{-3} mbar and increasing the temperature to 50 °C with a gradient of 5 °C/min. Immediately afterwards, the bonding head moves downwards, and applies 170 compression force on the Ce:YIG dies for 30 seconds. Since the area of the bonding head is much larger than the wafer, the actual bonding area is the total area of the Ce:YIG dies. Therefore, the number of the Ce:YIG dies will affect the actual bonding pressure. Then, the Ce:YIG dies and the IMOS wafer are brought into contact for 10 minutes at a temperature of 140 °C. The BCB layer is still in a liquid phase at this temperature, so it can fill in the voids at the bonding interface. Then, the pressure of the chamber increases to 800 mbar with a N_2 atmosphere. The dies and the wafer reach to 280 °C with a gradient of 5 °C/min. The full cross-linking of the BCB layer is achieved at this temperature. Finally, the chamber is cooled to 50 °C and the sample is ready to be unloaded.

In the IMOS platform, the center wavelength of the grating couplers, used for coupling light into and out of the chip, is optimized at 1550 nm with an air cladding. The presence of the bonding layers on the grating couplers will cause an unwanted wavelength shift. Therefore, after the bonding process is finished, a RIE process is performed to etch away the SiO_2 and BCB layer outside of the bonding area. A SEM image of the waveguides entering the bonded Ce:YIG region is shown in Fig 3.9(a). PCs can also be observed in this image. A photograph of the IMOS wafer bonded with two Ce:YIG dies is shown in Fig 3.9(b).

3.3.2 Experiments and analysis

Bonding experiments are carried out to develop a reliable Ce:YIG-die-to-IMOS-wafer bonding process, which not only reaches the target thickness of BCB in the previous section, but also achieves high bonding yield.

- Ce:YIG preparation and cleaning

  A 500 nm Ce:YIG film is deposited on a 3 inch (111)-oriented SGGG substrate (500 μm in thickness). A blade dicing saw is used for cutting the wafer into dies with different dimensions, as shown in Fig 3.10(a). The Ce:YIG dies are attached on a dicing tape, and can be peeled off directly without any treatment. The Ce:YIG surface is upside down and protected by a layer of photoresist, which can be removed with boiling Acetone. Currently, boiling Acetone is not available in our cleanroom. It is found that submerging the Ce:YIG dies in

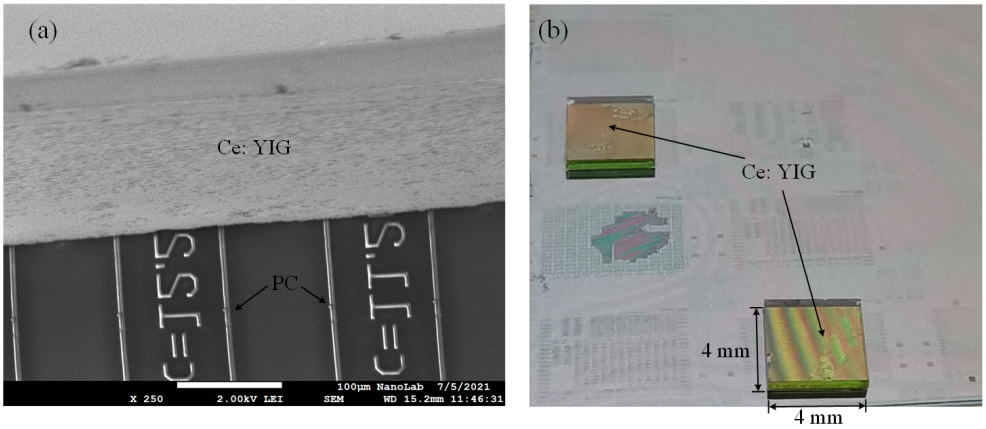

Figure 3.9: (a) A SEM image of the waveguides entering the bonded Ce:YIG region. (b) A photograph of the IMOS wafer bonded with Ce:YIG dies.

Acetone at room temperature cannot completely remove the photoresist layer in the experiment.

The Ce:YIG dies are transparent, so it is hard to determine the front side and back side. Since the blade is cut into the wafer from the backside, where at the top surface about 50 µm is remained. The different sides can be confirmed by observing the cutting edge, as shown in Fig 3.10(b).

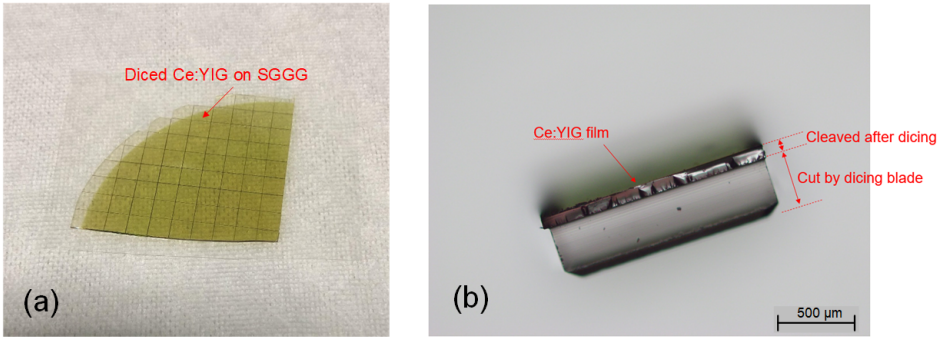

Figure 3.10: (a) A quarter of diced Ce:YIG on SGGG. (b) Side view of a Ce:YIG on SGGG die.

Fig 3.11 is a microscope image of the side view of a Ce:YIG die. There are residues of photoresist left on the surface, which could become local defects during the bonding process.

Thus, an alternative is using an ultrasonic cleaning process. The Ce:YIG dies are submerged in Acetone in a beaker, which is kept in a ultrasonic cleaner for 15 minutes to completely remove the photoresist layer. Afterwards, the Ce:YIG dies are submerged in IPA and UPW to remove residual Acetone.

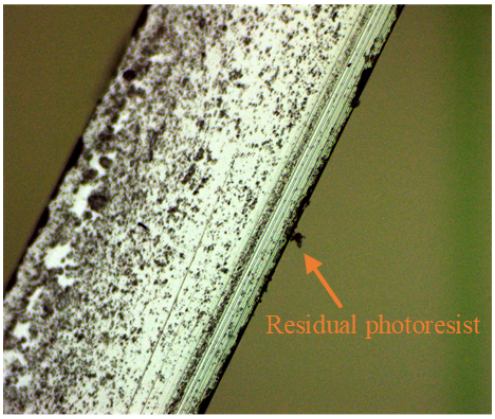

Figure 3.11: Side view of a Ce:YIG die in microscope.

- Thickness of the BCB layer

  The BCB thickness can be varied by three parameters: i) the bonding pressure. ii) the BCB to solvent(mesitylene) dilution ratio. iii) the rotation speed during the spin-coating of BCB. To obtain sub-100nm thick BCB layers, the dilution of BCB becomes the only effective way [96]. In simulations, for Ce:YIG dies with 2 mm and 4 mm in length, the target thicknesses of the BCB layer are 18 nm and 72 nm, respectively. To reach these target values, two different BCB dilution ratios (Cyclotene 3022-46: mesitylene 1:5 v/v and Cyclotene 3022-35: mesitylene 1:8 v/v) are prepared. The rotation speed is set at 4000 rpm for 30 seconds to produce an uniform film after spin-coating [97].

  An IMOS wafer bonded with Ce:YIG dies is cleaved to measure the BCB thickness. Diluted BCB (1:5 v/v) is spin-coated on the IMOS wafer. A scanning electron microscope (SEM) image of the cross-section of the bonded wafer is shown in Fig 3.12. The Ce:YIG die is not present in the image since it came off during the cleaving process. The measured thickness of the bonding layers (a SiO_2 layer and a BCB layer) is around 125 nm. It is difficult to tell the boundary between the SiO_2 and BCB in SEM. This measurement result matches well with the target value.

  Another method is also developed to measure the BCB thickness. First, an InP die is bonded on a Si wafer using diluted BCB. Then, the InP die is wet-etched in a diluted HCl solution. The BCB layer is exposed, and its thickness can be measured using a film thickness measurement tool. The measured thickness is 73 nm for diluted BCB (1:5 v/v) and 26 nm for diluted BCB (1:8 v/v) with over 0.997 goodness of fit. According to the simulation results in Fig 3.8, these two BCB thicknesses are close to the values needed for reaching π rad NRPS, when the length of the Ce:YIG die is 4 mm or 2mm.

- Observed issues and analysis

  The first issue is that the planarization step before bonding Ce:YIG brings extra

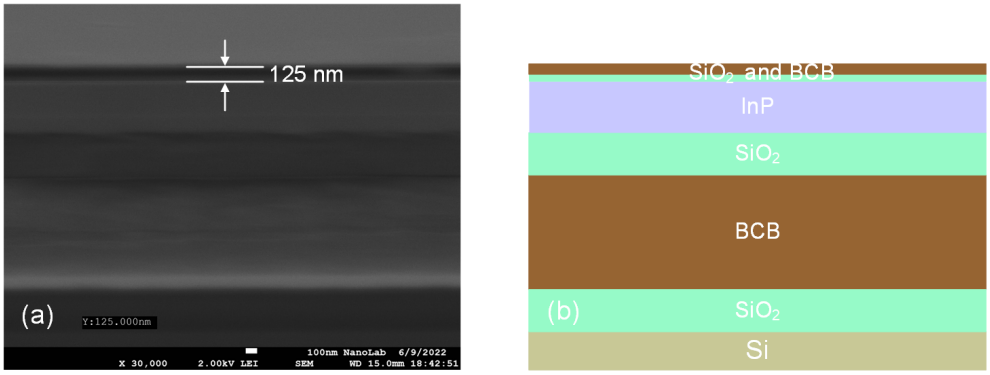

Figure 3.12: (a) SEM image of the cross-section of the IMOS wafer with a thin bonding layer on the surface. (b) Identification of different layers in (a).

propagation loss. As is shown in Chapter 1, the polarization converter(PC) in the IMOS platform contains two InP layers and a InGaAs etch-stop layer. The height of the PC is 460 nm to ensure an optimized overlap of the hybrid modes with the modes in the rectangular waveguide, which is 300 nm in height. During the fabrication process, one side of the PC is etched together with the waveguide, as shown in Fig 3.13(a). The etch depth must be over 460 nm to ensure the vertical sidewall of the PC is fully opened. Hence, after bonding the InP membrane to Si, there are SiO_2 pillars sticking out on both sides of the IMOS waveguides and PCs, as shown in Fig 3.13(b).

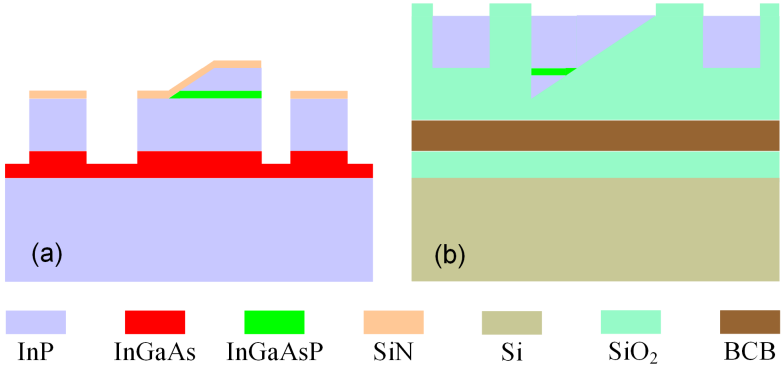

Figure 3.13: (a) Definition of the waveguide and the vertical sidewall of the PC. (b) SiO_2 sticking out of the surface after bonding the InP membrane to Si.

The excess SiO_2 pillar is over 160 nm and the thickness of bonding layer is around 120 nm, which is not thick enough to planarize the surface. To improve the bonding yield, a planarization step is needed before bonding. The SiO_2 layer can be removed using a CHF_3 based RIE step. Ideally, the etch depth is precisely controlled, and a flat surface can be obtained after etching. In reality,

since the etch rate is not exactly controllable and is not uniform over the 3 inch wafer, the SiO_2 layer is sometimes overetched, as shown in Fig 3.14. It can be seen that the sidewall of the InP waveguide is quite rough. This is because the InP waveguide is exposed in CHF_3 for 10 minutes and is slightly etched (in the order of 10 nm). About 20 dB propagation loss is added after this planarization step, as is found by measuring the transmittance of two cascaded TE grating couplers with a 100 μm long waveguide in between, before and after this step.

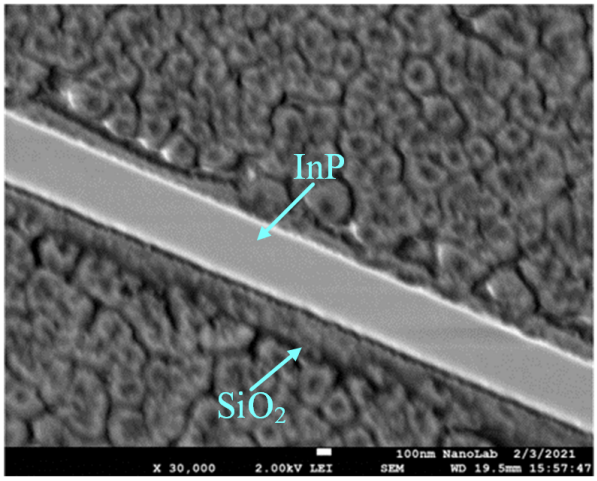

Figure 3.14: SEM image of the waveguide after a CHF_3 based RIE step.

Therefore, the etch time should be shortened to avoid over etch. The diluted BCB can still planarize the surface if the SiO_2 layer is less than the thickness of the BCB. Two other solutions can be applied to skip this planarization step: (1) the definition of the vertical sidewall of the PC and the waveguide can be separated in two lithography steps. The etch depth of the waveguide is controlled to 300 nm. (2) Replace the deep-etched waveguides with shallow-etched waveguides, and connect the waveguides and the PCs with shallow-to-deep waveguide transitions. More details regarding the shallow-to-deep waveguide transitions can be found in Chapter 6.

The second issue is the presence of particles on the wafer. Although the BCB bonding technique has more tolerance to particles than the direct bonding technique, it is still critical to prevent particles from the bonding layer. Particles that are smaller than the bonding layer can be enveloped in the bonding layer and do not affect the bonding quailty. However, in fact, most of the particles are thicker than the bonding layer. These particles may become defects to the bonding layer and cause a local separation of the IMOS wafer and the Ce:YIG die. The bond strength will be reduced, or even no adhesion will be present.

From my experience, the particles mainly come from two different sources:

(1) *From the diluted BCB solution*

The diluted BCB is prepared and kept in a small glass bottle in our cleanroom. A pipette is used to transfer the solution to the wafer. It has been observed in microscope that plenty of particles are present on the surface of the wafer, directly after BCB spinning, as shown in Fig 3.15(a). The diameters of the particles vary from tens of nanometers to a few micrometers, measured in a step height measurement tool. It is suspected that these particles may come from the diluted BCB bottle, or from the dilution process, or from impurities in the solvent.

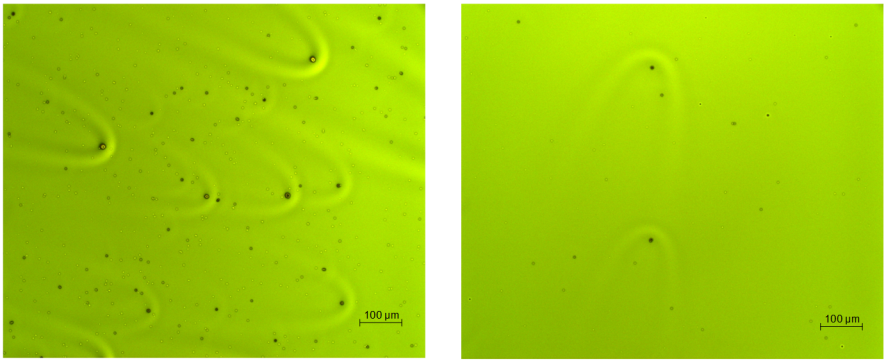

Figure 3.15: Microscope images of the surface of the wafer after BCB spinning. The diluted BCB solutions are from two different bottles: (a) bottle 1 and (b) bottle 2. Bottle 1 has been prepared three months before bottle 2.

A bonding test is carried out to verify this issue. Two diluted BCB bottles with the same dilution ratio and the same dilution process are tested. The only difference is that bottle 1 has been prepared three months before bottle 2. Two Si wafers are covered with 50 nm SiO_2 layers and are baked in a vacuum oven overnight. Then, the two wafers are spin-coated with a layer of AP3000 and are soft-backed on a hot plate. The two wafers are inspected in the microscope after every step to check if there are any visible particles. Then, diluted BCB from the two bottles are spin-coated on the two wafers, respectively.

Fig 3.15 (a) and (b) are the microscope images of the surfaces of the two wafers. Although it is hard to quantify the number of particles, it is clear that there are less particles from bottle 2. One explanation is that these particles are actually coagulations. The BCB molecules will coagulate if it is exposed to air frequently or expired.

It is not clear whether these particles will directly result in bonding failure. One concern is that this may affect the electric field distribution of the optical modes when they are located around the trenches, as shown in Fig 3.16. It is therefore still prudent to avoid these particles.

(2) *From human origin*

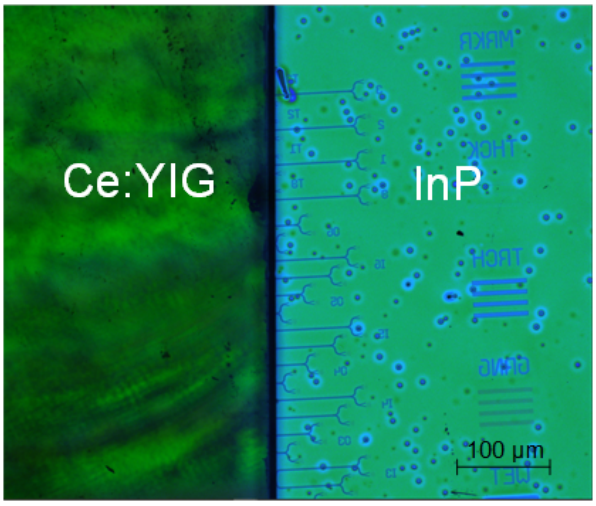

Figure 3.16: A microscope image of the InP membrane bonded with a Ce:YIG die. Particles are visible on the surface of the membrane.

Besides the coagulations observed in the bonding layer, there is also another kind of particle appearing on the wafer surface. Fig 3.17(a) is the microscope image of a failed bonding. It can be seen that particles with various of shapes are present in the bonding area. Outside of the bonding area, the surface looks clean in microscope. So, it is unlikely that these particles are from the diluted BCB bottle. A zoom-in image of one of the particles is shown in Fig 3.17(b), revealing a fiber-shape particle at the center. The measured thickness is around 60 µm. This large particle traps air around it during the bonding process and bubbles are formed around it. The presence of this large particle causes a complete bonding failure.

In another bonding test, the bonding strength is so low that the Ce:YIG die can be easily taken off with tweezers. An observation is that the BCB layer is not uniform at the bonding area. In Fig 3.18(a), the solution is mostly concentrated on the InP membrane and forms various long bubble-like strips. It can be seen that these stripes are mostly present between the wavguides. This might be because the sticking-out SiO_2 pillars are under-etched and cause topology on the surface. The diluted BCB is too thin to planarize the surface. The solution tends to stay on the flat membrane instead. Another observation is that the waveguide is broken after the bonding process, as shown in Fig 3.18(b). It seems that particles either from the wafer or the Ce:YIG die are located on the waveguide and are pressed into it when the force is applied during bonding.

These large particles are most likely fibre from clothing, paper and atmospheric contaminants from breath. The chance of particles attaching on the wafer surface increases significantly when handling multiple Ce:YIG dies with tweezers and aligning them on the waveguides manually. Although the operator tries to

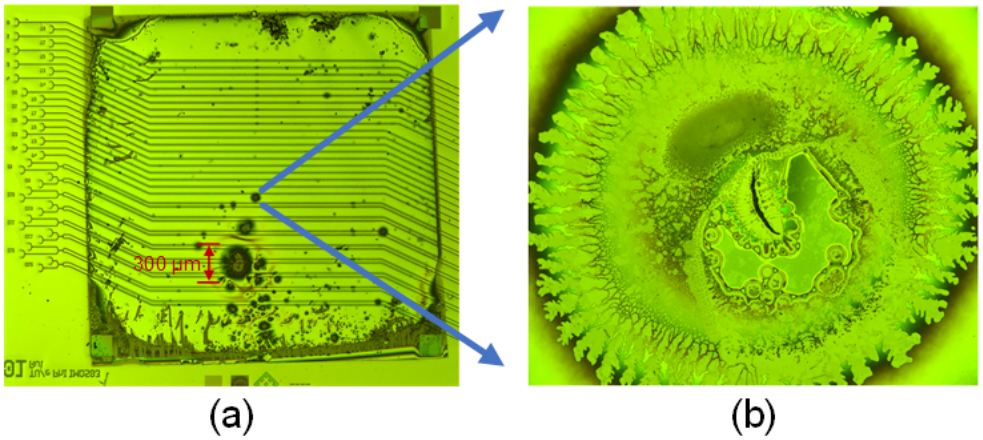

Figure 3.17: (a) Microscope image of the failed bonding area. (b) Microscope image of a local defect in the failed bonding area.

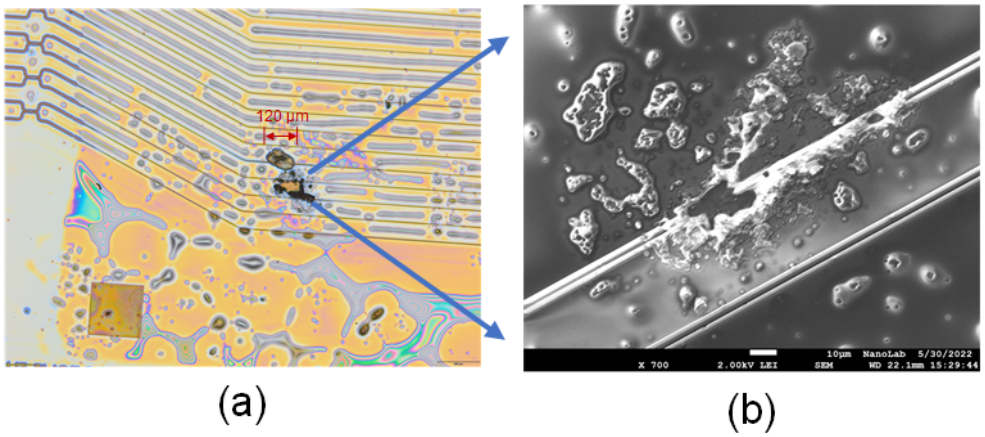

Figure 3.18: (a) Microscope image of the failed bonding area. (b) SEM image of the failed bonding area.

work as cleanly as possible, it is still difficult to prevent particles from getting onto the wafer.

- Multiple-Ce:YIG-die-to-InP-membrane bonding tests

  According to the aforementioned bonding procedure, a series of multiple-Ce:YIG-die-to-InP-membrane bonding tests were carried out. The 3 inch IMOS wafer was cleaved into four quarters. A 73 nm thick BCB layer is spin-coated on the IMOS wafer. Five 4×4 mm^2 Ce:YIG dies are aligned on the wafer surface. After the bonding process, an initial tensile test was performed to evaluate the bonding strength between the Ce:YIG die and the wafer

surface. A piece of tape was attached to the backside of the Ce:YIG die. Then, the tape was pulled up until it left the Ce:YIG die. It can come to a conclusion that the bonding strength is reliable for further characterization. Unfortunately, due to time constraint, only four tests were carried out using 4×4 mm^2 Ce:YIG dies. The achieved bonding yields are 60%, 40%, 80%, 40%, respectively.

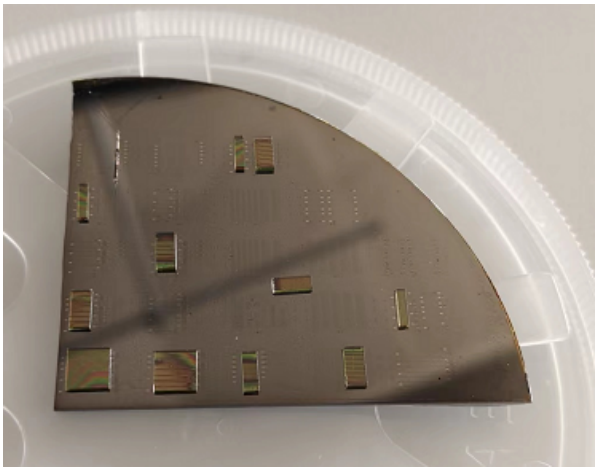

Figure 3.19: Picture of the IMOS wafer bonded with eleven Ce:YIG dies.

Another bonding test was performed using a 26 nm BCB layer. In this test, twenty Ce:YIG dies were placed on the wafer, and eleven Ce:YIG dies were bonded eventually. Fig 3.19 shows the picture of a quarter of IMOS wafer bonded with eleven Ce:YIG dies with lengths from 1 mm to 4mm[1]. The excess BCB outside of the bonding area is etched away in a RIE machine. A downside of this bonding procedure is that all the Ce:YIG dies were attached and aligned individually, which is a time-consuming work and may bring particles onto the wafer surface. An automatic pick and place tool can improve the bonding efficiency and yield.

3.4 Summary

In this chapter, a heterogeneous integration technique for the integrated optical isolators and circulators on the InP membrane platform is presented. A multiple-Ce:YIG-die-to-InP-membrane adhesive bonding procedure is developed. An ultra-thin BCB bonding layer is achieved to adhesively bond multiple Ce:YIG dies to the InP membrane. The measured thicknesses of BCB are 26 nm and 73 nm, respectively, which are sufficient for evanescent coupling of a 2 mm and a 4 mm long Ce:YIG die. This heterogeneous integration technique also offers the potential of bonding other functional materials on the InP membrane platform.

[1]A complete list of Ce:YIG dies used in this thesis can be found in Appendix A.

Two main observed problems are shown and analyzed. A proper planarization step is inevitable for the current design to improve the bonding quality. Two possible solutions are discussed to avoid this planarization step in the future design. Particles are always observed during the bonding process. A series of bonding tests show that the bonding yield is affected by the presence of particles. An average bonding yield of 55% is obtained. This is sufficient to build prototype circuit. In the futur, This bonding technique has the potential for large-scale production if the bonding yield and reliability can be improved by developing a machine-based process, thus avoiding particles.

Chapter 4

Integrated optical isolators based on nonreciprocal polarization conversion

In chapter 2, an integrated optical isolator based on NRPC (nonreciprocal polarization conversion) is introduced. The key component of the isolator is a nonreciprocal polarization converter, in which the polarization plane of the light rotates 45° upon propagation in one direction and -45° when propagating in the opposite direction. This device exploits the longitudinal MOKE (magneto-optic Kerr effect) effect by applying a magnetic field parallel to the surface of the MO (magneto-optic) film and to the incidence plane of the light. A major problem of this design is the linear birefringence of light in the waveguide. This device requires strict control of the design parameters to reduce the birefringence.

In this chapter, an integrated optical isolator based on NRPC is developed. This isolator consists of two TE-pass polarizers and a nonreciprocal polarization converter. The nonreciprocal polarization converter is based on NRPS (nonreciprocal phase shift), aiming to achieve full TE to TM conversion in one direction and zero conversion in the opposite direction. Compared to devices exploiting the longitudinal MOKE effect, this device does not need to meet the phase match condition. In principle, it has more fabrication tolerance and larger operation bandwidth.

4.1 An integrated optical isolator concept

An integrated isolator concept is proposed, as illustrated in Fig 4.1. It consists of two TE-pass polarizers and a nonreciprocal polarization converter. Unlike the nonreciprocal polarization converter described in section 2.2, this component is based on the NRPS effect. Full TE to TM conversion in one propagation direction and zero polarization conversion in the other propagation direction can be achieve by cascading a NRPS based structure with two PCs (polarization converters).

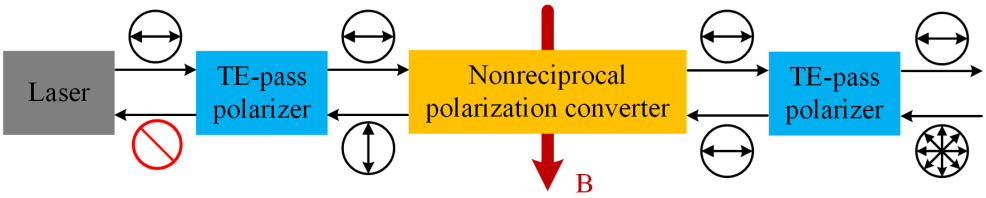

Figure 4.1: Schematic of an integrated optical isolator.

When the TE mode light is emitted from a laser source, it can pass through the TE-pass polarizer. Then, after propagating in the nonreciprocal polarization converter, the polarization state of the TE mode is unaltered when a transverse magnetic field is applied. The output is still TE mode light after the second TE-pass polarizer. In another propagation direction, light with unknown polarization states is filtered by the TE-pass polarizer and only TE mode light can pass through. After propagating in the nonreciprocal polarization converter, the TE mode light is converted to TM mode. Then, it is absorbed or scattered in the second TE-pass polarizer. Therefore, the laser source is protected from unwanted reflections.

4.2 Nonreciprocal polarization converter

4.2.1 Device design

The proposed nonreciprocal polarization converter is shown in Fig 4.2. It is used as a core of the proposed integrated isolator. It consists of two triangular waveguide sections and a rectangular waveguide section coated with a Ce:YIG layer. The two triangular waveguide sections are used as partial PCs. The external magnetic field is applied transverse to the propagation direction.

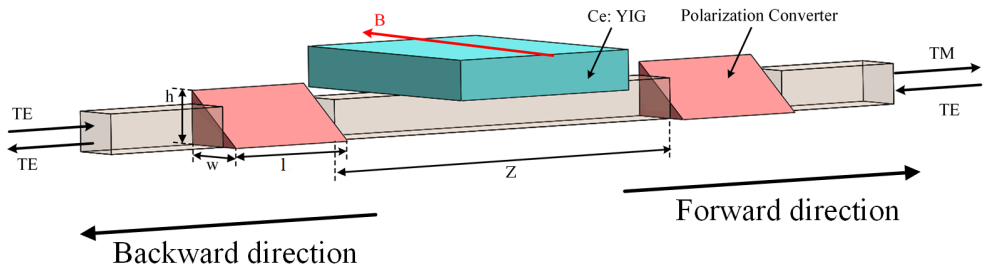

Figure 4.2: Schematic of the nonreciprocal polarization converter.

The cross section of the PC in the InP membrane is shown in Fig 4.3(a). The optimized height is found to be 460 nm, including a 300 nm InP layer, a 20 nm InGaAs layer and another 140 nm InP layer. The InGaAs layer is used as an etch-stop layer. Thus, the InGaAs layer and the extra InP layer can be selectively removed from

the IMOS waveguides. The slanted wall of the triangular waveguide can be obtained by wet etching InP in a $HCl : H_3PO_4$ solution.

A new set of eigenmodes are excited in the triangular section when TE or TM mode from the straight waveguide is coupled to the triangular waveguide. After propagating over a certain length, the two modes will recombine to a different polarization state. As shown in Fig 4.3(b), the new set of eigenmodes M1 and M2 is not aligned with the TE/TM polarizations of normal rectangular waveguides.

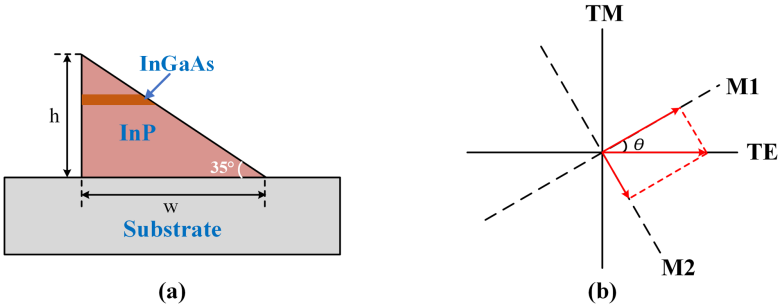

Figure 4.3: (a) Cross section of a triangular section. (b) Coordinate transformation to new bases.

As the eigenmodes propagate at different phase velocities, a phase-shift $\Delta\phi$ will be created after the propagation length l.

$$\Delta\phi = \left|\beta_1 - \beta_2\right| \cdot l \tag{4.1}$$

where β_1 and β_2 are the propagation constants of two eigenmodes M1 and M2.

If the input is TE mode, both TE and TM modes with equal amplitude can be obtained after a certain propagation length in the triangular waveguide. This also happens when the input is TM mode.

For the rectangular waveguide bonded with Ce:YIG on top, the NRPS effect will be enabled when the magnetic field is applied transverse to the propagation direction. This means NRPS will be induced between forward and backward traveling waves. However, because the Ce:YIG coated waveguide is symmetric in the horizontal direction, the TE mode will not be affected by the NRPS perturbation.

The phase difference induced by the NRPS effect can be written as

$$\Delta\phi_{\mathrm{NRPS}} = \left|\beta_{\mathrm{TM,F}} - \beta_{\mathrm{TM,B}}\right| \cdot z \tag{4.2}$$

where $\beta_{\mathrm{TM,F}}$ and $\beta_{\mathrm{TM,B}}$ are the propagation constants of the TM mode in forward and backward directions, respectively, z is the length of Ce:YIG coated waveguide section.

For the forward direction, the total phase shift in the rectangular waveguide with Ce:YIG layer can be written as

$$\Delta\phi_{\mathrm{F}} = \left|\beta_{\mathrm{TE}} - \beta_{\mathrm{TM,F}}\right| \cdot z \tag{4.3}$$

For the backward direction, the total phase shift in the rectangular waveguide with Ce:YIG layer can be written as

$$\Delta\phi_B = \left|\beta_{TE} - \beta_{TM,B}\right| \cdot z \tag{4.4}$$

In one direction, no matter whether the input is in the TE or TM mode, equal amplitude of both modes can be obtained by tuning the length of the PC. Then, a phase shift will be induced when propagating in the Ce:YIG coated waveguide section. The amount of phase shift is related to the length of the Ce:YIG coated waveguide section, according to equation 4.3. With the correct phase shift, full polarization conversion can be obtained after passing the second PC. In the other direction, zero polarization conversion can be realized because of the NRPS effect.

The working principle of this device can also be explained using Jones matrices. The transfer matrix of the first PC can be written as:

$$T_{PC,1} = \begin{bmatrix} \sqrt{1-\eta} & j\sqrt{\eta} \\ j\sqrt{\eta} & \sqrt{1-\eta} \end{bmatrix} \tag{4.5}$$

where η is the polarization conversion efficiency (PCE) of the PC. In this design, it is assumed the PCE is 50%. Thus, the transfer matrix can be expressed as:

$$T_{PC,1} = \begin{bmatrix} \frac{\sqrt{2}}{2} & j\frac{\sqrt{2}}{2} \\ j\frac{\sqrt{2}}{2} & \frac{\sqrt{2}}{2} \end{bmatrix} \tag{4.6}$$

For the waveguide section without the Ce:YIG layer, the transfer matrix can be written as:

$$T_{WG} = \begin{bmatrix} e^{j\beta_{TE}\cdot z_1} & 0 \\ 0 & e^{j\beta_{TM}\cdot z_1} \end{bmatrix} \tag{4.7}$$

where z_1 is the length of the waveguide section without the Ce:YIG layer. β_{TE} and β_{TM} are the propagation constants of the TE and TM modes in the waveguide section without the Ce:YIG layer, respectively.

The transfer matrix of the waveguide coated with the Ce:YIG layer in the forward direction can be written as:

$$T_{YIG,F} = \begin{bmatrix} e^{j\beta_{TE,F}\cdot z_2} & 0 \\ 0 & e^{j\beta_{TM,F}\cdot z_2} \end{bmatrix} \tag{4.8}$$

where z_2 is the length of the waveguide section with the Ce:YIG layer. β_{TE2} and $\beta_{TM,F}$ are the propagation constants of the TE and TM modes in the waveguide section with the Ce:YIG layer, respectively.

The transfer matrix of the waveguide coated with the Ce:YIG layer in the backward direction can be written as:

$$T_{\mathrm{YIG,B}} = \begin{bmatrix} e^{j\beta_{\mathrm{TE,B}}\cdot z_2} & 0 \\ 0 & e^{j\beta_{\mathrm{TM,B}}\cdot z_2} \end{bmatrix} \tag{4.9}$$

where $\beta_{\mathrm{TM,B}}$ is the propagation constant of the TM mode in the backward direction.

In this design, the second PC has the same length as the first PC. The transfer matrix can also be expressed as:

$$T_{\mathrm{PC},2} = \begin{bmatrix} \frac{\sqrt{2}}{2} & j\frac{\sqrt{2}}{2} \\ j\frac{\sqrt{2}}{2} & \frac{\sqrt{2}}{2} \end{bmatrix} \tag{4.10}$$

If the input is in the TE mode, the complete transfer in the two different propagating directions can be written as:

$$S_{\mathrm{out,F}} = T_{\mathrm{PC},2}\cdot T_{\mathrm{YIG,F}}\cdot T_{\mathrm{WG}}\cdot T_{\mathrm{PC},1}\cdot S_{\mathrm{TE}} \tag{4.11}$$

$$S_{\mathrm{out,B}} = T_{\mathrm{PC},2}\cdot T_{\mathrm{YIG,B}}\cdot T_{\mathrm{WG}}\cdot T_{\mathrm{PC},1}\cdot S_{\mathrm{TE}} \tag{4.12}$$

The output vector in the forward direction can be written as:

$$S_{\mathrm{out,F}} = \begin{bmatrix} \frac{1}{2}e^{j(\beta_{\mathrm{TE}}\cdot z_1+\beta_{\mathrm{TE,F}}\cdot z_2)} - \frac{1}{2}e^{j(\beta_{\mathrm{TM}}\cdot z_1+\beta_{\mathrm{TM,F}}\cdot z_2)} \\ \frac{1}{2}je^{j(\beta_{\mathrm{TE}}\cdot z_1+\beta_{\mathrm{TE,F}}\cdot z_2)} + \frac{1}{2}je^{j(\beta_{\mathrm{TM}}\cdot z_1+\beta_{\mathrm{TM,F}}\cdot z_2)} \end{bmatrix} \tag{4.13}$$

It can be obtained that the polarization state from the output is tuned by the phase shift from the waveguide between the two PCs. If $(\beta_{TE}\cdot z_1+\beta_{TE,F}\cdot z_2)$ and $(\beta_{TM}\cdot z_1+\beta_{TM,F}\cdot z_2)$ equal to π, the output vector is:

$$S_{\mathrm{out,F}} = \begin{bmatrix} 0 \\ 1 \end{bmatrix} \tag{4.14}$$

Hence, in the forward direction, the input TE mode is converted to the TM mode in the output.

In the backward direction, the output vector can be written as:

$$S_{\mathrm{out,B}} = \begin{bmatrix} \frac{1}{2}e^{j(\beta_{\mathrm{TE}}\cdot z_1+\beta_{\mathrm{TE,B}}\cdot z_2)} - \frac{1}{2}e^{j(\beta_{\mathrm{TM}}\cdot z_1+\beta_{\mathrm{TM,B}}\cdot z_2)} \\ \frac{1}{2}je^{j(\beta_{\mathrm{TE}}\cdot z_1+\beta_{\mathrm{TE,B}}\cdot z_2)} + \frac{1}{2}je^{j(\beta_{\mathrm{TM}}\cdot z_1+\beta_{\mathrm{TM,B}}\cdot z_2)} \end{bmatrix} \tag{4.15}$$

As analyzed in Chapter 2, $\beta_{\mathrm{TE,F}} = \beta_{\mathrm{TE,B}}$ since the TE mode will not experience NRPS. If $(\beta_{\mathrm{TE}}\cdot z_1+\beta_{\mathrm{TE,B}})$ is again π, and $(\beta_{\mathrm{TM}}\cdot z_1+\beta_{\mathrm{TM,B}}\cdot z_2)$ becomes 0, the output vector is:

$$S_{\mathrm{out,B}} = \begin{bmatrix} 1 \\ 0 \end{bmatrix} \tag{4.16}$$

In the backward direction, the input TE mode remains TE in the output. It can be obtained that the key to realize a nonreciprocal polarization converter is optimizing the MO interaction so that $(\beta_{\mathrm{TM,F}}-\beta_{\mathrm{TM,B}})\cdot z_2$ equals to π.

4.2.2 Optimization of the device performance

This design is simulated with a FDTD solver. As discussed in the previous section, to realize a nonreciprocal polarization converter, the length of the PC needs to be optimized to reach exactly 50% polarization conversion efficiency. As shown in Fig 4.4, the normalized TE and TM output power is simulated as a function of the triangular section length for a TE mode input light.

From the simulation results, it can be seen that one triangular section can be used to achieve 50% conversion, but not enough to achieve full conversion. This is because the mode tilt is not exactly 45° in the triangular waveguide section. TE and TM modes with equal amplitude can be obtained for a triangular section with a minimum length of 1.2 μm.

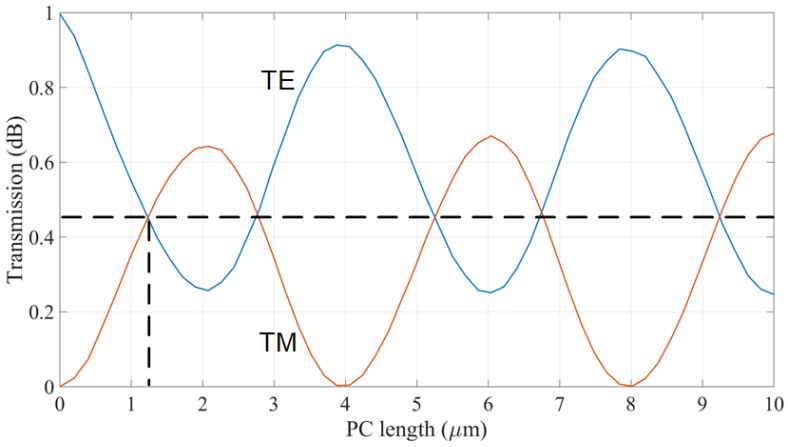

Figure 4.4: Transmission as a function of the length of the triangular waveguide section.

Next, to proof the concept of this device in the FDTD solver, the length of Ce:YIG coated waveguide section is swept from 0 to 12 μm, in steps of 0.2 μm, using the PCs with the optimized lengths. In simulation, the NRPS coefficient is deliberately enhanced by a factor of 100 to reduce the simulation length, because FDTD simulation is memory-consuming. In theory, the NRPS effect is a linear MO effect. Increasing the coefficient 100 times means the length of a real device will be 100 times larger than the length in our simulation. The bonding layer between the Ce:YIG film and the waveguide is also ignored to reduce the simulation time.

The simulation results for an input of TE-polarized light at 1550 nm are shown in Fig 4.5. The vertical axis is the transmission in the proposed device, as illustrated in Fig 4.5. The horizontal axis is the length of Ce:YIG coated waveguide section from 0 to 1.2 mm. Fig 4.5(a) and Fig 4.5(b) show the transmission of TE mode (red curve) and TM mode (blue curve) for forward and backward propagating directions.

It can be seen that polarization conversion between TE and TM is periodically repeated as the length of Ce:YIG coated waveguide section changes, and the periods for the forward and backward directions are different, because of the NRPS effect, as seen from Eq. 4.12 and Eq. 4.13. To realize NRPC, we need to find the optimal

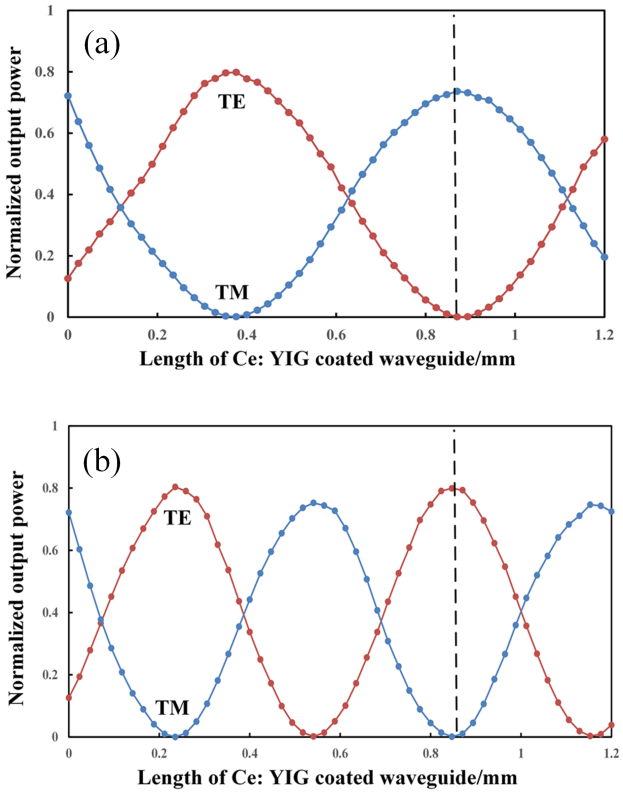

Figure 4.5: Transmission as a function of the length of Ce:YIG coated waveguide section, for a TE polarized input signal. (a) In forward direction. (b) In backward direction.

length of the Ce:YIG coated waveguide section for which the TM mode has maximum output power in the forward direction and minimum output power in the backward direction.

In Fig 4.5(a), the dashed line shows a maximum polarization extinction ratio (PER) 28.2 dB in forward direction at 1550 nm, when the length of Ce:YIG coated waveguide section is 0.85 mm. In Fig 4.5(b), the obtained PER in backward direction is -19.0 dB when the length of Ce:YIG coated waveguide section is also 0.85 mm.

The same results can also be obtained for a TM polarized input signal. The optical loss of 1.4 dB is found. It mainly originates from the interfaces between PCs, waveguides and the Ce:YIG layer. TM mode experiences more optical loss than the TE mode at the interfaces.

The electrical field propagating along the InP waveguide in the y and z directions for two different propagation directions are shown in Fig 4.6 when the length of Ce:YIG coated waveguide section is optimized. For the forward direction, the input TE mode is partly converted to the TM mode after the first PC. Then, the hybrid mode experiences a phase shift in the waveguide section coated with the Ce:YIG layer. After the second PC, the hybrid mode is fully converted to the TM mode. For the backward

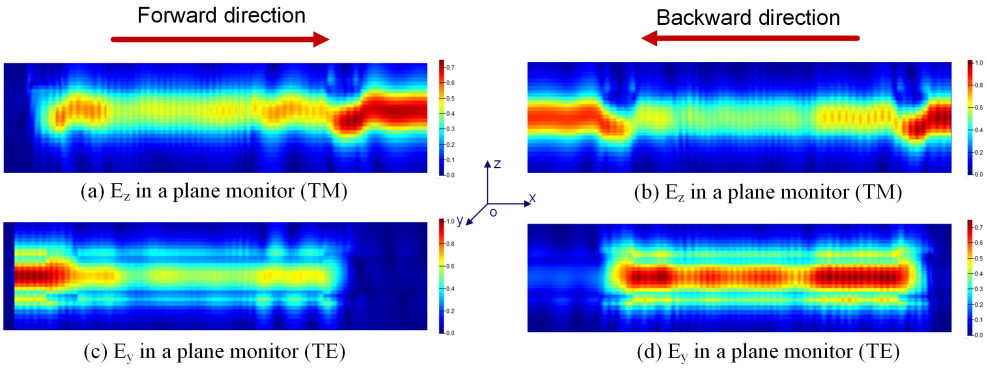

(a) E_z in a plane monitor (TM) (b) E_z in a plane monitor (TM)

(c) E_y in a plane monitor (TE) (d) E_y in a plane monitor (TE)

Figure 4.6: Electrical field in the y and z directions propagating in the InP waveguide for two different propagation directions. (a) E_z in forward direction. (b) E_z in backward direction. (c) E_y in forward direction. (b) E_y in backward direction.

direction, due to the presence of NRPS, the input TM mode remains as the TM mode at the output.

The simulation results show that the device has a high polarization conversion efficiency and acceptable insertion loss. A significant advantage of this device is its availability for both TE and TM modes. It is possible to use the device in an integrated optical isolator by integrating polarizers on both sides.

4.2.3 Fabrication process

The nonreciprocal polarization converter is fabricated in the IMOS platform. The main steps of the process flow are shown in Fig 4.7.

(1) The typical layer-stack of a passive IMOS wafer contains a 300 nm InP layer on top of a 100 nm InGaAs etch-stop layer on InP the substrate. An additional 20 nm InGaAsP layer and a 140 nm InP layer are added for the PCs. A 50 nm SiN layer is deposited on the wafer as a hard-mask and a layer of positive electron-beam resist (ZEP 520A) is spin-coated on SiN.

(2) The areas for trenches are opened by an electron-beam lithography (EBL) step. A CHF_3 based reactive ion etching (RIE) step is performed to transfer the pattern to the SiN layer. Then, H_3PO_4:HCl (4:1) and H_2SO_4:H_2O_2:H_2O (1:1:10) are used, respectively, to remove 300 nm InP layer and 100 nm InGaAs layer from the opening areas. Initial slopes are formed in the top two layers because of the selective wet etch with etch stop layers.

(3) An EBL step is performed on a new layer of ZEP 520A, which is spin-coated on a new 50 nm SiN layer. The vertical sidewalls of the rectangular waveguides and the triangular waveguides are patterned in the same step. A CH_4/H_2 based RIE step is used to etch the InP layer.

(4) A 100 nm SiN layer is deposited, and another EBL step is performed to expose the areas where the slopes for PCs are to be completed, while protecting the rest of the wafer, including the dry-etched vertical sidewalls. The etch time of the CHF_3 based

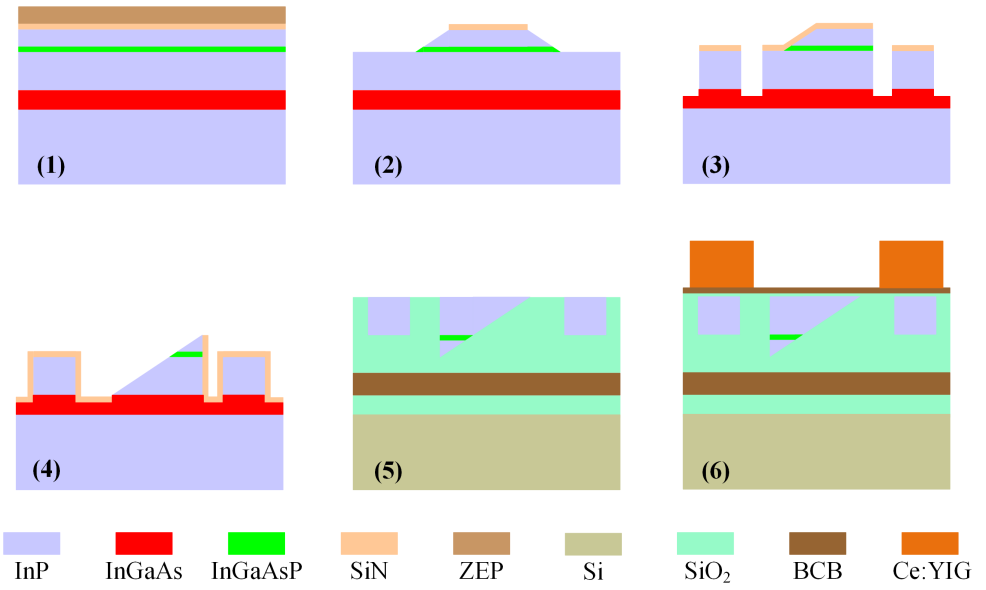

Figure 4.7: Main steps of the fabrication process.

RIE step is well-controlled so that the sidewall of the PC is covered with SiN. Then, the triangular sections are created using H_3PO_4:HCl (4:1) and H_2SO_4:H_2O_2:H_2O (1:1:10) to selectively wet etch the InP and InGaAsP layer.

(5) 400 nm SiO_2 layers are deposited on the IMOS wafer and a Si wafer. A layer of BCB (Cyclotene 3022-46) is spin-coated on the IMOS wafer. Then, the IMOS wafer is bonded up-side down onto the Si wafer in a bonder. The InP substrate and the InGaAs etch stop layer are removed in H_3PO_4:HCl (4:1) and H_2SO_4:H_2O_2:H_2O (1:1:10), respectively.

(6) A 50 nm SiO_2 is deposited on the processed IMOS wafer. A layer of diluted BCB (Cyclotene 3022-46: Mesitylene 1:5 v/v) is spin-coated at 4000 rpm for 30 seconds on the SiO_2 layer. The Ce:YIG dies are cleaned using acetone and IPA. They are aligned and attached on top of the IMOS waveguides. Finally, the dies are bonded on the IMOS wafer in the bonder following the bonding recipe developed in chapter 3.

The designed mask is shown in Fig 4.8(a). The four square markers are designed to align the four corners of the Ce:YIG die. The length of the rectangular waveguide in between the two PCs is 5.2 mm, to ensure enough space for the Ce:YIG die placement during the Ce:YIG-die-to-IMOS-wafer bonding process.

Fig 4.8(b) is the microscope image of the fabricated mask. It can be seen that a 4×4 mm^2 Ce:YIG die is adhesively bonded to the InP waveguide. The length of the waveguide without the Ce:YIG cladding is 1.2 mm. When the Ce:YIG film is saturated, the NRPS is expected to be π for different propagation directions according to the simulation results in section 3.2. The corners of the die deviate from the markers. This is because the die is manually aligned and it might move during wafer handling

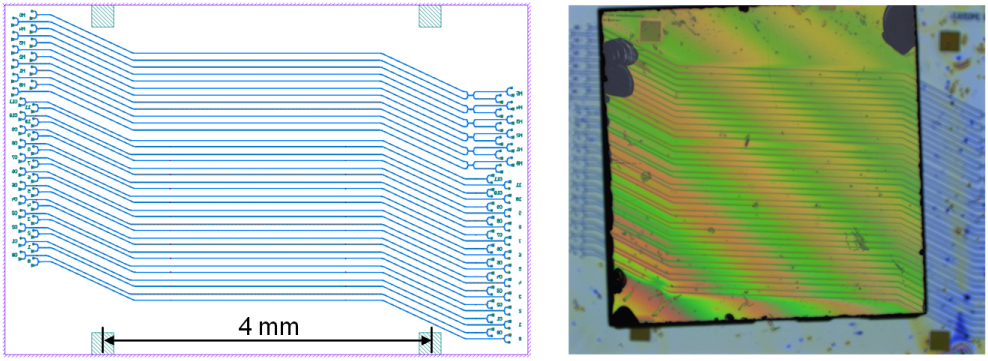

Figure 4.8: (a) The designed mask. (b) Microscope image of the fabricated devices bonded with a Ce:YIG die.

and transferring. This misalignment does not affect the measurement since all the grating couplers are outside of the bonding area.

4.2.4 Characterization

A schematic of the characterization structure is given in Fig 4.9. TE and TM grating couplers are placed on both sides of the device to couple light between the device and the fibers. The grating couplers and the two PCs are connected with two 1×2 MMIs. An additional rectangular waveguide section (Δz) is added. This functions as a reciprocal phase shifter. The length of this section varies from 1 to 6 μm, in steps of 1 μm.

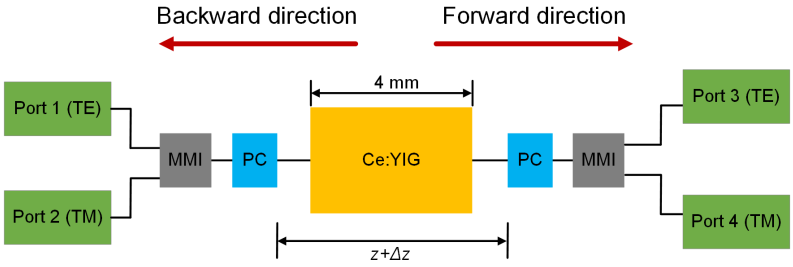

Figure 4.9: Schematic of a characterization structure of a nonreciprocal polarization converter.

A 4-port measurement method is used to characterize the nonreciprocal polarization converter. P_{ji} is the measured power at output j with i as input. The insertion losses, propagation losses and polarization sensitivity from all the components can be canceled out [98]. The transmission power for all ports for the forward direction can be expressed as

$$P_{13} = \alpha_1 \alpha_3 \alpha_{\mathrm{MMI}}^2 (1 - \eta_{\mathrm{forward}}) P_{\mathrm{in}} \tag{4.17}$$

$$P_{14} = \alpha_1 \alpha_4 \alpha_{\mathrm{MMI}}^2 \eta_{\mathrm{forward}} P_{\mathrm{in}} \tag{4.18}$$

$$P_{23} = \alpha_2 \alpha_3 \alpha_{\mathrm{MMI}}^2 \eta_{\mathrm{forward}} P_{\mathrm{in}} \tag{4.19}$$

$$P_{24} = \alpha_2 \alpha_4 \alpha_{\mathrm{MMI}}^2 (1 - \eta_{\mathrm{forward}}) P_{\mathrm{in}} \tag{4.20}$$

The PCE η for the forward direction can be expressed as

$$\eta_{\mathrm{forward}} = \frac{1}{1 + \sqrt{\frac{P_{13} P_{24}}{P_{14} P_{23}}}} \tag{4.21}$$

Similarly, the PCE η for the backward direction can be expressed as

$$\eta_{\mathrm{backward}} = \frac{1}{1 + \sqrt{\frac{P_{31} P_{42}}{P_{41} P_{32}}}} \tag{4.22}$$

A schematic of the measurement setup is given in Fig 4.10. The grating couplers are designed to couple light into or out of the device to the fibers. The two single mode fibers are aligned to the gratings at an angle of 10° with respect to the surface normal. TE (TM) light can be injected and collected by TE (TM) grating couplers. The various transmission spectra of the device are measured using a tunable laser and a power meter. A polarization controller is placed in the input fiber to manipulate the polarization states. The transmission spectra are recorded from the grating couplers for the forward and backward propagation direction in order to characterize the nonreciprocity of the device.

A Nd-Fe-B magnet is attached on top of the SGGG substrate to create a transverse magnetic field on the Ce:YIG film. The magnetic field at the Ce:YIG film is over 50 Oe (measured with a Gaussmeter). This is strong enough to saturate the Ce:YIG film.

Fig 4.11 shows the measured PCE as a function of the wavelength when Δz is 2 μm. The blue and orange sinusoidal curves are the PCE for forward and backward propagation directions, respectively. The ripples on the spectra curves might originate from a time instability such as vibration, mechanical movement, and acoustic signals, which would be temporal and coupled via fiber movements.

The vertical dashed line shows that a maximum PCE of 98.7% is achieved at a wavelength of 1518 nm. The nonreciprocal PCE at this wavelength is 9.8% between the two different propagation directions. The wavelength shift between the two sinusoidal curves is 0.2 nm. This shift corresponds to a NRPS of 0.06 rad/mm. In

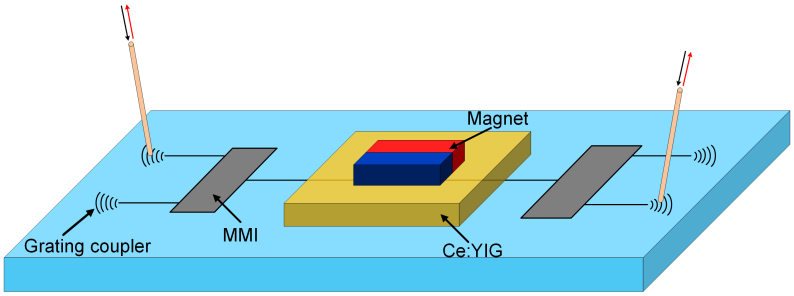

Figure 4.10: Schematic of the characterization setup.

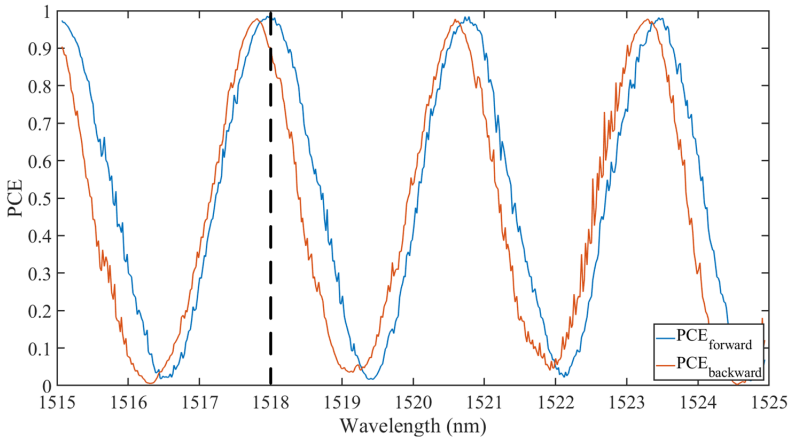

Figure 4.11: The measured PCE in two propagation directions as a function of the wavelength.

simulation, this NRPS value indicates that the distance between the Ce:YIG and the InP waveguide would be about 400 nm.

Ideally, the thickness of the bonding layer should be 120 nm, corresponding to a NRPS of 0.8 rad/mm in simulation. However, in the Ce:YIG-die-to-IMOS-wafer bonding process, particles may drop on the wafer surface at any step, especially during the manual placement of the Ce:YIG dies on the InP membrane. These particles cause local delaminations and increase the distance between the Ce:YIG die and the InP waveguide. The presence of the particles causes a weak bonding, which means the adhesion of the Ce:YIG die to the InP membrane is not strong enough.

A preliminary tensile test is carried out after the characterization. The Ce:YIG die came off the wafer when pushing it with tweezers. One inspection is that there are different sizes of particles locating in the bonding layer. The measured sizes of these particles are in a range of 20 nm to 600 nm using a step-height measurement tool. The possible large sizes of the particles could explain the measured small NRPS.

The measured fiber-to-fiber transmission spectra, for both TE and TM modes input, are shown in Fig 4.12. The blue and orange curves are the transmission spectra for forward and backward propagation directions, respectively. The vertical dashed

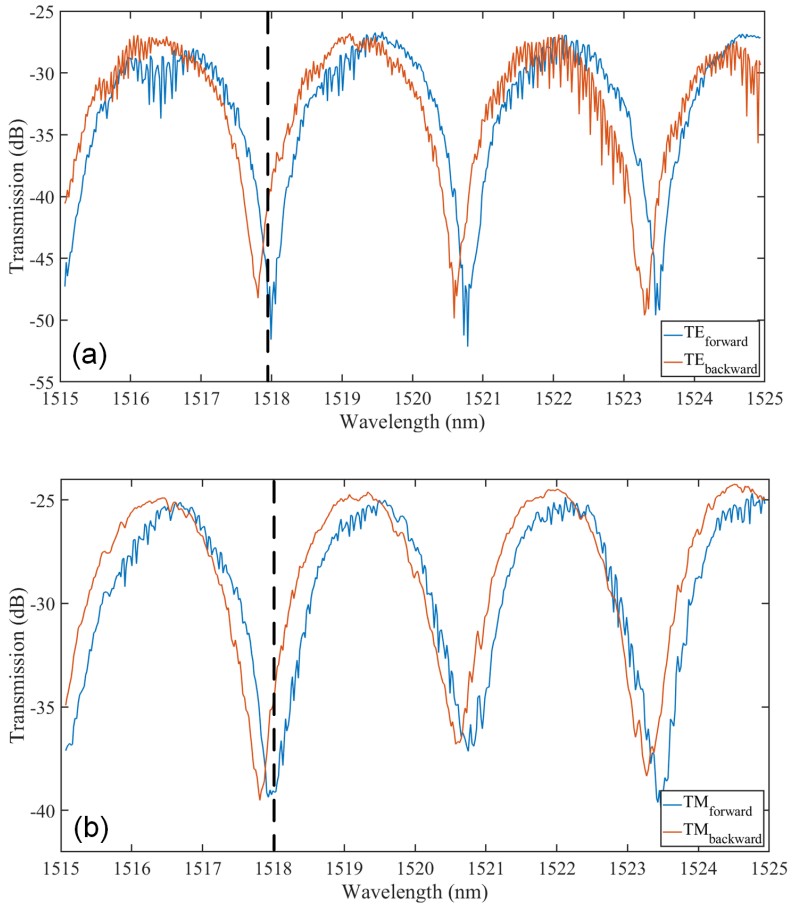

Figure 4.12: (a)Transmission spectra between port 1 and port 3 for the TE mode. (b) Transmission spectra between port 1 and port 3 for the TM mode.

line in Fig 4.12(a) indicates that, for the TE mode input, a nonreciprocal transmission difference of 12.6 dB is obtained at a wavelength of 1518 nm. For the TM mode input, the nonreciprocal transmission difference is 5.4 dB, as shown in Fig 4.12(b).

The difference in nonreciprocal transmission for the TE and TM modes may be because that the PCE of the triangular section is not exactly 50%. This means for different input modes, the NRPS and absorption loss from the Ce:YIG are different. Therefore, the nonreciprocal transmission for TE and TM input modes are different.

The insertion loss of the device is about 28 dB for the TE mode input. This can be attributed to several aspects: 1) the fibre-to-waveguide coupling loss is measured to be 13.8 dB. 2) the two triangular waveguide sections contribute around 1 dB loss. 3) the 1×2 MMI coupler at the output port gives a 3 dB loss. 4) The rest of the insertion loss is attributed to the waveguide propagation loss and the scattering loss in the waveguide section covered with the Ce:YIG die. The insertion loss for the TM

mode is about 3 dB less than the insertion loss for the TE mode. This is because the fiber-to-waveguide coupling loss and the propagation loss for the TE and TM modes are different, and the PCE of the PC is not exactly 50%.

The measured free spectral range (FSR) is 2.8 nm for both TE and TM modes. The FSR can be calculated using the following equation:

$$\Delta\lambda = \frac{\lambda^2}{\Delta n \cdot (z + \Delta z)} = \frac{\lambda^2}{\Delta n_1 \cdot \Delta z + \Delta n_1 \cdot z_1 + \Delta n_2 \cdot z_2} \tag{4.23}$$

where $\Delta n_1 = 0.22$ is the difference between the effective refractive indices of the TE and TM modes in the waveguide section without Ce:YIG. $z_1 = 1.2$ mm is the length of the waveguide section without Ce:YIG. $\Delta z = 2$ μm is the length of the reciprocal phase shifter. $\Delta n_2 = 0.16$ is the difference between the effective refractive indices of the TE and TM modes in the waveguide section with Ce:YIG. $z_2 = 4$ mm is the length of the waveguide section with Ce:YIG. The calculated $\Delta\lambda$ is 2.6 nm, which is comparable to the measured FSR.

In order to tune the beat length of the two hybrid modes, an additional rectangular waveguide section (Δz) is added and its length is swept from 1 μm to 6 μm. The scatter points in Fig 4.13 shows PCE for the devices with different Δz at a wavelength of 1518 nm. The PCE of the device with $\Delta z = 5$ μm is not available because of high insertion loss (over 60 dB), which may be caused by the fracture in the InP waveguides. Fractures in the InP waveguides sometimes occur during the Ce:YIG-die-to-IMOS-wafer bonding process, as shown in Fig 3.18.

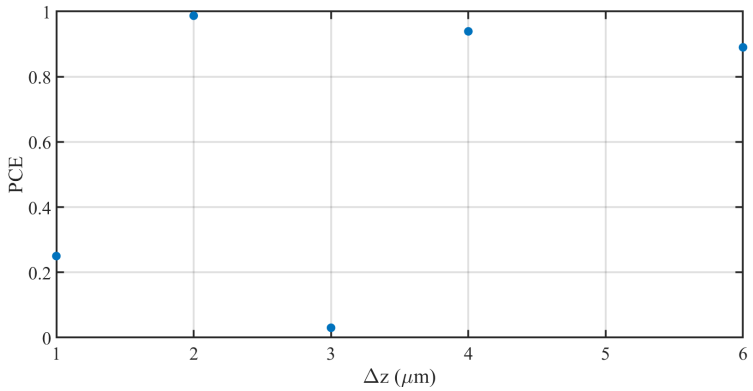

Figure 4.13: PCE for the devices with Δz from 1 μm to 6 μm at a wavelength of 1518 nm.

In principle, a phase shift is created between the two eigenmodes propagating in the rectangular waveguide section. The PCE oscillates with a period of L_π, which can be expressed as:

$$L_\pi = \frac{\pi}{\beta_{\mathrm{TE}} - \beta_{\mathrm{TM}}} \tag{4.24}$$

The calculated L_π is 3.5 μm in this design. In the measurement, the highest PCE is 98.7% when Δz is 2 μm and the lowest PCE is 3.0% when Δz is 3 μm. From Fig 4.13, the measured L_π is 1 μm. This might be because the deviation of the waveguide dimension or the stress induced in the InP-membrane-on-Si bonding procss.

As plotted in Fig 4.14, the nonreciprocal PCE (ΔPCE) varies between 0.8% and 9.8% for devices with Δz from 1 to 6 μm, at a wavelength of 1518 nm. This variation is related to the change of reciprocal phase shift, as discussed in section 4.2.1.

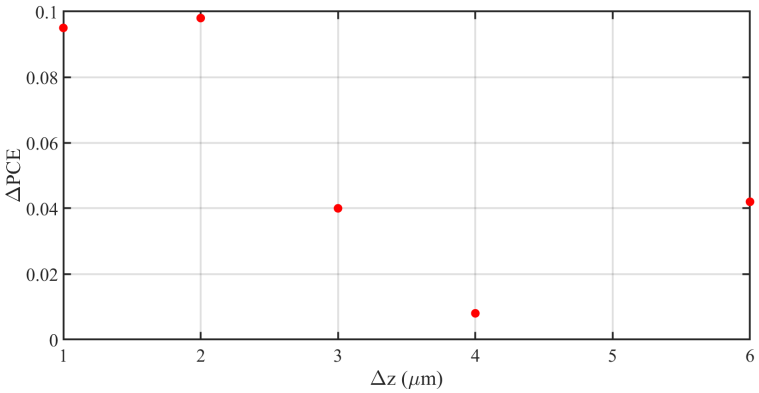

Figure 4.14: Nonreciprocal PCEs for devices with Δz from 1 to 6 μm.

4.3 Integrated TE-pass polarizers

To achieve optical isolation on chip, two integrated TE-pass polarizers are needed on both sides of the nonreciprocal polarization converter in order to extinguish the unwanted TM mode light.

4.3.1 Introduction

The operation principles of the integrated polarizers can be classified into two types: mode attenuation and mode cut-off [99]. The origin of the mode attenuation is from the optical absorption in the metal cladding on the waveguide. This attenuation is polarization dependent because of the different mode distribution of the two modes. Mode cut-off can be achieved by varying the dimension of the waveguide. One polarization mode will be radiated away when the cut-off condition is met. Integrated polarizers based on mode attenuation normally have a large footprint (1 mm long) to fully attenuate one unwanted polarization state. For example, a ridge waveguide with a shallow-etched ridge waveguide has been demonstrated in 2010 [100]. An extinction ratio of 25 dB was measured over a 100 nm wavelength range for a 1mm-long polarizer. The device footprint can be dramatically shortened by using hybrid plasmonic waveguide (HPWG) (hybrid plasmonic waveguide) structures. A HPWG based device, with 30 μm in length, have shown more than 28 dB extinction ratio over 150

nm bandwidth and less than 0.04 dB for the TE mode on the SOI platform [101]. Compared with devices based on mode attenuation, the mode cut-off based devices have smaller footprint (1 μm in length), but have less extinction ratio. A horizontal nanoplasmonics slot waveguide has been demonstrated in 2013 [102]. The coupling region length of the device is only 1 μm. More than 16dB polarization extinction ratio was obtained with 80 nm bandwidth, with an insertion loss of 2.2dB.

Considering the device performance and the compatibility with the IMOS platform, in this section, two different TE-pass polarizer designs utilizing mode attenuation are proposed and simulated. The goal is to achieve a TE-pass polarizer with small foot print (< 30 μm), large bandwidth (> 100nm wavelength range), high PER (polarization extinction ratio) (>30 dB), low insertion loss (<1 dB).

4.3.2 Device design and simulation

- Directional coupler based polarizer

  A three-dimensional schematic of the proposed TE-pass polarizer is shown in Fig 4.15(a). The basic structure is a directional coupler with three waveguides. Two metal strips are placed directly on the two other branches.

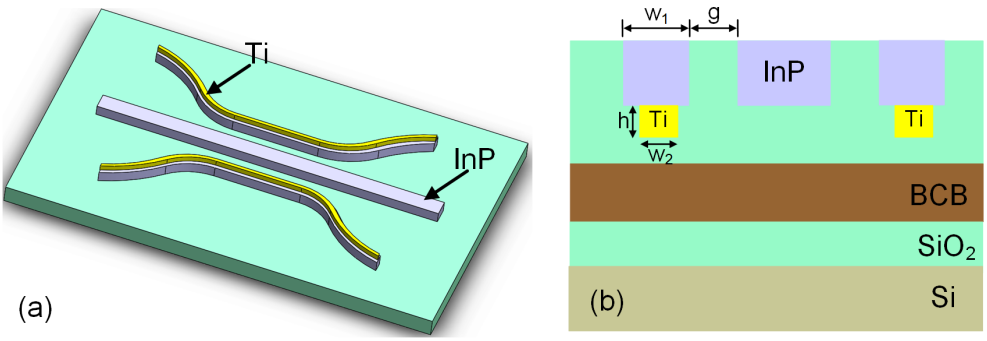

Figure 4.15: (a)Three-dimension schematic of the TE-pass polarizer. (b) Cross-section of the TE-pass polarizer.

By optimizing the device dimensions, the TM mode can be coupled into the two branches and be absorbed by the metal strips while the TE mode is not coupled and propagates in the central waveguide. Titanium (Ti) is chosen as the metal because of its good adhesion to InP, and it behaves as a high-loss dielectric material on the waveguide.

The cross-section of the device is shown in Fig 4.15(b). The central waveguide is 300 nm in height and 400 nm in width. The two other branches are symmetrical and have a width of w_1. The height and width of the metal layer are h and w_2, respectively. The gap between the central waveguide and another branch is g.

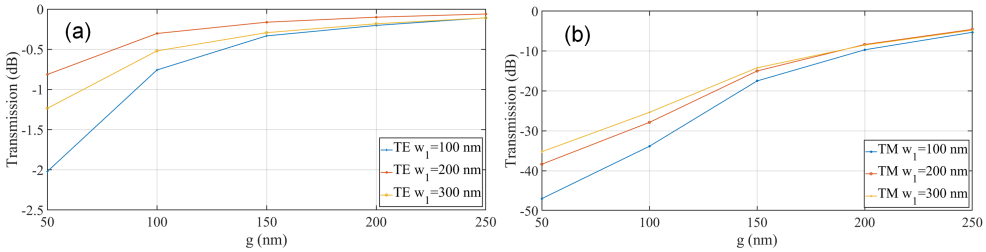

Figure 4.16: (a)Transmission of the TE mode as a function of g and w_1. (b) Transmission of the TM mode as a function of g and w_1.

The device is simulated with a FDTD solver. The length of the coupling region is first set at 10 μm. The metal strip is 100 nm in width and 100 nm in height, taking into account the limitations of the fabrication process. The gap between the central waveguide and the two other branches is swept from 50 nm to 250 nm.

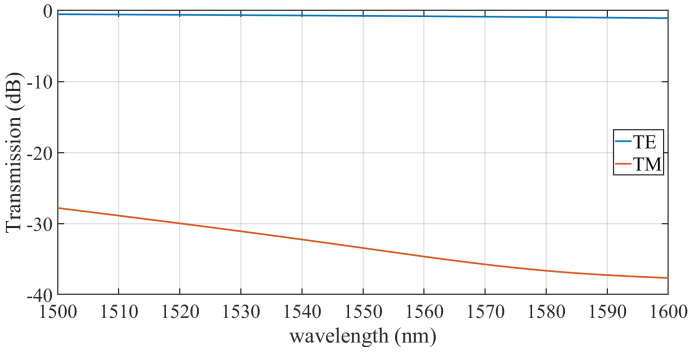

Figure 4.17: Transmission of the two modes as a function of the wavelength.

Fig 4.16(a) and Fig 4.16(b) show the transmission of the two input modes at a wavelength of 1550 nm, respectively. The transmission of the TE mode varies from -2.0 dB to 0.2 dB while the transmission of the TM mode varies from -48 dB to -5 dB as the gap increases. It can be seen that the TM mode is more sensitive to the distance of the gap than the TE mode. The highest polarization extinction ratio of 46 dB is obtained when g is 50 nm. It can also be noticed that there is a trade-off between insertion loss and PER. The insertion loss for the TE mode is 2 dB when g is 50 nm. A PER of 34 dB and an insertion loss of 0.8 dB can be obtained when g is 100 nm and w_1 is 100 nm.

The bandwidth of the device is also analyzed. Fig 4.17 shows the transmission for the TE and TM mode as a function of the wavelength from 1500 nm to 1600 nm when w_1 and w_2 are 100 nm. The insertion loss for the TE mode varies from 0.5 dB to 1.1 dB while the PER varies from 27 dB to 37 dB in this 100 nm wavelength range.

- HPWG based polarizer

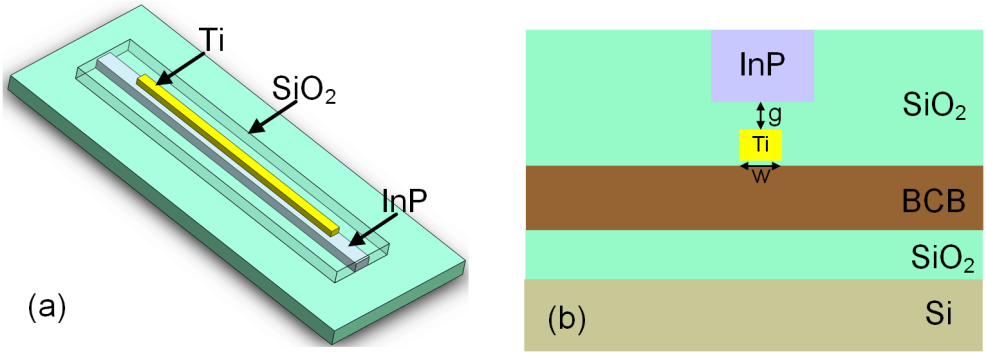

Figure 4.18: (a)Three-dimensional schematic of the TE-passe HPWG polarizer. (b) Cross-section of the TE-pass HPWG polarizer.

Fig 4.18 shows the schematic of the hybrid plasmonic waveguide based TE-pass polarizers. The HPWG section consists of a Ti layer, an InP layer and a SiO_2 layer. The TM mode is confined near the metal surface and be absorbed in the metal while the TE mode is mostly concentrated in the InP waveguide and has low propagation loss.

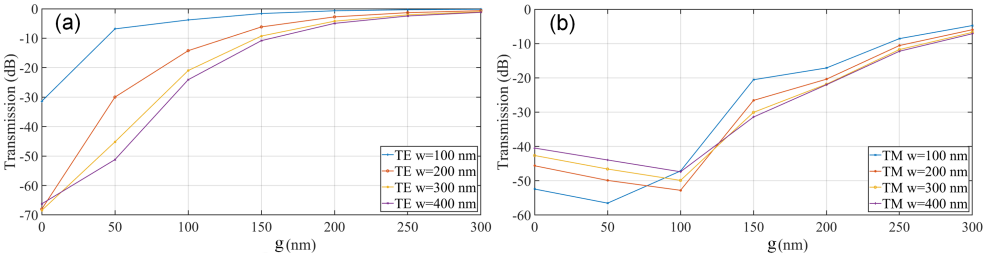

Figure 4.19: (a)Transmission of the TE mode as a function of g and w. (b) Transmission of the TM mode as a function of g and w.

The dimensions of the polarizer design are optimized with a FDTD solver. The length of the plasmonic region is 30 μm to ensure high PCE. The height of the Ti layer is 100 nm and the width w is swept from 100 nm to 400 nm. Fig 4.19 shows the transmission as a function of the distance between the InP waveguide and the Ti layer for the TE and TM modes input, at a wavelength of 1550 nm.

Narrower distance between the InP waveguide and the metal layer brings higher insertion loss for both TE and TM modes, because the modes are interacting more with the metal surface. The insertion loss for the TE mode also increases as the metal becomes wider. A PCE of 43.4 dB and an insert loss of 3.8 dB for the TE mode are obtained when w is 100 nm and g is 100 nm. This high insertion loss (compared with the first polarizer deisgn) is caused by the absorption in the Ti layer.

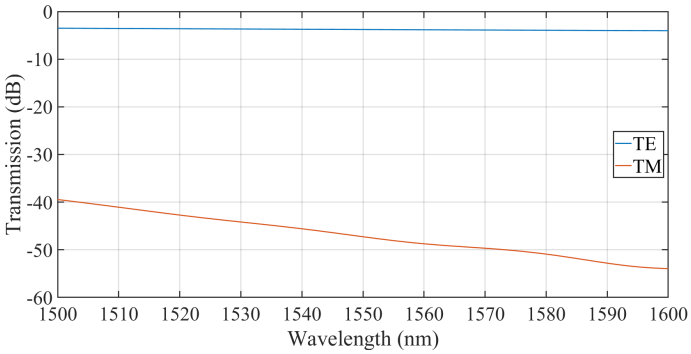

Figure 4.20: Transmission of the two modes as a function of wavelength.

Fig 4.20 shows the transmission for the TE and TM modes as a function of the wavelength from 1500 nm to 1600 nm when w and g are 100 nm. Over 34 dB PCE can be obtained in 100 nm wavelength range.

These two designs are both compatible with the IMOS platform. The metal strips can be realized with a metal lift-off process [103]. However, the second design requires an extra step of 100 nm SiO_2 deposition.

4.4 Summary

In this chapter, an integrated optical isolator, consisting of two TE-pass polarizers and a non-reciprocal polarization converter, is proposed.

The non-reciprocal polarization converter makes use of the NRPS effect and contains two asymmetric waveguide sections (triangular waveguide) as partial polarization converter and a rectangular waveguide section, on which a Ce:YIG layer is adhesively bonded. The working principle of the device is discussed using two different methods. In simulation, the maximum PER is 28.2 dB in forward direction and -19.0 dB in backward direction at a wavelength of 1550 nm.

The nonreciprocal polarization converter is fabricated in the IMOS platform. A 4 mm × 4 mm Ce:YIG die is adhesively bonded on the InP waveguide. A maximum nonreciprocal PCE of 9.8% and 12.6 dB nonreciprocal transmission for the TE mode are measured. The performance of this device can be improved by optimizing the bonding process.

Two different TE-pass polarizer designs are proposed and simulated. The devices show small footprint, large bandwidth, low insertion loss and high PER in simulation. The proposed polarizers are compatible with the IMOS platform and can be fabricated together with the nonreciprocal polarization converter. It is promising to integrate the proposed isolator with other passive and active devices in the IMOS platform and to provide a step forward towards a fully functional PIC.

Chapter 5

Integrated polarization-independent isolators and circulators

MZI-based isolators and circulators exploiting NRPS (nonreciprocal phase shift) effect have been developed in recent years [104]. However, due to the polarization dependence of the NRPS effect, these optical isolators and circulators only work for one polarization state. This is not enough to accommodate the isolation needs of polarization-diverse integrated optical systems.

In this chapter, an integrated non-reciprocal device is demonstrated by connecting PCs with a MZI structure and adhesive bonding of a Ce:YIG layer in the IMOS platform. This work is promising for removing the optical interfaces between laser and isolator for robust production. The designed device can be operated as a polarization-independent isolator or as a polarization-independent circulator [1].

5.1 Device design

The polarization independent isolator/circulator is a Mach-Zehnder interferometer and is schematically shown in Fig 5.1. Two 2×2 MMIs are placed on both sides of the device to form a 4-port circulator and also an isolator when considering the port pairs on opposite sides. The 2×2 MMIs are developed for low polarization dependence and low reflection on the IMOS platform. Four ultra-small (<5 μm length) and efficient (97.5% polarization conversion efficiency) PCs are involved [98]. A PC contains two triangular waveguides with one rectangular waveguide section in-between. A set of rotated eigenmodes will be excited when a TE or TM polarized mode is coupled to the triangular waveguide. After propagating over a certain length, the two modes

[1] The content of this chapter was previously published in a peer reviewed journal titled "Integrated polarization-independent optical isolators and circulators on an InP membrane on silicon platform," Optica 8, 1654-1661 (2021).

will recombine to a different polarization state. Two triangular sections are needed to achieve full TE-TM conversion.

A Ce:YIG die is adhesively bonded on top of two arms of the MZI structure with a layer of BCB. A NRPS effect will be present for the TM mode when an external lateral magnetic field is applied. The NRPS, defined as the phase shift between waves propagating in opposite directions, decreases with the thickness of the BCB layer. TE and TM modes have different propagation constants in the rectangular waveguide sections, which will introduce an additional reciprocal phase shift (RPS) to the propagation light in the two arms.

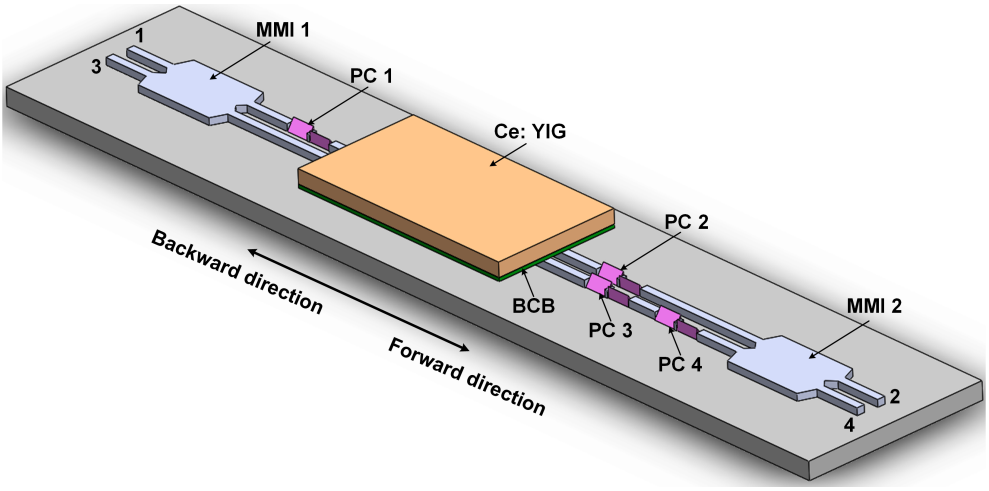

Figure 5.1: Schematic of the MZI-based nonreciprocal device in the IMOS platform.

For the forward direction, the input signal coupled into port 1 is split into two branches by MMI 1. The signals in both branches are designed to have equal power but a phase difference of $\pi/2$. When the input is TE mode, it will be converted to TM mode after passing through PC 1 in the upper branch. NRPS becomes effective on the TM-mode in the upper branch covered with Ce: YIG when a transverse magnetic field is applied. The TM mode will be converted back to TE mode after propagating through PC 2. In the lower branch, the TE mode will not be affected by the NRPS effect. The TE mode signal in the lower branch will be converted to the TM mode after PC 3 and back to the TE mode after PC 4. PC 3 and PC 4 are used to balance the losses from PC 1 and PC 2. The birefringence in the waveguides will cause an additional reciprocal phase shift (RPS) between the signals in the two branches.

Similarly, if the input is in the TM-mode, the same NRPS and RPS will be obtained, but now in the lower branch. Thus, both input polarizations will lead to equally large, but opposite, phase differences between the branches. If arranged properly, this device enables a polarization independent behavior.

5.2 Working principle

The schematic configuration is shown in Fig 5.2. L_1 is the length of the branch without Ce:YIG layer. L_2 is the length of thebranch with Ce:YIG layer. L_3 is the length of the branch between PC 3 and PC 4. In this design, L_3 is negligible compared with L_1 and L_2.

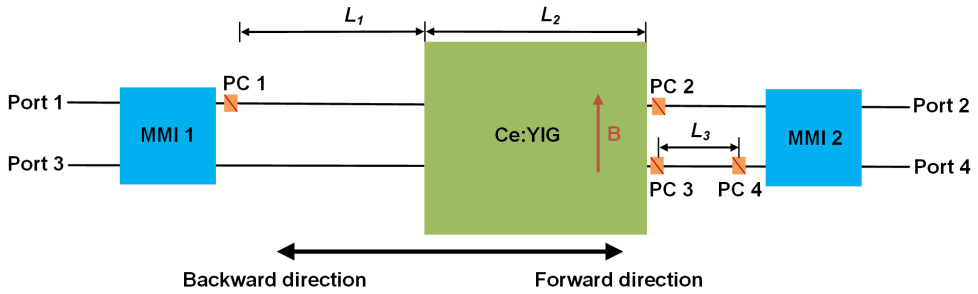

Figure 5.2: Schematic diagram of the MZI-based nonreciprocal device.

When the input light is in the TM mode and is injected from port 1, the reciprocal phase difference $\Delta\phi_{\mathrm{TM,RPS}}$ and the non-reciprocal phase difference $\Delta\phi_{\mathrm{TM,NRPS}}$ between the two branches for the forward direction can be written as

$$\Delta\phi_{\mathrm{TM,RPS}} = \beta_{\mathrm{TM},1} \cdot L_1 - (\beta_{\mathrm{TE},1} \cdot L_1 + \beta_{\mathrm{TE},2} \cdot L_2) \tag{5.1}$$

$$\Delta\phi_{\mathrm{TM,NRPS}} = \beta_{\mathrm{TM},2} \cdot L_2 \tag{5.2}$$

where $\beta_{\mathrm{TE},1}$ ($\beta_{\mathrm{TE},2}$) is the propagation constant of TE mode light that propagates in the branches without (with) the Ce:YIG layer. $\beta_{\mathrm{TM},1}$ ($\beta_{\mathrm{TM},2}$) is the propagation constant of the TM mode that propagates in the branches without (with) the Ce:YIG layer in forward direction.

The output power in two branches for the forward direction can be written as

$$I_2 = A^2 \sin^2\left(\frac{\Delta\phi_{\mathrm{TM,RPS}} + \Delta\phi_{\mathrm{TM,NRPS}}}{2}\right) \tag{5.3}$$

$$I_4 = A^2 \cos^2\left(\frac{\Delta\phi_{\mathrm{TM,RPS}} + \Delta\phi_{\mathrm{TM,NRPS}}}{2}\right) \tag{5.4}$$

where A is the amplitude of the input light.

Thus, the output power in the two ports can be tuned with $\Delta\phi_{\mathrm{TM,RPS}}$ and $\Delta\phi_{\mathrm{TM,NRPS}}$. When $\Delta\phi_{\mathrm{TM,RPS}}$ is $\pi/2+2n\pi$ (where n is an integer) and $\Delta\phi_{\mathrm{TM,NRPS}}$ is

$\pi/2+2m\pi$ (where m is an integer), light in the two branches is out-of-phase and is coupled out from port 2.

For the backward direction, the reciprocal phase difference $\Delta\phi'_{TM,RPS}$ and nonreciprocal phase difference $\Delta\phi'_{TM,NRPS}$ for TM mode light injected from port 2 in the two branches is

$$\Delta\phi'_{TM,RPS} = \Delta\phi_{TM,RPS} \tag{5.5}$$

$$\Delta\phi'_{TM,NRPS} = -\beta_{TM,2} \cdot L_2 = -\Delta\phi_{TM,NRPS} \tag{5.6}$$

The output power in two branches for the backward direction can be written as

$$I_1 = A^2 \sin^2\left(\frac{\Delta\phi_{TM,RPS} - \Delta\phi_{TM,NRPS}}{2}\right) \tag{5.7}$$

$$I_3 = A^2 \cos^2\left(\frac{\Delta\phi_{TM,RPS} - \Delta\phi_{TM,NRPS}}{2}\right) \tag{5.8}$$

The output power in the two ports 1,3 is also tuned with $\Delta\phi_{TM,RPS}$ and $\Delta\phi_{TM,NRPS}$. When $\Delta\phi_{TM,RPS}$ is $\pi/2+2n\pi$ and $\Delta\phi_{TM,NRPS}$ is $\pi/2+2m\pi$, light in the two branches is in-phase and is coupled out from port 3.

When the phase conditions mentioned above are matched, the TM mode light injected in port 1 will be coupled out from port 2, while the TM mode light injected in port 2 will be coupled out from port 3. Thus, an optical isolation can be achieved between port 1 and port 2, which means this device can work as an optical isolator. Furthermore, light in port 3 is directed to port 4, and input at port 4 is directed to port 1. Thus, a 4-port circulator operation is realized.

This device also works on the same principle when the input signal is TE mode. If the TE mode light is injected in port 1, the reciprocal phase difference $\Delta\phi_{TE,RPS}$ and nonreciprocal phase difference $\Delta\phi_{TE,NRPS}$ in the two branches for the forward direction can be written as

$$\Delta\phi_{TE,RPS} = (\beta_{TE,1} \cdot L_1 + \beta_{TE,2} \cdot L_2) - \beta_{TM,1} \cdot L_1 = -\Delta\phi_{TM,RPS} \tag{5.9}$$

$$\Delta\phi_{TE,NRPS} = -\beta_{TM,2} \cdot L_2 = -\Delta\phi_{TM,NRPS} \tag{5.10}$$

The output power in two branches for the forward direction can be written as

$$I_2 = A^2 \sin^2\left(\frac{\Delta\phi_{TE,RPS} + \Delta\phi_{TE,NRPS}}{2}\right) = A^2 \sin^2\left(\frac{\Delta\phi_{TM,RPS} + \Delta\phi_{TM,NRPS}}{2}\right) \tag{5.11}$$

$$I_4 = A^2 \cos^2\left(\frac{\Delta\phi_{\mathrm{TE,RPS}} + \Delta\phi_{\mathrm{TE,NRPS}}}{2}\right) = A^2 \cos^2\left(\frac{\Delta\phi_{\mathrm{TM,RPS}} + \Delta\phi_{\mathrm{TM,NRPS}}}{2}\right) \tag{5.12}$$

These are identical to Eqs. (5.3) and (5.4). When $\Delta\phi_{\mathrm{TM,RPS}}$ is $\pi/2+2\mathrm{n}\pi$ and $\Delta\phi_{\mathrm{TM,NRPS}}$ is $\pi/2+2\mathrm{m}\pi$, light in the two branches is out-of-phase and is coupled out from port 2. For the backward direction, the reciprocal phase difference and non-reciprocal phase difference in the two branches for TE mode light injected in port 2 can be written as

$$\Delta\phi'_{\mathrm{TE,RPS}} = \Delta\phi_{\mathrm{TE,RPS}} = -\Delta\phi_{\mathrm{TM,RPS}} \tag{5.13}$$

$$\Delta\phi'_{\mathrm{TE,NRPS}} = \beta_{\mathrm{TM},2} \cdot L_2 = \Delta\phi_{\mathrm{TM,NRPS}} \tag{5.14}$$

The output power two branches for the backward direction can be written as

$$I_1 = A^2 \sin^2\left(\frac{\Delta\phi'_{\mathrm{TE,RPS}} + \Delta\phi'_{\mathrm{TE,NRPS}}}{2}\right) = A^2 \sin^2\left(\frac{\Delta\phi_{\mathrm{TM,RPS}} - \Delta\phi_{\mathrm{TM,NRPS}}}{2}\right) \tag{5.15}$$

$$I_3 = A^2 \cos^2\left(\frac{\Delta\phi'_{\mathrm{TE,RPS}} + \Delta\phi'_{\mathrm{TE,NRPS}}}{2}\right) = A^2 \cos^2\left(\frac{\Delta\phi_{\mathrm{TM,RPS}} - \Delta\phi_{\mathrm{TM,NRPS}}}{2}\right) \tag{5.16}$$

These are identical to Eqs. (5.7) and (5.8). The output power in the two ports 1, 3 can also be tuned with $\Delta\phi_{\mathrm{TM,RPS}}$ and $\Delta\phi_{\mathrm{TM,NRPS}}$. When $\Delta\phi_{\mathrm{TM,RPS}}$ is $\pi/2+2\mathrm{n}\pi$ and $\Delta\phi_{\mathrm{TM,NRPS}}$ is $\pi/2+2\mathrm{m}\pi$, light in the two branches is in-phase and coupled out from port 3. An optical isolator or a 4-port circulator operation for TE mode light can thus be realized if the phase conditions are matched.

5.3 Optimization of the device performance

In this section, the 2×2 MMI, the PC, and the proposed nonreciprocal device are optimized to obtain a fully polarization-independent nonreciprocal device with high performance.

5.3.1 2×2 MMI couplers

Optical isolation is defined as the difference of transmission between forward and backward directions for a certain pair of ports. For MZI-based isolators and circulators, the optical isolation not only relies on the NRPS, also depends on the extinction ratio (ER) of resonance for both the bar and cross port pairs.

A schematic of the simplified device, which is a 2×2 MZI structure, is analyzed, as shown in Fig 5.3.

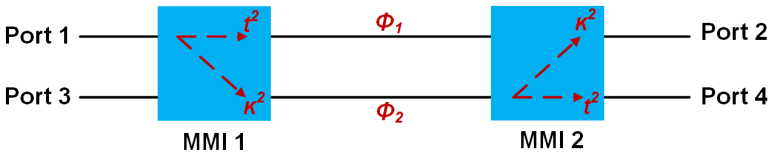

Figure 5.3: Schematic of a 2×2 MZI structure.

The relationship between the input and output electric fields of the MZI can be expressed as:

$$\begin{bmatrix} E_{\text{out},2} \\ E_{\text{out},4} \end{bmatrix} = \begin{bmatrix} t & -j\kappa \\ -j\kappa & t \end{bmatrix} \begin{bmatrix} e^{-j\phi_1} & 0 \\ 0 & e^{-j\phi_2} \end{bmatrix} \begin{bmatrix} t & -j\kappa \\ -j\kappa & t \end{bmatrix} \begin{bmatrix} E_{\text{in},1} \\ E_{\text{in},3} \end{bmatrix} \tag{5.17}$$

where $E_{in,1}$ and $E_{in,3}$ are the electric fields at the two inputs. $E_{out,2}$ and $E_{out,4}$ are the electric fields at the two outputs. The two MMIs are assumed to be identical. t and κ are the through-coupling coefficient and cross-coupling coefficient, respectively. ϕ_1 and ϕ_2 are the optical phase shifts of the two arms.

If light is launched into port 1, the output power at port 2 can be expressed as:

$$P_{\text{out},2} = \kappa^4 + t^4 - 2\kappa^2 t^2 \cos(\Delta\phi) \tag{5.18}$$

the output power at port 4 can be expressed as:

$$P_{\text{out},4} = 2\kappa^2 t^2 (1 + \cos(\Delta\phi)) \tag{5.19}$$

where κ^2 and t^2 are the cross-coupling ratio and the through-coupling ratio of the 2×2 MMI. $\Delta\phi$ is the phase difference between the two arms.

The ER for the cross and bar configuration can be expressed as:

$$ER_{\text{cross}} = 10\log_{10}\left(\frac{P_{\text{out},4}}{P_{\text{out},2}}\right) = 10\log_{10}\left(\frac{2\kappa^2 t^2(1+\cos(\Delta\phi))}{\kappa^4 + t^4 - 2\kappa^2 t^2\cos(\Delta\phi)}\right) \tag{5.20}$$

$$ER_{\text{bar}} = 10\log_{10}\left(\frac{P_{\text{out},2}}{P_{\text{out},4}}\right) = 10\log_{10}\left(\frac{\kappa^4 + t^4 - 2\kappa^2 t^2\cos(\Delta\phi)}{2\kappa^2 t^2(1+\cos(\Delta\phi)}\right) \tag{5.21}$$

It can be seen that the ER depends on the coupling ratio of the MMI. If κ^2 and t^2 are 0.5, the light input from port 1 will be output from port 4 when $\Delta\phi$ is 0. The light input from port 1 will be output from port 2 when $\Delta\phi$ is π.The imbalance of the MMI results in a reduction of the ER.

The splitting ratio and insertion loss for the two polarization states depend on the geometry of the 2×2 MMI. Fig 5.4(a) and (b) show the splitting ratio and insertion loss of the 2×2 MMI as a function of the 2×2 MMI length at a wavelength of 1550 nm.

The imbalance and insertion loss differ for the two polarizations. Although a perfect length with balanced output for the two polarization states is not obtained, less than 1 dB imbalance and insertion loss are achieved for the 2×2 MMI with lengths between 26.0 μm and 27.5 μm.

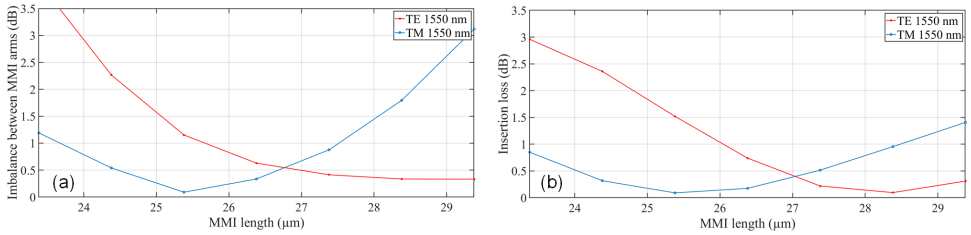

Figure 5.4: Simulated length dependence of a 2×2 MMI at 1550 nm. (a) Imbalance between two arms. (b) Insertion loss.

The wavelength dependence of the 2×2 MMI is also analyzed. Fig 5.5 (a) and (b) show the splitting ratio and insertion loss of the 2×2 MMI as a function of wavelength when the MMI length is 26.38 μm. It can be found the imbalance and insertion loss for the two polarization states vary within 1.5 dB for a wavelength range of 100 nm.

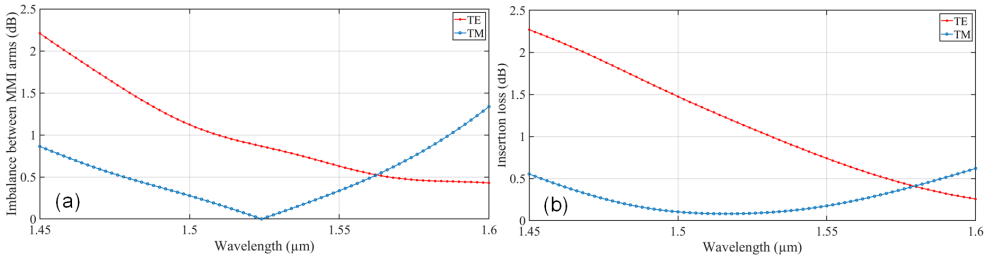

Figure 5.5: Simulated wavelength dependence of a 2×2 MMI with a length of 26.38 μm. (a) Imbalance between two arms. (b) Insertion loss.

The imbalance of the MMI should be close to zero in a wide wavelength range for the device to function as a broadband circulator. According to Eq. (5.20), 1.5 dB imbalance results in only 15.8 dB ER for the cross configuration when when $\Delta\phi$ is zero. The measurement results of the device and further analysis are explored in next section.

5.3.2 Polarization converter (PC)

The optical isolation of this device not only depends on the splitting ratio of the 2×2 MMI, but also depends on the PCE of the PC. A more detailed calculation using Jones matrix can be found in Appendix B. In the previous section, the PCE of the PC is assumed to be 100% for all the wavelengths. However, this is nearly impossible to achieve due to fabrication imperfections and wavelength dependence of the PC.

PCs have been investigated and demonstrated in the IMOS platform [27]. In this section, the performance of a PC, with 1.7 μm and 2.3 μm lengths of the two triangular sections, are analyzed in a eigenmode expansion (EME) solver. Fig 5.6(a) and (b) show the PCE and the insertion loss of this PC . Over 99% PCE and less than 1 dB insertion loss can be found in a 100 nm wavelength range.

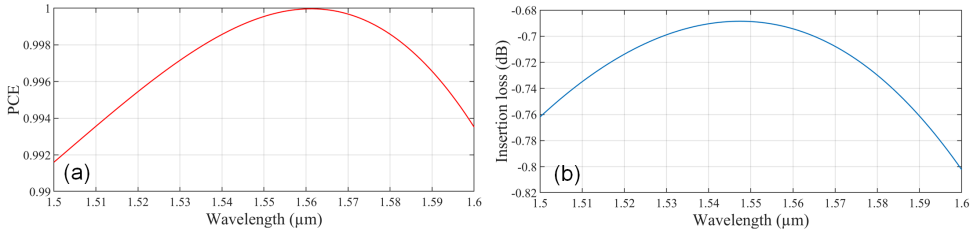

Figure 5.6: PCE and insertion loss of the PC.

Although over 99% PCE in a 100 nm wavelength range is obtained in simulation, it is still difficult to reach such a high efficiency in reality due to fabrication imperfections. In fabrication, the vertical sidewall of the PC is covered by a 50 nm SiN layer. Then, a wet-etch step is performed create the triangular sections. To make sure the areas to be wet-ecthed are fully opened, the SiN layer is over-etched. This will result in a height reduction of the PC. Hence, the performance of the PC is affected.

For a PC with 1.7 μm and 2.3 μm lengths of the two triangular sections, the measured PCE at 1550 nm is about 95% [98]. The incomplete conversion brings extra insertion loss and impacts the optical isolation of the device, according to the calculation in Appendix B.

5.3.3 Nonreciprocal device

The optimized 2×2 MMIs and the PCs are implemented into the proposed nonreciprocal device. Then, the device is simulated with a FDTD solver. To reduce the simulation time, the bonding layer between the waveguide and the Ce:YIG is excluded. The optical absorption of the Ce:YIG is also ignored.The length of Ce:YIG is tuned from 0 to 1 mm, in steps of 0.05 mm. The simulation results for an input of TE-polarized light at 1550 nm are shown in Fig 5.7.

The vertical axis is the transmission in the proposed device as illustrated in Fig 5.1. The horizontal axis is the length of Ce:YIG. Fig 5.7(a) shows the transmission in port 3 and port 4 for forward direction. Fig 5.7(b) shows the transmission in port 1 and port 2 for backward direction.

In Fig 5.7, the transmission in the two output ports is periodically changing with the length of Ce:YIG. The periods for forward and backward directions are different, because of the NRPS effect as illustrated in the previous section.

In Fig 5.7(a), when the length of Ce:YIG is 0.75 mm, the TE mode signal entered from port 1 will mostly pass through port 4 in the forward direction. The crosstalk is 40.1 dB between port 3 and port 4. This is because the phase difference is not exactly π when Ce:YIG is 0.75 mm. A larger crosstalk between will be found if a

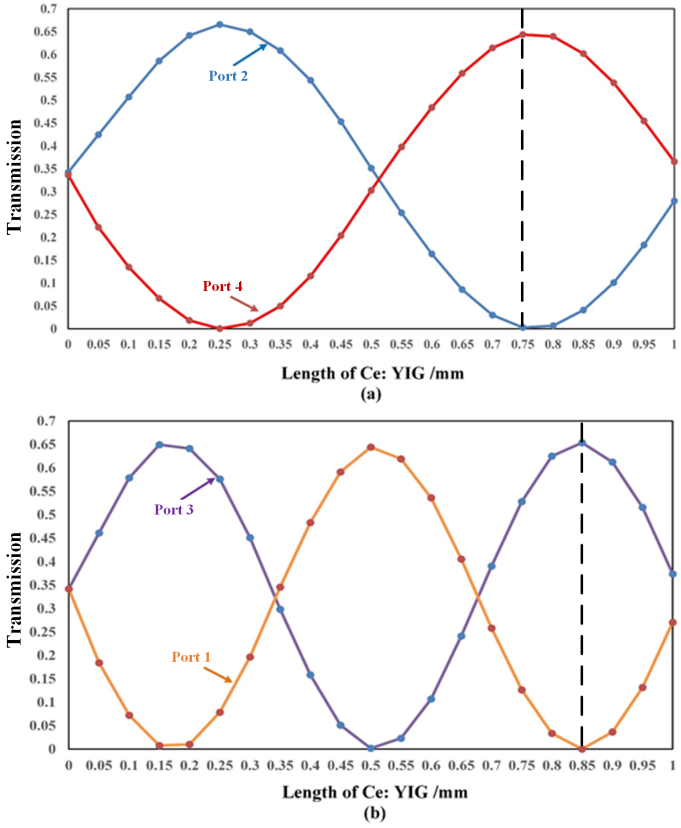

Figure 5.7: Transmission as a function of the length of the Ce:YIG, for a TE polarized input signal. (a) In forward direction (input from port 1). (b) In backward direction (input from port 4).

narrower sweep step is used. The insertion loss is 1.7 dB. This insertion loss can be attributed to different sources: i) scattering loss and reflection in the MMI, ii) reflection at the interface between the waveguide and the Ce:YIG layer, iii) reflection at the interface between the triangular waveguide and the rectangular waveguide in the PC. In Fig 5.7(b), when the length of Ce:YIG is 0.85 mm, the TE mode signal entered from port 4 will mostly pass through port 2 in the backward direction. The crosstalk that can be obtained is 41.2 dB between port 1 and port 2. The insertion loss is 1.8 dB. The reason that the crosstalk and insertion loss are slightly different for forward and backward direction is that the optimal length of Ce:YIG is different. The device performance can be further improved if an optimal Ce:YIG length is found for two propagation directions.

The electrical fields of the TE mode propagating along the circulator for two different propagation directions are shown in Fig 5.8 when the length of Ce:YIG coated waveguide section is optimized. In Fig 5.8(a), the TE mode enters from port 1 and

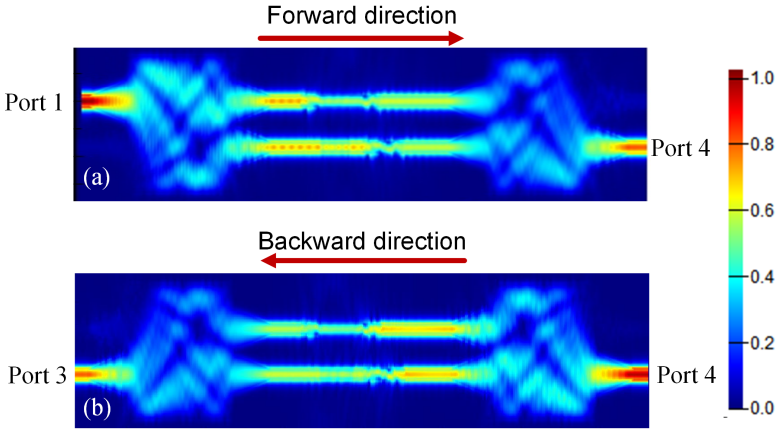

Figure 5.8: Electrical field propagating along the InP waveguide of the TE mode. (a) in forward direction. (b) in backward direction.

emits from port 4 in the forward direction. In Fig 5.8(b), the TE mode enters from port 4 and emits from port 3 ,instead of port 1, in the backward direction, meaning the NRPS becomes effective.

5.4 Device fabrication and characterization

This device is fabricated in the IMOS platform. The fabrication process is the same as the nonreciprocal polarization converter, which is discussed in Chapter 4. The designed mask is shown in Fig 5.9(a). The four square markers are designed to align the four corners of the Ce:YIG die. Fig 5.9(b) is a microscope image of the fabricated sample. It can be seen that a 4×4 mm^2 Ce:YIG die is bonded on the waveguides.

In the mask, two different characterization structures are designed, which are shown in Fig 5.10. TE and TM grating couplers are placed on both sides of the device and are connected with two 2×2 MMIs. The PC in this design is only 4 μm long. This length can be neglected compared to the 4 mm long Ce:YIG die. In Fig 5.10(a), the distance between two PCs (ΔL_2) is 4.8 mm. All the PCs are outside the bonding area. In Fig 5.10(b), the distance between two PCs (ΔL_1) is 2 mm. All the PCs in are covered by the 4 mm long Ce:YIG die.

A grating-coupler setup, as shown in Fig 4.10, is used to characterize the device. TE (TM) grating couplers are used to couple TE (TM) light into or out of the device with fibres.

5.4.1 Isolator characterization

To characterize the device as an optical isolator, the transmission spectra through port 2 and port 3 are recorded from both TE and TM grating couplers for forward and backward propagation direction.

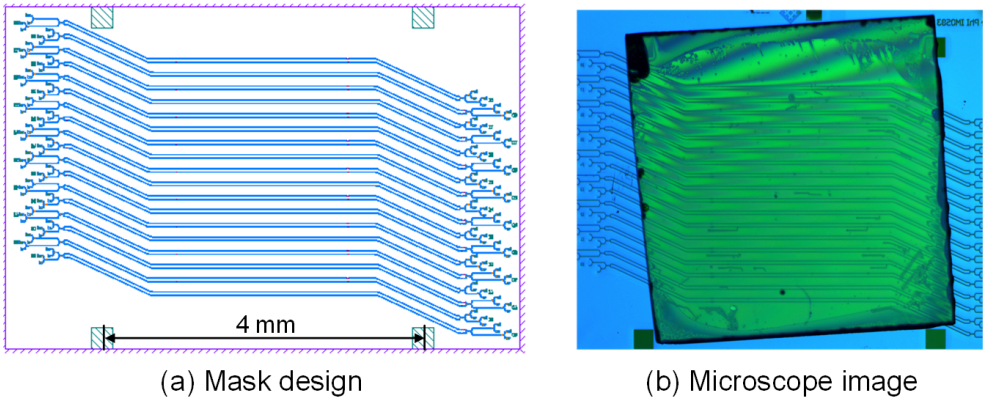

Figure 5.9: (a) The designed mask pattern. (b) Microscope image (through a polarizer) of the fabricated devices with a bonded Ce:YIG die.

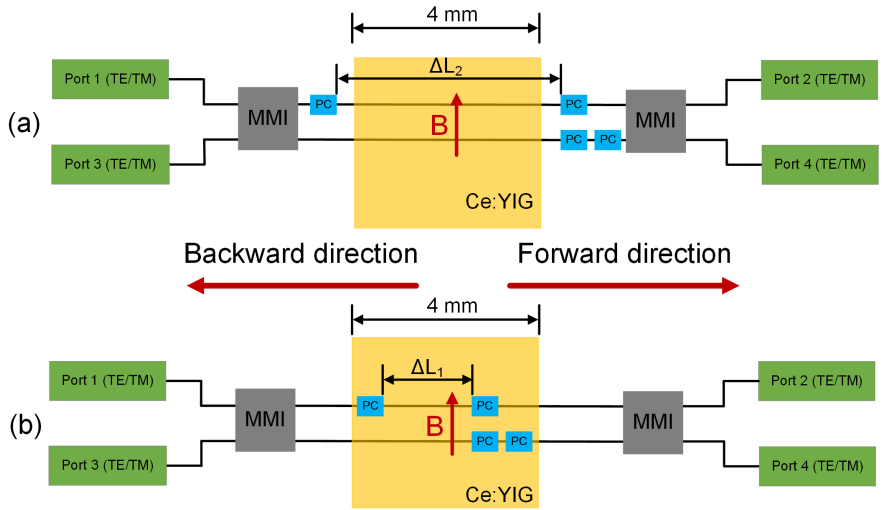

Figure 5.10: Two different characterization structures. (a) PCs outside the bonding area. (b) PCs inside the bonding area.

The device that is shown in Fig 5.10(a) is measured. The transmission spectra of the TE mode light between port 2 and port 3 are shown in Fig 5.11(a). The wavelength shift between the spectra of two transmission directions is around 1.2 nm. An optical isolation of 24.1 dB is measured at 1539.6 nm. Fig 5.11(b) shows the transmission spectra of TM mode light between port 2 and port 3. A wavelength shift of around 1.2 nm is again obtained. An optical isolation of 34.0 dB is measured at 1539.2 nm. The 1.2 nm wavelength shift for both TE and TM mode light corresponds to a reciprocal phase shift of $(\pi/2+2n\pi)$ and a non-reciprocal phase difference of π. The wavelength where the maximum isolation is achieved for TE and TM mode light

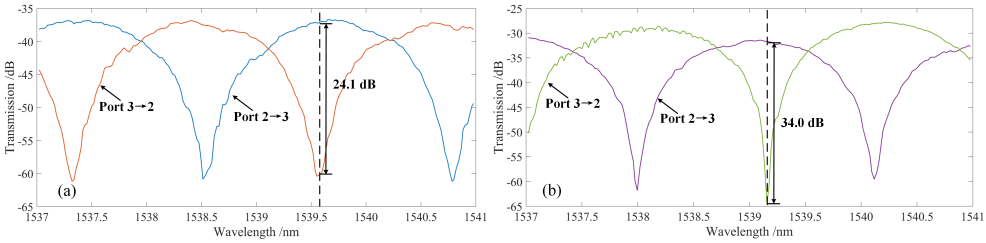

Figure 5.11: Transmission spectra of the device in Fig 5.10(a) between port 2 and port 3 for (a) TE mode light. (b) TM mode light.

differs by 0.4 nm. According to the theoretical analysis in the previous sections, this wavelength offset should be zero.

An explanation is that there is a phase error between the two arms. It originates from the deviation in the waveguide dimensions of the two arms. Phase errors has also been noticed in other MZI structures in the IMOS platform. The deviation in the waveguide dimensions is caused by fabrication imperfections, such as non-uniformity in the dry etching step or unexpected stress in the bonding process.

A polarization-independent optical isolator can be claimed if this phase error can be eliminated by improving the fabrication process. Another solution is to implement a phase shifter (e.g. thermal-optic phase shifter) in one arm to tune the reciprocal phase difference in the two arms.

The 20 dB optical isolation bandwidth represents a wavelength range in which the isolation ratio is more than 20 dB. In Fig 5.11(a) and (b), the measured 20 dB bandwidths for the two polarization states are both 0.2 nm. The reason of this narrow bandwidth is that the FSR of this device is only about 2.3 nm. In the design, the two branches of the MZI have the same length. However, there is always the TE mode in one branch and the TM mode in the other branch, regardless the input is the TE or TM mode. The different propagation constants of the two modes results in an imbalance of the MZI. For practical application purposes, a larger bandwidth is desired.

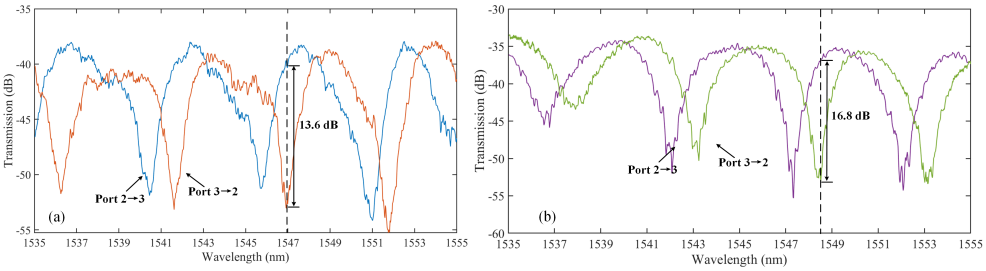

Figure 5.12: Transmission spectra of the device in Fig 5.10(b) between port 2 and port 3 for (a) TE mode light. (b) TM mode light.

The device that is shown in Fig 5.10(b) is also measured. The length of the waveguide (ΔL_1) between the two PCs in the upper branch is 2 mm. All the PCs are covered by the bonding layer and the Ce:YIG die. The optimized lengths for the two

triangular sections of the PC are 2.8 μm and 3.7 μm in the FDTD solver, to reach the maximum PCE.

The transmission spectra for the TE and TM modes between port 2 and port 3 are recorded in Fig 5.12(a) and (b). The FSR of this device is 5.0 nm. The spectral shift between the spectra of two transmission directions is about 1.2 nm. An optical isolation of 13.6 dB is measured at 1547.0 nm for the TE mode ,and an optical isolation of 16.8 dB is measured at 1548.5 nm for the TM mode.

Compared with the performance of the device in Fig 5.10(a), this device shows larger insertion loss, larger optical bandwidth, and lower optical isolation.

The insertion loss of this structure is a few dB higher than the one in Fig 5.10(a). This extra insertion loss may be from two aspects: i) the incomplete PCE of the PC. The unconverted light cannot be coupled out from the polarization-dependent grating couplers. Thus, it will contribute as part of the insertion loss. ii) The reflection between the triangular waveguide section and the rectangular waveguide section. Since the PCs are covered by a bonding layer and a Ce:YIG layer, there will be a mode mismatch between the triangular waveguide section and the rectangular waveguide section, and causes reflection.

The larger bandwidth derives from the shorter waveguide between the two PCs in the upper branch. The imbalance of the MZI configuration is less if ΔL_1 is shorter. However, the 2 mm long waveguide covered with the Ce:YIG die is not efficient enough to achieve π rad NRPS. The spectral shift corresponds to an NRPS of 86.4°. This value is comparable to the simulation results in Fig 3.6. Therefore, for this design, there is a trade-off between the optical isolation and the isolation bandwidth.

In principle, reducing the thickness of the bonding layer can enhance the NRPS. A device with larger optical isolation and larger bandwidth can be achieved by using a shorter Ce:YIG die and a thinner bonding layer. For example, for a device with a 2 mm long Ce:YIG die and 18 nm thick bonding layer, the predicted optical isolation is over 30 dB and the predicted 20 dB isolation bandwidth is about 0.5 nm. Another method to improve the bandwidth to tens of nanometers without degrading the nonreciprcoal performance of the device is discussed in Chapter 6.

Another reason that this device shows lower optical isolation is because of the relatively low ER in this structure. The ER varies from 14 dB to 18 dB and from 11 dB to 20 dB for the TE and TM modes, respectively. This low ER could be because the PCE of the PC is lower than the one in the first device. The InP membrane will be stretched during the InP-to-Si bonding process due to thermal mismatch. For a PC with longer length, the impact of this stretch becomes more significant.

It can aslo be observed that there are ripples with a period of about 0.25 nm in the spectra in Fig 5.12(a) and (b). These ripples indicate that there is a cavity in the circuit, which gives unwanted reflection. The length of this cavity can be calculated by:

$$L_{\text{cavity}} = \frac{\lambda^2}{2n_g\Delta\lambda} \tag{5.22}$$

where n_g is the group index. In this structure, the group index for the InP waveguide covered with Ce:YIG is 3.5 at 1550 nm, obtained from a FEM solver. Hence, the cal-

culated cavity length is 1.4 mm. This value is close to the waveguide length between the two PCs, which forms a Fabry-Perot cavity because of the mode mismatch.

5.4.2 Circulator characterization

To characterize the device as an optical circulator, the transmission spectra of the four ports are recorded from both TE and TM grating couplers for forward and backward propagation direction.

The device that is shown in Fig 5.10(a) is measured. The transmission spectra of TE light input in clockwise direction (Port 1→Port 2→Port 3→Port 4→Port 1) and counter-clockwise direction (Port 1→Port 4→Port 3→Port 2→Port 1) are shown in Fig 5.13(a) and (b). The measured transmittance of two cascaded TE grating couplers is also shown in Fig 5.13(a). The operating wavelengths in the clockwise direction and counter-clockwise directions are highlighted with the dashed vertical line and the solid vertical line, respectively.

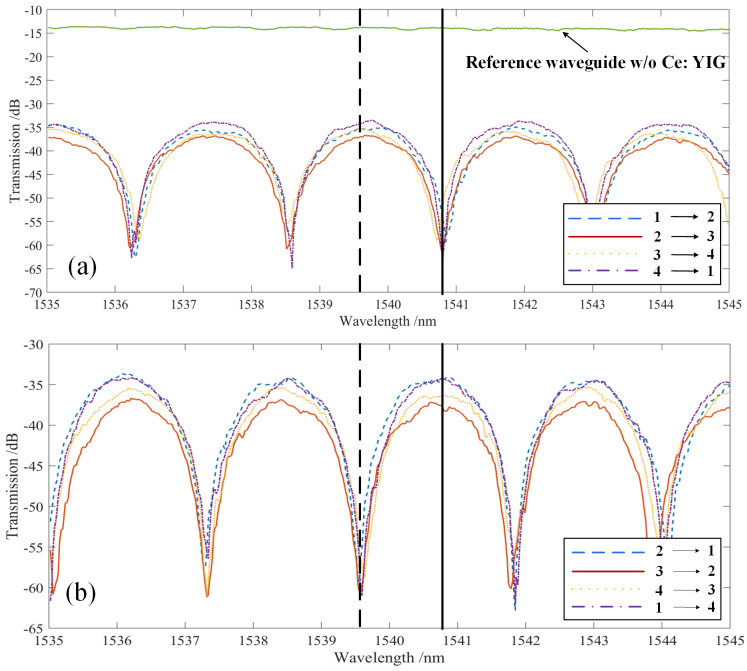

Figure 5.13: Transmission spectra of the device in Fig 5.10(a) for different circulating directions for TE mode input in (a) clockwise direction and (b) counter-clockwise direction.

The transmittance of the TE mode at 1539.6 nm is summarized in Table 1 for the four input/output ports. The transmittance for clockwise direction at this wavelength is between -36.9 dB and -34.0 dB. As shown in Fig 5.13(a), the fibre-to-waveguide coupling loss is measured to be 13.8 dB. A 3-dB coupler is placed at the output port to split the light to TE and TM grating couplers, respectively. The PC gives around

1.0 dB loss and the 2×2 MMI gives around 1.0 dB loss. Another 3.0 dB loss is observed from the device with Ce:YIG compared to the device without Ce:YIG. This excess loss is attributed to optical absorption of Ce:YIG, and to scattering and reflection at the boundaries of the Ce:YIG cladding regions. The remaining insertion loss is attributed to the propagation loss of the waveguide, which is around 11.0 dB/cm in this fabrication run. In this device, the waveguide section is 5.8 mm long, which will bring around 6.4 dB loss. This large waveguide loss is attributed to the sidewall roughness induced during the EBL step. A record low waveguide loss of 1.8 dB/cm was demonstrated on the IMOS platform utilizing 193-nm Deep UV Lithography [31], which could reduce the waveguide loss significantly. The insertion losses can be further improved by shortening the length of the Ce:YIG die (the length of the waveguide section covered with Ce:YIG is shortened as well then), and by optimizing the design of the PCs and MMIs.

The measured optical isolations are 27.0 dB and 24.1 dB for the cross-port pairs, while optical isolations for the bar-port pairs are 19.9 dB and 18.6 dB. The variations of the optical isolations for cross and bar port pairs are caused by the incomplete conversion of the PC. For the PCs implemented in this device, the measured polarization conversion efficiency (PCE) is 96%±0.5%. This can be improved by optimizing the PC design.

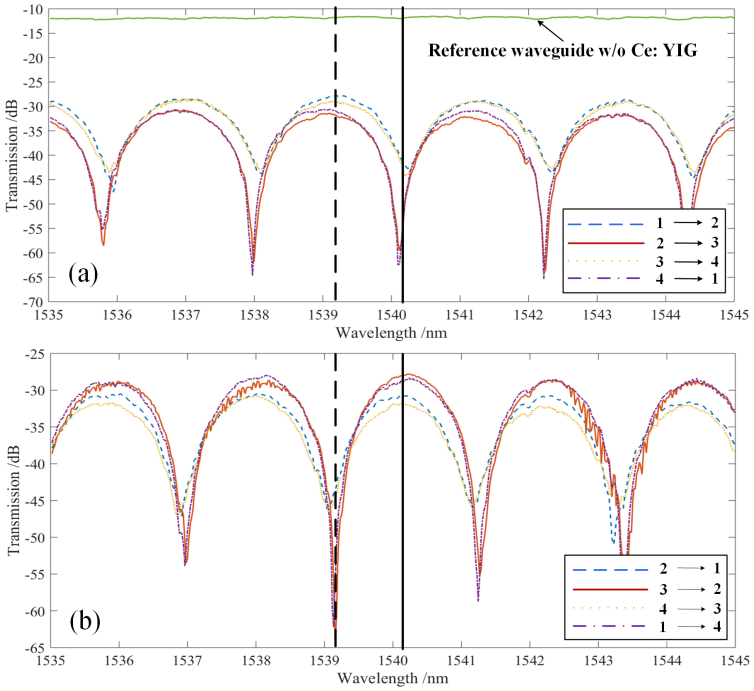

Figure 5.14: Transmission spectra of the device in Fig 5.10(a) for different circulating directions for TM mode input in (a) clockwise direction and (b) counter-clockwise direction.

The transmission spectra of the TM mode input for clockwise direction and counter-clockwise direction are shown in Fig 5.14(a) and (b). The measured transmittance of two cascaded TM grating couplers is shown in Figure 5.14(a). The operating wavelengths in clockwise direction and counter-clockwise directions are highlighted with the dashed vertical line and the solid vertical line, respectively.

Table 5.1. Transmission for the input/output port combinations for TE mode input

Input	**Output (dB)**			
	Port 1	Port 2	Port 3	Port 4
Port 1	-	-35.3	-	-61.0
Port 2	-55.2	-	-36.9	-
Port 3	-	-61.0	-	-35.9
Port 4	-34.0	-	-54.5	-

Table 5.2. Transmission for the input/output port combinations for TM mode input

Input	**Output (dB)**			
	Port 1	Port 2	Port 3	Port 4
Port 1	-	-27.8	-	-62.2
Port 2	-44.6	-	-30.9	-
Port 3	-	-64.9	-	-28.8
Port 4	-31.3	-	-45.2	-

The transmittance of the TM mode at 1539.2 nm is summarized in Table 2 for the four input/output ports. The transmittance for clockwise direction at this wavelength is between -27.8 dB and -31.3 dB. The insertion loss for the TM mode is less than the insertion loss for the TE mode. This is because the TE mode suffers from more propagation loss from the sidewall roughness, due to the mode distribution in the waveguide. The measured optical isolations are 30.9 dB and 34.0 dB for the cross-port pairs, while optical isolations for the bar-port pairs are 16.8 dB and 16.4 dB.

The difference of optical isolations between the cross and bar configuration for the TM mode is larger than the difference for the TE mode. In this device, the power splitting ratio is closer to 50:50 for the TE mode than for the TM mode. This can be improved by optimizing the 2×2 MMI design.

5.5 Summary

In this chapter, an integrated optical nonreciprocal device is experimentally demonstrated. The device is realized with adhesively bonding a Ce:YIG die to a MZI-based structure in the IMOS platform.

The device works as an optical isolator between ports at the opposite side of the MZI. Two different structures are characterized. Maximum Optical isolations of 27.0 dB and 34.0 dB are obtained for the TE and TM mode input, respectively. This device is polarization independent if the phase error in the two arms can be avoided. The optical isolation bandwidth is within 0.5 nm, and can be improved by reducing the imbalance between the two arms.

The structure can also function as an optical circulator when using all the four input/output port combinations. For TE polarized light, 27.0 dB and 24.1 dB optical isolations are obtained for the cross-port pairs in that case, while 19.9 dB and 18.6 dB

optical isolations are measured for the bar-port pairs. For TM mode light, 30.9 dB and 34.0 dB optical isolations for the cross-port pairs, and 16.8 dB and 16.4 dB optical isolations for the bar-port pairs, are obtained. The sources of the insertion losses are studied, and the methods to reduce the insertion loss are also discussed. The 2×2 MMI design needs to be optimized to reduce the imbalanced power splitting ratio for both TE and TM mode.

To claim a compact, broadband, low loss, and polarization independent optical isolator/circulator, further improvements still need to be done, and will be discussed in the next chapter.

Chapter 6

Designs for a broadband tunable nonreciprocal device

In Chapter 5, an integrated optical nonreciprocal device has been demonstrated. However, the device still suffers from high insertion loss, narrow bandwidth and large footprint. In this chapter, several new designs and methods are proposed to achieve a broadband, tunable, low-loss and compact nonreciprocal device. Unfortunately, due to unexpected failure in the fabrication process, the purpose of this chapter is to describe the ideas.

6.1 Integrated electromagnet

For optical nonreciprocal devices using the Ce:YIG film, an external static magnetic field is needed. As discussed in Section 5.4, a Nd-Fe-B magnet is described in our measurement set-up to provide a static transverse magnetic field. However, this bulk magnet adds significant device footprint and limits the co-integration of the nonreciprocal devices with other optical components.

An electrically driven integrated optical isolator was demonstrated in 2016 [82]. After the Ce:YIG on SGGG die is bonded on the Si wafer, the SGGG substrate is polished from 500 μm down to around 5 μm. Then, a multi-coil electromagnet is fabricated on the SGGG substrate. A 80 mA DC current is applied in the electromagnet to reach a magnetic field the largest optical isolation.

However, the mechanical polishing technique used to reduce SGGG thickness brings extra risk and complexity in fabrication. The waveguides could be damaged if they are exposed in the grinding tool. Also, the garnet residues may be attached to the waveguide and bring extra propagation loss. Moreover, the generated electrical power in the microstrip causes a thermal-optic wavelength shift in the microring structure. This thermal-optic shift will limit the performance of the device.

6.1.1 Device design

Thanks to the advantage of double-side processing in the IMOS platform, an electromagnet can be fabricated before bonding the InP membrane onto a Si wafer. So, the mechanical polishing of the SGGG substrate is avoided. The cross-section of the IMOS waveguide integrated with an electromagnet is shown in Fig 6.1.

The electromagnet is about 1 μm away from the Ce:YIG layer and is patterned on a layer of polyimide, which is used as a support material, as shown in Fig 6.1. The fabrication process of the electromagnet is compatible with the IMOS process flow. After the electromagnet is defined, a BCB bonding process is performed. So, the metal layer is buried underneath the InP membrane. An extra lithography cycle is needed to open the metal pads. A transverse magnetic field is generated to magnetize the Ce:YIG film when a direct current is injected into the electromagnet.

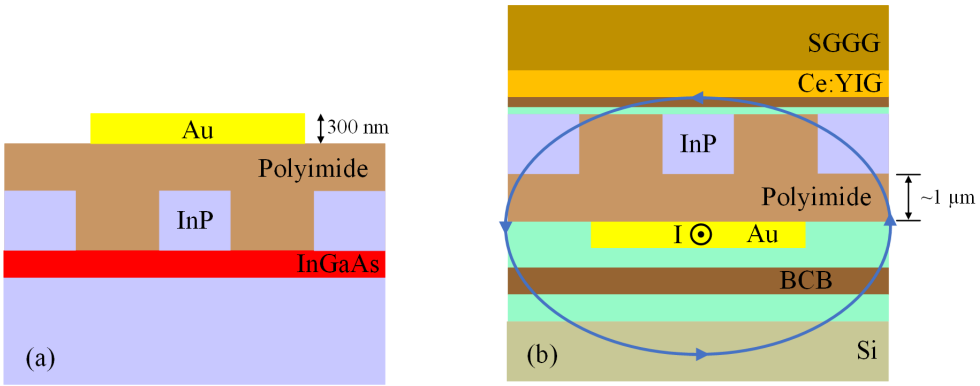

Figure 6.1: Cross-section of the IMOS waveguide with an electromagnet (a) before bonding. (b) after bonding.

6.1.2 Simulation

To reduce local heating when a direct current is applied, the resistance of the electromagnet must be kept low. Therefore, the designed electromagnet is 100 μm in width, 2 mm in length, 300 nm in height. The calculated resistance is 1.5 Ω. The magnetic and thermal performance of the electromagnet is simulated with COMSOL Multiphysics.

Fig 6.2(a) shows the magnetic flux intensity on the surface of the electromagnet when a 105 mA direct current is applied. The red arrows indicate the direction of the magnetic field. Fig 6.2(b) shows the magnetic flux density on the surface of the Ce:YIG film (1 μm away from the electromagnet) as a function of the applied current. The red dashed line indicates that 105 mA direct current can provide 5 mT (50 Oe) magnetic field to saturate the Ce:YIG in the in-plane direction, as discussed in Chapter 2.

Fig 6.3 shows the cross-section of the temperature distribution when a 105 mA direct current is applied. The InP waveguide is 300×400 nm^2, and is 1 μm above the

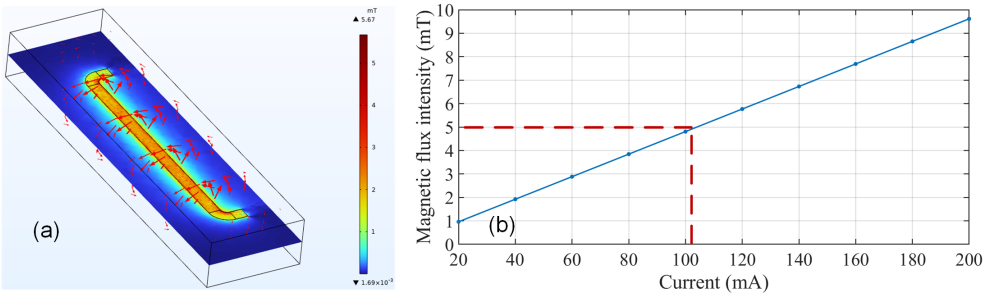

Figure 6.2: (a) Magnetic flux distribution of the electromagnet. (b) Magnetic flux density on the surface of the Ce:YIG film as a function of the applied current.

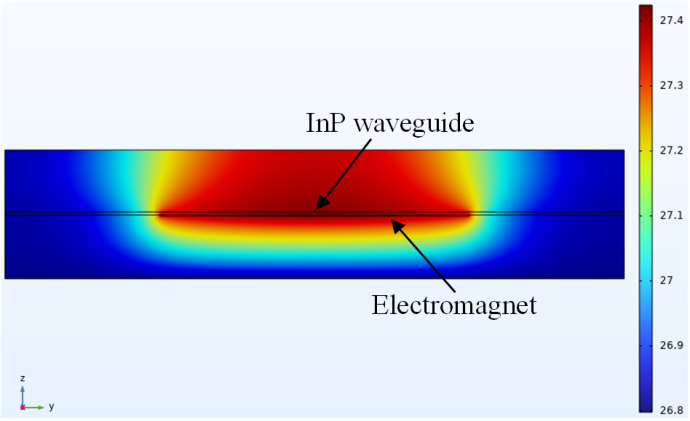

Figure 6.3: Cross-section of the temperature distribution.

electromagnet. It can be seen that the temperature of the InP waveguide increases around 0.5 °C. The calculated phase shift induced by the heating is about 23°. The electromagnet is placed underneath a MZI structure, light propagating in the two arms will experience same amount of phase shift. Hence, this temperature variation will not induce extra resonance wavelength shift. Moreover, it has been tested that the residual magnetization of the Ce:YIG film can last for at-least three months [56]. So, the device can be characterized and used when the current is off.

6.1.3 Fabrication and characterization

The electromagnets are fabricated in an IMOS passive run, together with the thermal-optic phase shifters. The actual metal layerstack is 25 nm Ti and 275 nm Au instead of the 300 nm Au used in simulation. The thin Ti layer is used to improve the adhesion. The metal layer is on top of the InP membrane with a layer of polyimide in between. Fig 6.4 shows the InP wafer after a metal lift-off step and the zoom-in microscope image of an electromagnet and a phase shifter.

The InP wafer is bonded on a Si wafer after this metal lift-off step. Then, the

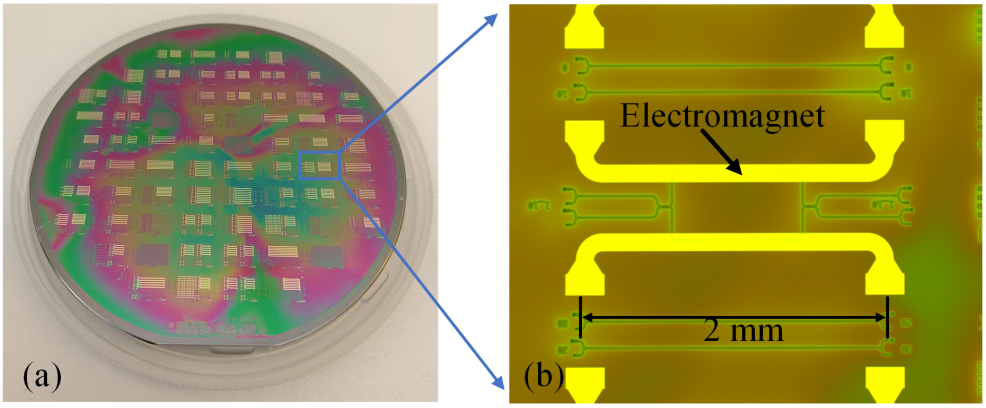

Figure 6.4: (a) Photo of the InP wafer after metal lift-off. (b) Microscope image of a electromagnet.

metal pads are opened for the placing of electrical probes. Unfortunately, the InP membrane was damaged during the substrate removal process, as shown in Fig 6.5. It was noticed that the damage at the edge of the wafer is greater than at the center area. The reason might be that the HCl solution penetrates the polyimide layer and reaches the InP membrane. The polyimide layer fails to provide a hermetic seal during the substrate removal process, and allows HCl to lift off the InP membrane layer. This could be solved by deposit a thin layer of SiO_2 as a protection layer on the InP membrane before spinning polyimide.

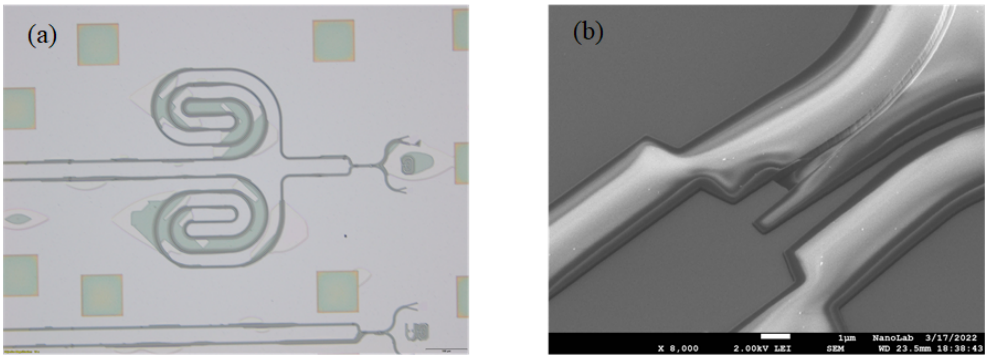

Figure 6.5: (a) Microscope image of the InP membrane (The blueish areas indicates that the membrane is damaged). (b) SEM image of a damaged MMI (one branch of the MMI is missing).

6.2 Thermal-optic phase shifter

The implementation of thermal-optic phase shifters in the nonreciprocal devices brings two main advantages. First, as discussed in Chapter 5, the nonreciprocal device can be polarization-independent if a phase shifter is used to compensate the phase error. Second, the optical phase condition can be satisfied by thermally tuning the phase in one arm, and the operation wavelength is also tuned.

The cross-section of a thermal phase shifter is shown in Fig 6.6(a). A layer of Au is underneath the InP waveguide. A 1 μm polyimide layer is used as a support material. The thermal-optic phase shifter shares the same layerstack and process flow as the integrated electromagnet. Fig 6.6(b) shows a microscope image after the metal-lift-off process. It can be seen that two phase shifers on the two arms of a MZI structure are patterned. After the InP-to-Si bonding process, another lithography cycle is needed to open the metal pads in order to apply current.

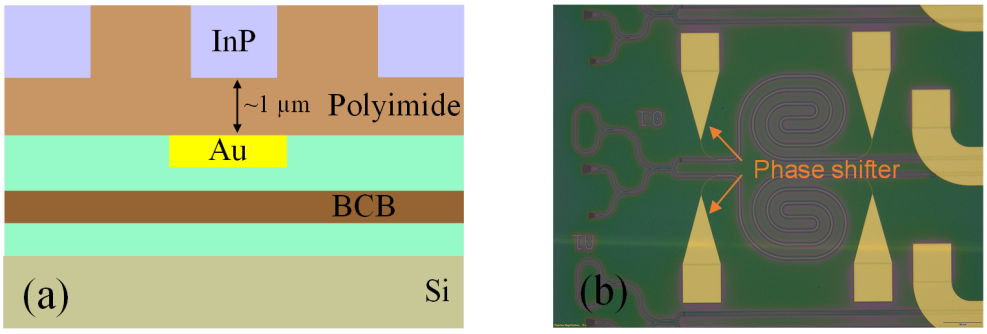

Figure 6.6: (a) Cross-section of the phase shifter after the bonding process. (b) Microscope image of two phase shifters before the bonding process.

The thermal-optic phase shift $\Delta\phi$ can be expressed as

$$\Delta\phi = \frac{2\pi L}{\lambda}\frac{\mathrm{d}n}{\mathrm{d}T}\Delta T \tag{6.1}$$

where L is the length of the phase shifter. $\frac{\mathrm{d}n}{\mathrm{d}T}$ is the thermo-optic coefficient. For an InP waveguide, $\frac{\mathrm{d}n}{\mathrm{d}T} = 2\times10^{-5}$ K^{-1} at $\lambda = 1550$ nm, T = 300 K [105]. In order to obtain sufficient thermal-optic efficiency, the metal layer is 300 nm in height, 1 μm in width and 1 mm in length. The calculated temperature variation to reach π phase shift is 3.9 °C.

The thermal-optic performance of the phase shifter is simulated in COMSOL Multiphysics. Fig 6.7 shows the temperature distribution when a 200 mA direct current is applied. The increased temperature in the InP waveguide is enough to provide π phase shift. Unfortunately, due to the damaged membrane, the performance of this device cannot be characterized.

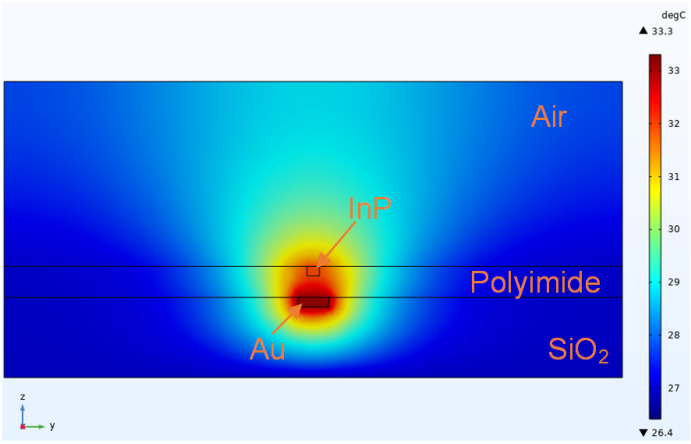

Figure 6.7: Temperature distribution of the electromagnet.

6.3 Shallow-to-deep waveguide transitions

For the optical nonreciprocal devices discussed in Chapter 5, 6.4 dB propagation loss is induced by a 5.8 mm long waveguide section. The high propagation loss is due to scattering loss from sidewall roughness, which is created by the ICP etch step and the planarization step in the RIE tool. By replacing the deep-etched waveguides with shallow-etched waveguides, the propagation loss induced by the ICP etch step can be mitigated. The SiO_2 pillars discussed in Section 3.3, Chapter 3 can also be avoided. However, deep-etched waveguide sections are still inevitable in the device because of the PCs. Hence, a shallow-to-deep waveguide transition taper is needed to connect the two waveguides with different dimensions.

In addition, such a transition taper can also be used to couple light from the input/output waveguides to the unetched free propagation region (FPR) in a planar concave grating (PCG). A properly designed shallow-to-deep waveguide transition could provide an efficient coupling and reduce the insertion loss.

In the past decades, different designs of shallow-to-deep waveguide transitions have been proposed both on SOI [106, 107] and III-V platform [108]. These taper designs are optimized in simulation to reach high transmission (>99%) and low mode conversion (<1%). However, these designs might not be suitable to the IMOS platform because the change of waveguide dimensions and layerstacks.

A design of a shallow-to-deep waveguide transition is proposed [36], based on the IMOS platform. Over 99% transmission for TE mode light is obtained with a taper length of 24 μm and an interface length of 2.1 μm. However, the shallow and deep widths are fixed to 2 μm and 0.8 μm in the design, which does not match with the waveguide widths in this thesis. Additionally, the transmission for TM mode light is not investigated.

To reduce the insertion loss of the nonreciprocal device, in this section, two different taper designs for shallow-to-deep waveguide transitions, a bi-level taper and a

butt-jointed taper, are developed for the IMOS platform.

6.3.1 Device design

Fig 6.8(a) shows the schematic of the bi-level taper. The deep-etched waveguide section is 400 nm in width (w_0) and 300 nm in height (h_0), which are the standard dimensions of the passive waveguide in the IMOS platform. The shallow-etched waveguide section is 400 nm in width (w_0) and 120 nm in height (h_1).

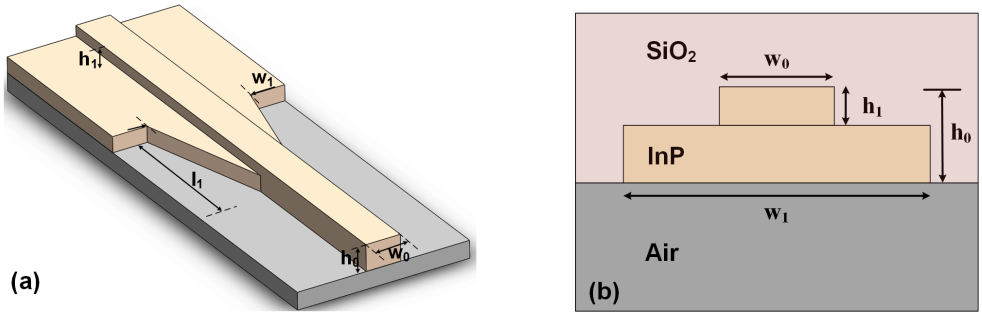

Figure 6.8: (a) the schematic of the bi-level taper. (b) the cross-section at the taper section (at the shallow waveguide side).

The shallow waveguide etch depth is chosen to be the same as the etch depth of the grating couplers in the IMOS platform. This is beneficial since it simplifies the processing. The taper will maintain an adiabatic transition for the propagating light. Fig 6.8(b) shows the cross-section of the taper section. Once the dimensions of the taper are optimized, the fundamental TE and TM modes in the shallow-etched waveguide section could propagate through the taper with high transmission and low mode conversion.

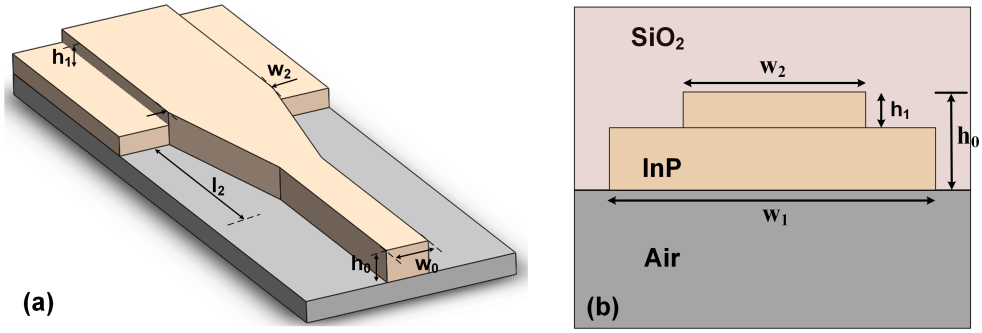

Figure 6.9: (a) the schematic of the bi-level taper. (b) the cross-section in the taper section (at the shallow waveguide side).

Fig 6.9(a) shows the schematic of the butt-jointed taper. Compared to the bi-level taper, this taper design is expected to be more tolerant to fabrication imperfections

because the transition taper is defined together with the deep-etched waveguide. The performance of the taper is mainly determined by the width w_2 and length l_2 of the taper. Fig 6.9(b) shows the cross-section of the transition taper.

6.3.2 Simulation

The performance of the two taper designs is analyzed using the EME method. For the bi-level taper, the width and height of the shallow/deep-etched waveguides are fixed. The width of the taper w_2 is swept from 0.6 μm to 1.0 μm, in steps of 0.1 μm. The length of the taper l_1 is swept from 0 to 500 μm.

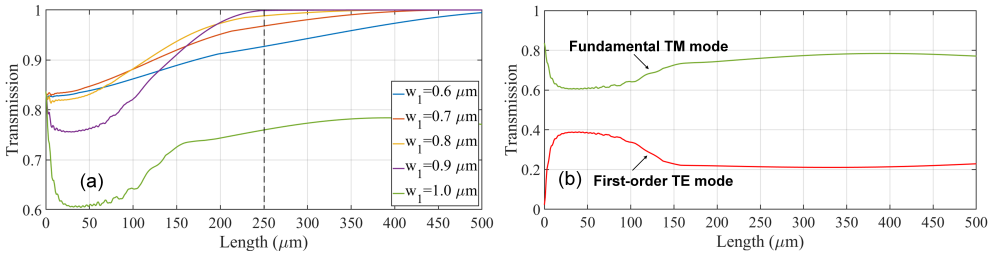

Figure 6.10: Simulation results of the bi-level taper. (a) Transmission of the fundamental TM mode. (b) Transmission of the fundamental TM mode and the first-order TE mode when w_1 is 1.0 μm.

Fig 6.10(a) shows the transmission of the bi-level taper for the fundamental TM mode input at 1550 nm. When the width of w_1 is 1.0 μm, the transition for the fundamental TM mode input is the lowest among all the five different widths. Fig 6.10(b) shows the transmission of the fundamental TM mode and the first-order TE mode for the fundamental TM mode input, when w_1 is 1.0 μm.

About 22% mode conversion can be observed between the two modes when the length of the taper is 250 μm. The adiabatic propagation can no longer be maintained because of the large angle of the taper [109]. For a shallow-to-deep etch transition taper, mode conversion should be avoided. As shown in Fig 6.10(a), When w_1 is 0.9 μm and l_1 is over 250 μm, the transmission for the fundamental TM mode is more than 0.99. For the fundamental TE mode input, a transmission of more than 0.99 is also obtained when w_1 is 0.9 μm and l_1 is over 250 μm in simulation.

Fig 6.11(a) and Fig 6.11(b) show the transmission of the butt-jointed taper for both fundamental TM and TE mode injections at 1550 nm. For the fundamental TM mode input, more than 0.99 transmission can be obtained when w_2 is around 1.1 μm and l_2 is over 90 μm. For the fundamental TM mode input, w_2 is not critical compared to TM_0 mode input. More than 0.99 transmission can be found when w_2 is over 0.9 μm and l_2 is over 70 μm. For the butt-jointed taper design, the transmission for both fundamental TM and TE mode changes within 0.06 when w_2 is swept from 0.8 μm to 1.2 μm. This design therefore seems to be more tolerant to fabrication imperfections in terms of width variation, compared to the bi-level design.

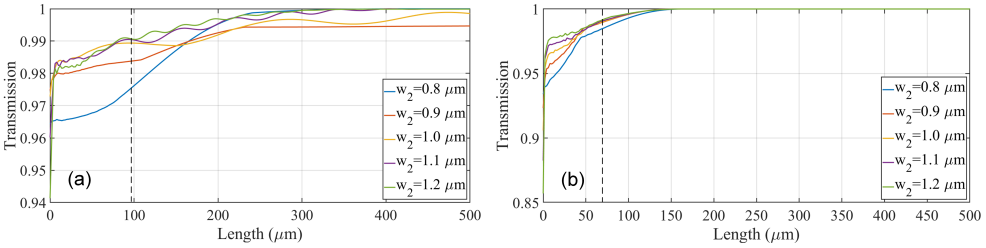

Figure 6.11: Simulation results of the butt-jointed taper. (a) Transmission of the fundamental TM mode. (b) Transmission of the fundamental TE mode.

6.3.3 Fabrication

The two proposed structures are compatible with the IMOS platform. Since the shallow waveguide etch depth is chosen to be the same as the etch depth of the grating couplers (120 nm), no additional process step is needed. Compared to the bi-level design, the butt-jointed taper design is more tolerant to fabrication imperfections in terms of width variation according to the simulation results in Fig 6.10 and Fig 6.11.

Fig 6.12 shows the SEM images of the two designed tapers after the definition of the shallow-etch waveguides. A 50 nm thick SiN layer is covering the top of the waveguide as a hard mask.

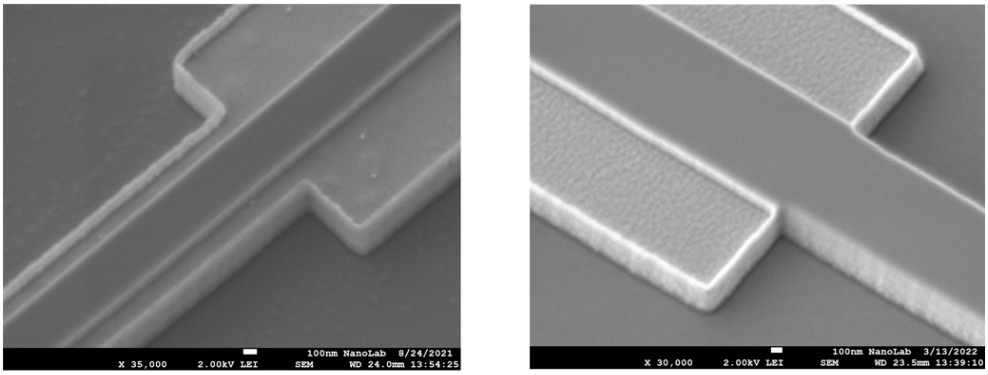

(a) The bi-level taper (b) The butt-jointed taper

Figure 6.12: SEM images of (a) the bi-level taper. (b) the butt-jointed taper.

Unfortunately, these designs cannot be characterized due to aforementioned fabrication failure.

6.4 Bandwidth improvement

In Chapter 5, it is obtained that the FSR of the device is about 2.3 nm. The measured 20 dB optical isolation bandwidth for the two polarization states is 0.2 nm. In the design, the two arms of the MZI have the same length. However, there is always a TE mode in one arm and a TM mode in the other arm, regardless of whether the input is the TE or TM mode. The different propagation constants of the two modes result in an imbalance of the MZI. For practical application purposes, a larger bandwidth is needed.

In the forward direction, the phase shift in the upper arm and the lower arm can be expressed as following if a TE mode light is injected:

$$\phi_{\text{up}} = \beta_{\text{TM},1} \cdot L_1 + \beta_{\text{TM},2} \cdot L_2 + \beta_{\text{TE},1} \cdot L_3 \tag{6.2}$$

$$\phi_{\text{down}} = \beta_{\text{TE},1} \cdot L_1 + \beta_{\text{TE},2} \cdot L_2 + \beta_{\text{TM},1} \cdot L_3 \tag{6.3}$$

where L_1 is the length of the waveguide without coated Ce:YIG between two PCs in the upper arm. L_2 is the length of the waveguide with coated Ce:YIG between two PCs in the upper arm. L_3 is the length of the waveguide between two PCs in the lower arm.

The expected phase difference between two arms can be expressed as:

$$\Delta\phi = (\beta_{\text{TM},1} - \beta_{\text{TE},1}) \cdot (L_1 - L_3) + (\beta_{\text{TM},2} - \beta_{\text{TE},2}) \cdot L_2 \tag{6.4}$$

The effective refractive indices of the two modes in the waveguides with and without Ce:YIG are obtained from a mode solver:

$$\Delta n_{\text{eff},1} = |n_{\text{TE},1} - n_{\text{TM},1}| = 0.22 \tag{6.5}$$

$$\Delta n_{\text{eff},2} = |n_{\text{TE},2} - n_{\text{TM},2}| = 0.16 \tag{6.6}$$

Hence, the phase difference $\Delta\phi$ can be expressed as:

$$\Delta\phi = (\beta_{\text{TM},1} - \beta_{\text{TE},1}) \cdot (L_1 + 0.73L_2 - L_3) \tag{6.7}$$

Light in the two arms becomes in-phase at the output port if $\Delta\phi = 2n\pi$ (n is an integer). In order to increase the optical isolation bandwidth , the integer n should be as small as possible. Therefore, the bandwidth can be improved by either reducing L_1 and L_2 or increasing L_3. In the design in Chapter 5, L_1 is 1.8 mm, L_2 is 4 mm and L_3 is 20 μm. This results in a large imbalance of the MZI, and hence a narrow isolation bandwidth.

As is shown in Fig 6.13, two optical delay lines are implemented in the two arms in order to increase L_3. In the meanwhile, as discussed in Subsection 6.2, thermal-optic phase shifters can be fabricated by patterning metal layers above the InP waveguides. An integrated electromagnet and shallow-to-deep waveguide transitions, discussed in Subsection 6.1 and 6.3, are also integrated in the device.

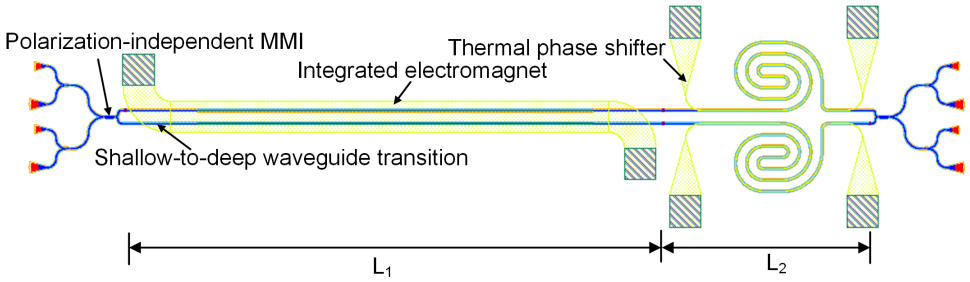

Figure 6.13: Schematic of the nonreciprocal device integrated with a electromagnet, phase shifters, and shallow-to-deep waveguide transitions.

6.5 Integrating isolators with lasers

In Chapter 4 and 5, we have demonstrated integrated optical isolators and circulators, which can be integrated with the fully passive building block library, in the passive IMOS platform. However, an integrated optical isolator becomes more useful when it is integrated with a laser.

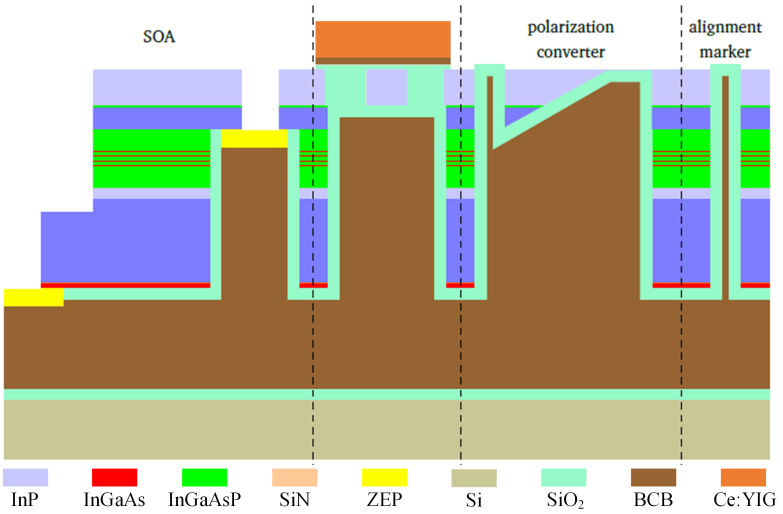

Figure 6.14: Cross-section of the active-passive integrated platform.

The integration of a PC in the twin-guide active-passive IMOS platform has been demonstrated in [27]. The cross section of the active-passive integrated platform is shown in Fig 6.14. All the active and passive components are fabricated in the InP membrane, which is adhesively bonded with a Si wafer. A Ce:YIG-die-to-InP-membrane adhesive bonding procedure is carried out to bond the Ce:YIG die on the InP waveguide. In this way, the co-integration of a nonreciprocal device with a laser is achieved.

Compared with the PC in the passive IMOS platform, the top part of the triangular sections of this PC is a n-doped InP layer instead of an intrinsic InP layer. This n-doped top layer has negligible impact on the PCE and insertion loss of the PC. Details about the performance of the active devices and the integration of the PCs with lasers can be found in [27].

The optical isolator in Chapter 5 can also be fabricated in the twin-guide active-passive IMOS platform. Thus, the isolator can be integrated together with the laser in this paltform.

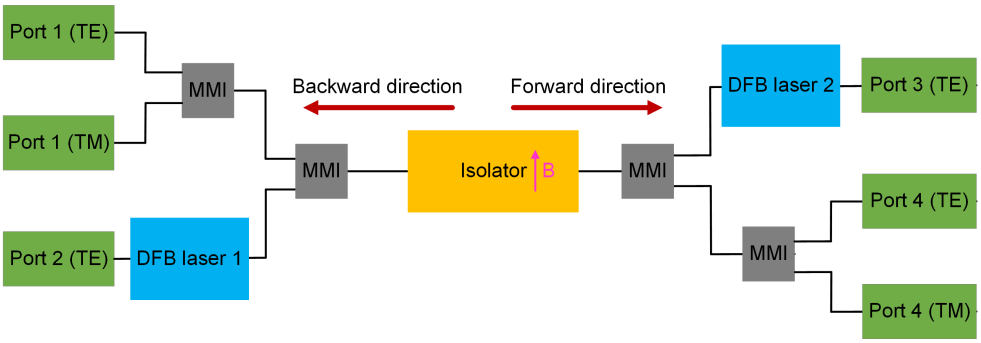

Figure 6.15: Schematic of the characterization structure of the isolators integrated with lasers.

It is also important to characterize the performance of the isolator once it is integrated with the laser. The characterization structure is shown in Fig 6.15. The two DFB lasers are identical and are placed on both sides of the structure to provide TE modes in two different propagation directions.

In the forward direction, the performance of DFB laser 1 can be recorded at port 2. The optical signal propagates through the isolator and is recorded by the two grating couplers at port 4. In the backward direction, the performance of DFB laser 2 is recorded at port 3. The optical signal propagates through the isolator is obtained from the two grating couplers at port 1. The optical isolation and bandwidth of the isolator can be calculated by comparing the transmission spectra at port 1 and port 4.

6.6 Summary

In this chapter, several designs and methods for achieving a broadband, tunable, low-loss and compact nonreciprocal device have been proposed. An integrated electromagnet is designed and fabricated in the IMOS platform. The electromagnet can

replace the bulk permanent magnet to saturate the Ce:YIG film. A thermal-optic phase shifter is proposed in the device to eliminate the phase error between the two arms and tune the operation wavelength. The metal layer of the phase shifter can be patterned in the same lithography cycle as for the electromagnet. Two shallow-to-deep transition tapers are designed. Over 99% transmission is obtained in an EME solver. The transition tapers are compatible with the IMOS process flow. They can be patterned in the same lithography cycle as the grating couplers. The optical isolation bandwidth of the device can be improved by implemented two optical delay lines in the two arms. The estimated bandwidth is over tens of nanometers. A method to integrate the optical nonreciprocal devices with active devices in the IMOS platform is proposed.

With all these optimizations and improvements, the performance of the nonreciprocal devices can be reduced dramatically. This integrated optical isolator is possible to achieve over 30 dB optical isolation and over 30 nm bandwidth, which is comparable with the commercial bulk isolators. The device is also promising to integrate with lasers in the IMOS platform. Therefore, this device shows the potential to meet the requirements for practical applications in a circuit level.

Chapter 7

Conclusions and outlook

7.1 Conclusions

The IMOS platform is promising for the next-generation photonic integrated circuit (pic), providing compact footprint and low power consumption. Multiple functionalities, like light generation, amplification, modulation and detection, have been developed on this platform [110]. However, optical isolation and circulation are still absent. This absence becomes a bottleneck in achieving a high-density functional PIC, and in reaching certain application areas.

Currently, bulk optical isolators and circulators are equipped with lasers and other optical components in module level, which results in a significant proportion of packaging cost. The operation principles of these devices are explained in Chapter 1. The key to achieve optical isolation is to break the Lorentz reciprocity. However, due to the reciprocal nature of most semiconductor and dielectric materials, the integration of optical nonreciprocal devices with other integrated optical components presents crucial design and fabrication challenges.

To bring isolators and circulators on chip, an intuitive way is to copy the design of the bulk devices. However, the Faraday rotation is of limited use due to the beating effect of the two polarization states in the waveguide. Other methods, such as nonreciprocal loss (NRL) and nonreciprocal phase shift (NRPS), are studied and discussed in Chapter 2. Among all these methods, NRPS is preferred, considering the feasibility of the fabrication process and the device performance.

To develop integrated isolators and circulators based on NRPS, a magneto-optic (MO) material named Cerium substituted Yttrium Iron Garnet (Ce:YIG) is chosen. It has a large Faraday rotation coefficient and low optical absorption loss in the near infrared wavelength region. The propagation constants of the light in the Ce:YIG layer, in forward and backward propagation directions, are different if a static magnetic field is transverse to the propagation direction of light. This difference is related to the Faraday rotation coefficient of the Ce:YIG. Mainly three approaches are developed to integrate Ce:YIG with semiconductor platforms: i) Pulsed laser deposition (PLD), ii) Direct bonding and iii) Adhesive bonding. Among them, the last approach is the

most suitable for the IMOS platform.

Wafer bonding techniques have been developed for decades, particularly in the area of integrating light sources on the SOI platform. A heterogeneous integration technique for the integrated optical isolators and circulators on the IMOS platform is demonstrated in Chapter 3. A Ce:YIG-die-to-InP-membrane adhesive bonding procedure is developed. An ultra-thin BCB bonding layer is created to adhesively bond multiple Ce:YIG dies to the InP membrane. The measured thickness of the bonding layer is sufficient for evanescent-coupling. This bonding technique also offers the potential of bonding other functional materials on the InP membrane platform. The bonding yield can be improved by developing a machine-based process, thus avoiding particles, which are created by human interaction.

Two NRPS-based integrated nonreciprocal devices, by using the adhesive bonding technique, are demonstrated in Chapter 4 and Chapter 5, respectively. In Chapter 4, an integrated optical isolator, containing two TE-pass polarizers and a nonreciprocal polarization converter, is proposed. The nonreciprocal polarization converter contains two asymmetric waveguide sections (triangular waveguides) as partial polarization converter and a rectangular waveguide section, on which a Ce:YIG layer is adhesively bonded. The nonreciprocal polarization converter can achieve full TE to TM conversion in one direction and zero conversion in the opposite direction. In combination with polarization filters, an integrated isolator can be obtained. This device is fabricated in the IMOS platform. A 4 mm × 4 mm Ce:YIG die is adhesively bonded on the InP waveguide. A maximum nonreciprocal PCE of 9.8% and 12.6 dB nonreciprocal transmission difference for the TE mode are measured. The performance of this device can be further improved by optimizing design and the bonding process.

To realize a fully integrated isolator using this nonreciprocal polarization converter, two different TE-pass polarizer designs are proposed and simulated. The devices show small footprint, large bandwidth, low insertion loss and high PER in simulation. The proposed polarizers are compatible with the IMOS platform and can be fabricated together with the nonreciprocal polarization converter.

In Chapter 5, an integrated optical nonreciprocal device, which can be operated as an isolator and a circulator, is experimentally demonstrated. NRPS is exploited in a MZI to achive optical isolation and circulation. A Ce:YIG die is adhesively bonded on a MZI, in combination with four PCs. The device shows maximum optical isolations of 27.0 dB and 34.0 dB for TE and TM mode input, respectively. The structure can also function as an optical circulator when using all the four input/output port combinations. For TE polarized light, 27.0 dB and 24.1 dB optical isolations are obtained for the cross-port pairs in that case, while 19.9 dB and 18.6 dB optical isolations are measured for the bar-port pairs. For TM mode light, 30.9 dB and 34.0 dB optical isolations for the cross-port pairs, and 16.8 dB and 16.4 dB optical isolations for the bar-port pairs, are obtained. The demonstration of this nonreciprocal device, which can work for the two hybrid modes, is a first to the best of our knowledge.

To bring this nonreciprocal device to a circuit level, several new building blocks and methods have been proposed and discussed. An integrated electromagnet is designed and fabricated on top of the InP waveguide in the IMOS platform. The electromagnet can replace the bulky permanent magnet to provide a sufficient magnetic field. A thermal phase shifter is implemented in the device to tune the operation

wavelength and meet the optimal phase condition. The metal layer of the phase shifter can be patterned in the same lithography cycle as for the electromagnet. In order to reduce the waveguide loss and create a flat surface for Ce:YIG bonding, two shallow-to-deep transition tapers are designed. The transition tapers are compatible with the IMOS process flow. They can be patterned in the same lithography cycle as for the grating couplers. The optical isolation bandwidth of the device can be improved by implemented two optical delay lines in the two branches. The estimated bandwidth is over tens of nanometers, comparable with the bandwidth of a bulk optical isolator.

This device is demonstrated on a platform that has been shown to integrate active and passive photonic components, including amplifiers and lasers, on one platform. A method to integrate the optical nonreciprocal devices with active devices in the IMOS platform is also proposed. With all these optimizations and improvements, the footprint and the insertion loss of the device can be reduced dramatically. The obtainable bandwidth and isolation are comparable with commercial bulk isolators. Therefore, this device shows the potential to meet the requirements for practical applications. It also provides a step forward towards multi-functional and high-density PICs.

7.2 Outlook

In this thesis, the successful demonstration of integrated optical isolators and circulators in the IMOS platform is reported. Nevertheless, several future improvements need to be made to meet the requirements of real world applications. Hence, some suggestions for this are made in this section.

1. Reducing the device footprint

In order to obtain large optical isolation and circulation, the device in this thesis is bonded with a 4×4 mm^2 Ce:YIG die, which significantly increases the footprint of the device. In this section, two methods are proposed to reduce the device footprint while maintaining its performance.

- Reducing the bonding layer thickness

  For the work in this thesis, a 3-inch Ce:YIG on SGGG wafer is diced into plenty of dies, which are adhesively bonded on the InP waveguides. In Chapter 3, it is found that the NRPS increases with reduced bonding layer thickness. At most a 72 nm thick BCB layer is needed to reach π NRPS for Ce:YIG with 4 mm length.

  In order to reduce the Ce:YIG size, further efforts need to be done to reach a thinner BCB layer. As is discussed in Chapter 3, a thinner BCB layer has less tolerant to surface topology and particle contamination. A clean, smooth and flat surface is required in order to improve the bonding yield. Furthermore, the uniformity of the bonding layer needs to be investigated.

  Alternatively, a plasma-assisted direct bonding process can be developed [111]. It has been found that exposing Ce:YIG and semiconductors in oxygen plasma

can smooth the surface in order to increase the adhesion. In this way, the bonding layer can be thinned down to an atomic layer, and therefore the size of the Ce:YIG die can be reduced according to the simulation results in Chapter 3. However, this technique requires an extreme flat and clean surface. Such strict requirements may bring challenges to an large-scale fabrication in the future.

- Patterning the Ce:YIG film

  The schematic is of the design in this thesis is shown in Fig 7.1(a). In this design. the coupling efficiency of light in this structure depends on the waveguide dimension and the thickness of the bonding layer between Ce:YIG and waveguide. As is analyzed in Chapter 3, the mode coupling efficiency reduces with reduced bonding layer thickness, because of the mode mismatch at the interface between the plain waveguide and the Ce:YIG-covered waveguide.

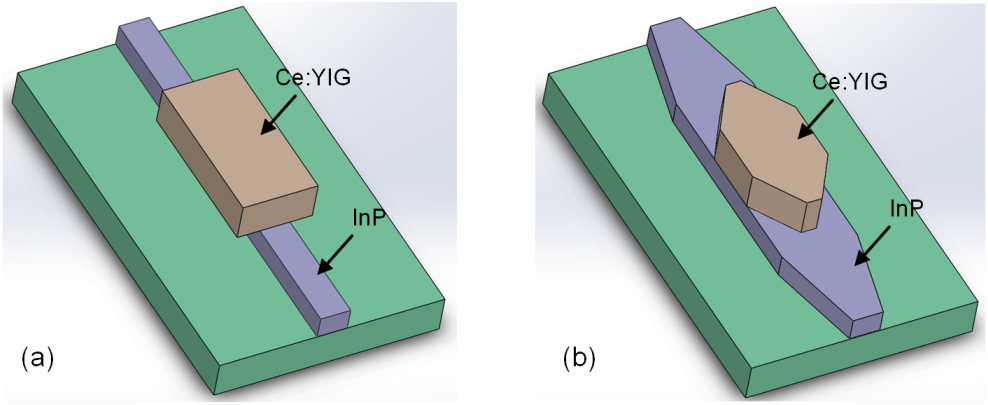

Figure 7.1: Schematics of two coupling structures. (a) Conventional structure. (b) Tapered structure.

  In order to increase the coupling efficiency of the optical mode in the Ce:YIG layer, an adiabatic taper is designed, as shown in Fig 7.1(b). At the adiabatic coupling region, the optical mode can first be coupled into the Ce:YIG layer, and experience a NRPS. Then, the optical mode is confined into InP waveguide again when the width of Ce:YIG gradually decreases. Other designs, such as multiple stages of linear adiabatic tapers [112], can also be used to further increase the coupling efficiency.

  Therefore, the key is to pattern the Ce:YIG layer into the designed shape after the bonding process. In 2020, an ion mill etching technique is developed to etch YIG film [113]. An etch rate of 32.6 nm/min is achieved. A vertical sidewall angle is retained in this process. It is also found that the thickness of the YIG film is reduced from 2 μm to 300 nm by wet etching in ortho-phosphoric acid for about an hour [114]. It is also possible to develop dry-etch and wet-etch processes to pattern the YIG film.

2. Scaling up the bonding process

In order to achieve large-scale integration in the future, the throughput and the yield of the Ce:YIG-die-to-IMOS-wafer bonding process, developed in Chapter 3, needs to be improved.

High-throughput multiple dies-to-wafer bonding techniques have been developed in order to integrate lasers on a Si substrate [112, 115]. An automatic pick-and-place method is developed to avoid bonding surface contamination, and therefore the bonding yield can be improved. Figure 7.2(a) shows a photograph of a processed 8-inch Si wafer bonded with 100 InP dies (5 mm × 5 mm). The achieved bonding yield is about 80%. Fig 7.2(b) shows a zoom-in view of the wafer center region.

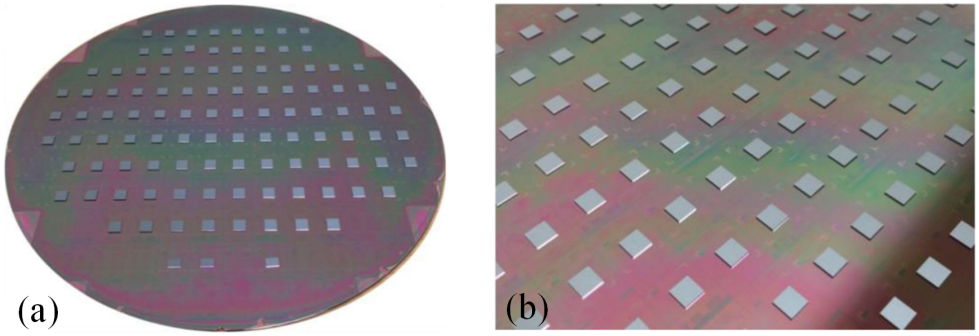

Figure 7.2: (a) Photograph of a processed 8-inch Si wafer bonded with 100 InP dies. (b) Zoom-in image of the bonded dies.

This bonding technique is also suitable for bonding multiple Ce:YIG dies on the InP membrane. Further experiments, such as to investigate the uniformity and the tensile stress of the bonding layer, still need to be considered.

Appendix A

Inventory of Ce:YIG samples

The Ce:YIG dies used in this thesis are provided by Professor Yuya Shoji and Professor Tetsuya Mizumoto from the Tokyo Institute of Technology. The Ce:YIG film is deposited on a 3 inch (111)-oriented SGGG substrate, which is purchased from Saint-Gobain Crystals, France. The two quarters are diced into dies with different dimensions, as shown in Fig A.1.

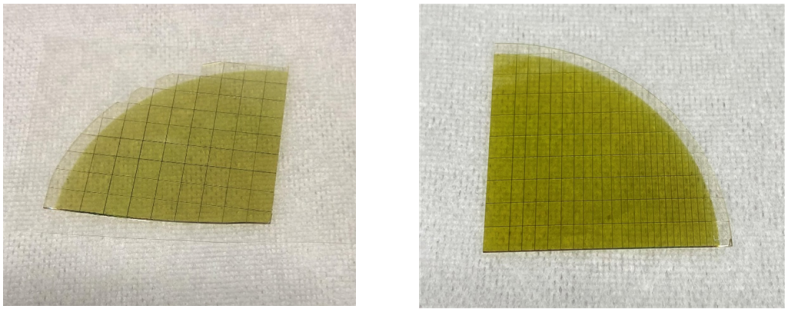

Figure A.1: Images of two diced Ce:YIG/SGGG quarters.

An inventory of Ce:YIG dies is listed in Table A.1. In chapter 3, Ce:YIG dies with different dimensions are used to perform the multiple-Ce:YIG-die-to-InP-membrane bonding test. In chapter 4 and 5, only 4 mm × 4 mm Ce:YIG dies are used for the characterization of the nonreciprocal devices.

Size	Amount
4 mm × 4 mm	60
4 mm × 2 mm	40
4 mm × 1.5 mm	35
4 mm × 1 mm	60

Table A.1: The inventory of Ce:YIG.

Appendix B

Theoretical analysis of the nonreciprocal device

In Section 5.2, Chapter 5, the theoretical analysis of the nonreciprocal device is based on several ideal conditions, where the PCE of the PC is exactly 100%, the splitting ratio is 50:50 for the TE and TM modes, and the phase difference is zero in one direction and π in another direction.

However, it is much more difficult to meet all these conditions due to fabrication imperfections. Hence, it is important to know how these components affect the performance of the nonreciprocal device. In this section, Jones vectors and matrices are used to explain the working principle of the device.

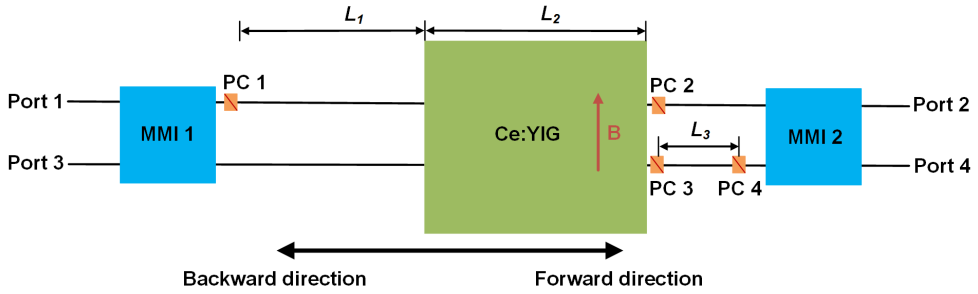

Figure B.1: Schematic diagram of the device.

In the forward direction, the input signal can be written as a four-element vector:

$$S_{in} = \begin{bmatrix} TE_{\text{upper}} \\ TE_{\text{lower}} \\ TM_{\text{upper}} \\ TM_{\text{lower}} \end{bmatrix} \tag{B.1}$$

The transfer matrix of the first 2×2 MMI:

$$T_{MMI,1} = \begin{bmatrix} \sqrt{k_{\mathrm{TE}}} & j\sqrt{1-k_{\mathrm{TE}}} & 0 & 0 \\ j\sqrt{1-k_{\mathrm{TE}}} & \sqrt{k_{\mathrm{TE}}} & 0 & 0 \\ 0 & 0 & \sqrt{k_{\mathrm{TM}}} & j\sqrt{1-k_{\mathrm{TM}}} \\ 0 & 0 & j\sqrt{1-k_{\mathrm{TM}}} & \sqrt{k_{\mathrm{TM}}} \end{bmatrix} \tag{B.2}$$

where k_{TE} and k_{TM} are the coupling constants of the first MMI for the respective polarizations. In this design, $\mathrm{T_{MMI,1}}=\mathrm{T_{MMI,2}}$, since the two MMIs are assumed symmetrical.

The transfer matrix of the two PCs in the up branch can be written as:

$$T_{\mathrm{PC,up}} = \begin{bmatrix} \sqrt{1-\eta} & 0 & j\sqrt{\eta} & 0 \\ 0 & 1 & 0 & 0 \\ j\sqrt{\eta} & 0 & \sqrt{1-\eta} & 0 \\ 0 & 0 & 0 & 1 \end{bmatrix} \tag{B.3}$$

where η is the PCE of the PC. PC3 and PC4 are ignored in order to simplify the calculation.

For the waveguide section without Ce:YIG, the transfer matrix can be written as:

$$T_{\mathrm{WG}} = \begin{bmatrix} e^{j\beta_{\mathrm{TE}}L_1} & 0 & 0 & 0 \\ 0 & e^{j\beta_{\mathrm{TE}}L_1} & 0 & 0 \\ 0 & 0 & e^{j\beta_{\mathrm{TM}}L_1} & 0 \\ 0 & 0 & 0 & e^{j\beta_{\mathrm{TM}}L_1} \end{bmatrix} \tag{B.4}$$

where β_{TE} and β_{TM} are the propagation constants in the waveguide section without Ce:YIG.

For the waveguide coated with the Ce:YIG layer, the transfer matrix in the forward direction can be written as:

$$T_{\mathrm{YIG,F}} = \begin{bmatrix} e^{j\beta_{\mathrm{TE,YIG}}L_2} & 0 & 0 & 0 \\ 0 & e^{j\beta_{\mathrm{TE,YIG}}L_2} & 0 & 0 \\ 0 & 0 & e^{j\beta_{\mathrm{TM,F}}L_2} & 0 \\ 0 & 0 & 0 & e^{j\beta_{\mathrm{TM,F}}L_2} \end{bmatrix} \tag{B.5}$$

where $\beta_{\mathrm{TE,YIG}}$ and $\beta_{\mathrm{TM,F}}$ are the propagation constants in the waveguide section with Ce:YIG.

The output vector can be expressed as:

$$S_{\mathrm{out}} = T_{\mathrm{MMI,2}} \cdot T_{\mathrm{PC,up}} \cdot T_{\mathrm{YIG,F}} \cdot T_{\mathrm{WG}} \cdot T_{\mathrm{PC,up}} \cdot T_{\mathrm{MMI,1}} \cdot S_{\mathrm{in}} \tag{B.6}$$

If the TE mode is input from port 1, the output vector becomes:

$$S_{\text{out}} = \begin{bmatrix} (1-\eta)k_{\text{TE}}e^{j\phi_{\text{TE}}} - \eta k_{\text{TE}}e^{j\phi_{\text{TM}}} - (1-k_{\text{TE}})e^{j\phi_{\text{TE}}} \\ j(1-\eta)\sqrt{k_{\text{TE}}}\sqrt{1-k_{\text{TE}}}e^{j\phi_{\text{TE}}} - j\eta\sqrt{k_{\text{TE}}}\sqrt{1-k_{\text{TE}}}e^{j\phi_{\text{TM}}} + j\sqrt{k_{\text{TE}}}\sqrt{1-k_{\text{TE}}}e^{j\phi_{\text{TE}}} \\ j\sqrt{\eta}\sqrt{1-\eta}\sqrt{k_{\text{TE}}}\sqrt{k_{\text{TM}}}(e^{j\phi_{\text{TE}}} + e^{j\phi_{\text{TM}}}) \\ -\sqrt{\eta}\sqrt{1-\eta}\sqrt{k_{\text{TE}}}\sqrt{1-k_{\text{TM}}}(e^{j\phi_{\text{TE}}} + e^{j\phi_{\text{TM}}}) \end{bmatrix} \tag{B.7}$$

where $\phi_{\text{TE}} = \beta_{\text{TE}}L_1 + \beta_{\text{TE,YIG}}L_2$, $\phi_{\text{TM}} = \beta_{\text{TM}}L_1 + \beta_{\text{TM,F}}L_2$.

Clearly, the power of the TM mode at the two output ports is zero if the PCE of the PC is 1. For a lower PCE, the TM mode will be coupled out at the two ports. The power of the TE mode at the two output ports also depends on the splitting ratio of the MMI and the phase shift of the two modes.

The extinction ratio (ER) at the two output ports can be expressed as:

$$\text{ER} = 10\log_{10}\left(\frac{P_{\text{out,up}}}{P_{\text{out,bot}}}\right) \tag{B.8}$$

According to Eq. (A.7), η and k_{TE} will both affect the ER of the device. As a result, the optical isolation of the device is influenced.

Bibliography

[1] B. Roel, *Photonics*, 8th ed. Ghent University, 2019.

[2] T. T. M. van Schaijk, "Feedback Insensitive Integrated Semiconductor Laser," Ph.D. dissertation, Eindhoven University of Technology, Eindhoven, 2019.

[3] R. Lang and K. Kobayashi, "External optical feedback effects on semiconductor injection laser properties," *IEEE Journal of Quantum Electronics*, vol. 16, no. 3, pp. 347–355, Mar. 1980.

[4] A. Y. Liu, T. Komljenovic, M. L. Davenport, A. C. Gossard, and J. E. Bowers, "Reflection sensitivity of 13 um quantum dot lasers epitaxially grown on silicon," *Optics Express*, vol. 25, no. 9, p. 9535, May 2017.

[5] O. Hirota and Y. Suematsu, "Noise properties of injection lasers due to reflected waves," *IEEE Journal of Quantum Electronics*, vol. 15, no. 3, pp. 142–149, Mar. 1979.

[6] L. Goldberg, H. Taylor, A. Dandridge, J. Weller, and R. Miles, "Spectral Characteristics of Semiconductor Lasers with Optical Feedback," *IEEE Transactions on Microwave Theory and Techniques*, vol. 30, no. 4, pp. 401–410, 1982.

[7] K. Petermann, "External optical feedback phenomena in semiconductor lasers," *IEEE Journal of Selected Topics in Quantum Electronics*, vol. 1, no. 2, pp. 480–489, Jun. 1995.

[8] D. Jalas, A. Petrov, M. Eich, W. Freude, S. Fan, Z. Yu, R. Baets, M. Popović, A. Melloni, J. D. Joannopoulos, M. Vanwolleghem, C. R. Doerr, and H. Renner, "What is — and what is not — an optical isolator," *Nature Photonics*, vol. 7, no. 8, pp. 579–582, Aug. 2013.

[9] D. Lenstra, T. T. M. van Schaijk, and K. A. Williams, "Toward a Feedback-Insensitive Semiconductor Laser," *IEEE Journal of Selected Topics in Quantum Electronics*, vol. 25, no. 6, pp. 1–13, Nov. 2019.

[10] J. Duan, H. Huang, B. Dong, D. Jung, J. C. Norman, J. E. Bowers, and F. Grillot, "1.3- um Reflection Insensitive InAs/GaAs Quantum Dot Lasers Directly Grown on Silicon," *IEEE Photonics Technology Letters*, vol. 31, no. 5, pp. 345–348, Mar. 2019.

[11] D. Dai, J. Bauters, and J. E. Bowers, "Passive technologies for future large-scale photonic integrated circuits on silicon: Polarization handling, light non-reciprocity and loss reduction," *Light: Science & Applications*, vol. 1, no. 3, pp. e1–e1, Mar. 2012.

[12] D. Vojna, O. Slezák, A. Lucianetti, and T. Mocek, "Verdet Constant of Magneto-Active Materials Developed for High-Power Faraday Devices," *Applied Sciences*, vol. 9, no. 15, p. 3160, Aug. 2019.

[13] H. Taskeya, "A Review of Magneto-Optic Effects and Its Application," *International Journal of Electromagnetics and Applications*, p. 8, 2017.

[14] J. Yang, Y. Xu, F. Zhang, and M. Guillot, "Theoretical analysis of the magnetization and of the paramagnetic and diamagnetic magneto-optical effects in Pr-substituted yttrium iron garnets using quantum theory," *Physical Review B*, vol. 56, no. 17, pp. 11 119–11 133, Nov. 1997.

[15] "Thor labs-optical isolators," https://www.thorlabs.com/newgrouppage9.cfm?objectgroup_id=6178.

[16] "Thor labs-optical circulators," https://www.thorlabs.com/newgrouppage9.cfm?objectgroup_id=373.

[17] T. R. Zaman, X. Guo, and R. J. Ram, "Semiconductor Waveguide Isolators," *Journal of Lightwave Technology*, vol. 26, no. 2, pp. 291–301, 2008.

[18] D. Huang, P. Pintus, and J. E. Bowers, "Towards heterogeneous integration of optical isolators and circulators with lasers on silicon [Invited]," *Optical Materials Express*, vol. 8, no. 9, p. 2471, Sep. 2018.

[19] M. Krause, H. Renner, and E. Brinkmeyer, "Optical isolation in silicon waveguides based on nonreciprocal Raman amplification," *Electronics Letters*, vol. 44, no. 11, p. 691, 2008.

[20] C.-H. Dong, Z. Shen, C.-L. Zou, Y.-L. Zhang, W. Fu, and G.-C. Guo, "Brillouin-scattering-induced transparency and non-reciprocal light storage," *Nature Communications*, vol. 6, no. 1, p. 6193, May 2015.

[21] S. Hua, J. Wen, X. Jiang, Q. Hua, L. Jiang, and M. Xiao, "Demonstration of a chip-based optical isolator with parametric amplification," *Nature Communications*, vol. 7, no. 1, p. 13657, Dec. 2016.

[22] J. B. Khurgin, "Non-reciprocal propagation versus non-reciprocal control," *Nature Photonics*, vol. 14, no. 12, pp. 711–711, Dec. 2020.

[23] H. Lira, Z. Yu, S. Fan, and M. Lipson, "Electrically Driven Nonreciprocity Induced by Interband Photonic Transition on a Silicon Chip," *Physical Review Letters*, vol. 109, no. 3, pp. 1–5, Jul. 2012.

[24] D. B. Sohn, S. Kim, and G. Bahl, "Time-reversal symmetry breaking with acoustic pumping of nanophotonic circuits," *Nature Photonics*, vol. 12, no. 2, pp. 91–97, Feb. 2018.

[25] C. R. Doerr, N. Dupuis, and L. Zhang, "Optical isolator using two tandem phase modulators," *Optics Letters*, vol. 36, no. 21, p. 4293, Nov. 2011.

[26] W. Yan, Y. Yang, W. Yang, J. Qin, L. Deng, and L. Bi, "On-Chip Nonreciprocal Photonic Devices Based on Hybrid Integration of Magneto-Optical Garnet Thin Films on Silicon," *IEEE Journal of Selected Topics in Quantum Electronics*, vol. 28, no. 3, pp. 1–15, May 2022.

[27] S. F. G. Reniers, "Integration of a polarization converter on the active-passive IMOS platform," Ph.D. dissertation, Eindhoven University of Technology, Eindhoven, 2022.

[28] M. Smit, X. Leijtens, B. Musk, and D. Robbins, "An introduction to InP-based generic integration technology," *Semiconductor Science and Technology*, vol. 29, no. 8, pp. 1–41, Jun. 2014.

[29] L. Shen, "Double-side processing for membrane-based photonic integration," in *The European Conference on Integrated Optics*, 2016.

[30] W. Yao, X. Liu, M. K. Matters-Kammerer, A. Meighan, M. Spiegelberg, M. Trajkovic, J. J. G. M. van der Tol, M. J. Wale, X. Zhang, and K. Williams, "Towards the Integration of InP Photonics With Silicon Electronics: Design and Technology Challenges," *Journal of Lightwave Technology*, vol. 39, no. 4, pp. 999–1009, Feb. 2021.

[31] J. van Engelen, S. Reniers, J. Bolk, K. Williams, J. van der Tol, and Y. Jiao, "Low Loss InP Membrane Photonic Integrated Circuits Enabled by 193-nm Deep UV Lithography," in *2019 Compound Semiconductor Week (CSW)*. Nara, Japan: IEEE, May 2019, pp. 1–2.

[32] Y. Jiao, T. de Vries, R.-S. Unger, L. Shen, H. Ambrosius, C. Radu, M. Arens, M. Smit, and J. van der Tol, "Vertical and Smooth Single-Step Reactive Ion Etching Process for InP Membrane Waveguides," *Journal of The Electrochemical Society*, vol. 162, no. 8, pp. E90–E95, 2015.

[33] F. Van Laere, T. Claes, J. Schrauwen, S. Scheerlinck, W. Bogaerts, D. Taillaert, L. O'Faolain, D. Van Thourhout, and R. Baets, "Compact Focusing Grating Couplers for Silicon-on-Insulator Integrated Circuits," *IEEE Photonics Technology Letters*, vol. 19, no. 23, pp. 1919–1921, Dec. 2007.

[34] J. Pello, J. van der Tol, S. Keyvaninia, R. van Veldhoven, H. Ambrosius, G. Roelkens, and M. Smit, "High-efficiency ultrasmall polarization converter in InP membrane," *Optics Letters*, vol. 37, no. 17, p. 3711, Sep. 2012.

[35] V. Pogoretskiy, "Nanophotonic membrane platform for integrated active devices and circuits," Ph.D. dissertation, Eindhoven University of Technology, Eindhoven, 2019.

[36] B. Gargallo, Y. Jiao, P. Muñoz, J. van der Tol, and X. Leijtens, "Simulation and design of arrayed waveguide gratings for InP membranes using an efficient numerical method and improved shallow to deep transitions," *Optical and Quantum Electronics*, vol. 48, no. 7, p. 356, Jul. 2016.

[37] L. Shen, Y. Jiao, W. Yao, Z. Cao, J. P. van Engelen, G. Roelkens, M. K. Smit, and J. J. G. M. van der Tol, "High-bandwidth uni-traveling carrier waveguide photodetector on an InP-membrane-on-silicon platform," *Optics Express*, vol. 24, no. 8, p. 8290, Apr. 2016.

[38] A. Kashi, J. van der Tol, K. Williams, W. Yao, M. S. Lebby, C. Pecinovsky, and Y. Jiao, "Electro-Optic Slot Waveguide Phase Modulator on the InP Membrane on Silicon Platform," *IEEE Journal of Quantum Electronics*, pp. 1–1, 2020.

[39] J. van der Tol, "InP Membrane on Silicon (IMOS) Photonics," *IEEE Journal of Quantum Electronics*, vol. 56, pp. 1–7, 2020.

[40] S. Kumari, "A comprehensive study of magneto-optic materials and its applications," *Materials Today: Proceedings*, vol. 56, pp. 100–106, Jan. 2022.

[41] S. Kumari and S. Chakraborty, "Study of different magneto-optic materials for current sensing applications," *Journal of Sensors and Sensor Systems*, vol. 7, no. 1, pp. 421–431, Jun. 2018.

[42] L. Bi, J. Hu, P. Jiang, H. Kim, D. Kim, M. Onbasli, G. Dionne, and C. Ross, "Magneto-Optical Thin Films for On-Chip Monolithic Integration of Non-Reciprocal Photonic Devices," *Materials*, vol. 6, no. 11, pp. 5094–5117, Nov. 2013.

[43] L. Bi, J. Hu, P. Jiang, D. H. Kim, G. F. Dionne, L. C. Kimerling, and C. A. Ross, "On-chip optical isolation in monolithically integrated non-reciprocal optical resonators," *Nature Photonics*, vol. 5, no. 12, pp. 758–762, Dec. 2011.

[44] T. Goto, Y. Eto, K. Kobayashi, Y. Haga, M. Inoue, and C. A. Ross, "Vacuum annealed cerium-substituted yttrium iron garnet films on non-garnet substrates for integrated optical circuits," *Journal of Applied Physics*, vol. 113, no. 17, p. 17A939, May 2013.

[45] T. Fakhrul, S. Tazlaru, L. Beran, Y. Zhang, M. Veis, and C. A. Ross, "Magneto-Optical Bi:YIG Films with High Figure of Merit for Nonreciprocal Photonics," *Advanced Optical Materials*, vol. 7, no. 13, 2019.

[46] Y. Shoji, M. Yanaga, T. Kashima, T. Suzuki, S. Nakagawa, and T. Mizumoto, "Application of Cobalt Ferrite to an Ultra-Compact Magneto-Optical Isolator on Silicon Photonics Circuits," *Journal of the Japan Society of Powder and Powder Metallurgy*, vol. 61, no. S1, pp. S343–S345, 2014.

[47] M. Yanaga, Y. Shoji, Y. Takamura, S. Nakagawa, and T. Mizumoto, "Compact magnetooptical isolator with cobalt ferrite on silicon photonic circuits," *Applied Physics Express*, vol. 8, no. 8, p. 082201, Aug. 2015.

[48] T. Zaman, X. Guo, and R. J. Ram, "Faraday rotation in semiconductors for photonic integration," in *CLEO 2004*, 2004, p. 2.

[49] M. C. Onbasli, L. Beran, M. Zahradník, M. Kučera, R. Antoš, J. Mistrík, G. F. Dionne, M. Veis, and C. A. Ross, "Optical and magneto-optical behavior of Cerium Yttrium Iron Garnet thin films at wavelengths of 200–1770 nm," *Scientific Reports*, vol. 6, no. 1, p. 23640, Jul. 2016.

[50] J. F. Dillon, "Origin and Uses of the Faraday Rotation in Magnetic Crystals," *Journal of Applied Physics*, vol. 39, no. 2, pp. 922–929, Feb. 1968.

[51] T. R. Zaman, X. Guo, and R. J. Ram, "Faraday rotation in an InP waveguide," *Applied Physics Letters*, vol. 90, no. 2, Jan. 2007.

[52] M. Gomi, K. Satoh, and M. Abe, "Giant Faraday Rotation of Ce-Substituted YIG Films Epitaxially Grown by RF Sputtering," *Japanese Journal of Applied Physics*, vol. 27, no. Part 2, No. 8, pp. L1536–L1538, Aug. 1988.

[53] M. Gomi, H. Furuyama, and M. Abe, "Enhancement of Faraday Effect in Highly Ce-Substituted YIG Epitaxial Films by RF Sputtering," *Japanese Journal of Applied Physics*, vol. 29, no. Part 2, No. 1, pp. L99–L100, Jan. 1990.

[54] M. Huang and S.-Y. Zhang, "Growth and characterization of cerium-substituted yttrium iron garnet single crystals for magneto-optical applications," *Applied Physics A: Materials Science & Processing*, vol. 74, no. 2, pp. 177–180, Feb. 2002.

[55] Y. Shoji, M. Ito, Y. Shirato, and T. Mizumoto, "MZI optical isolator with Si-wire waveguides by surface-activated direct bonding," *Optics Express*, vol. 20, no. 16, p. 18440, Jul. 2012.

[56] S. Ghosh, S. Keyvavinia, W. Van Roy, T. Mizumoto, G. Roelkens, and R. Baets, "Ce:YIG/Silicon-on-Insulator waveguide optical isolator realized by adhesive bonding," *Optics Express*, vol. 20, no. 2, p. 1839, Jan. 2012.

[57] G. Roelkens, J. Van Campenhout, J. Brouckaert, D. Van Thourhout, R. Baets, P. R. Romeo, P. Regreny, A. Kazmierczak, C. Seassal, X. Letartre, G. Hollinger, J. Fedeli, L. Di Cioccio, and C. Lagahe-Blanchard, "III-V/Si photonics by die-to-wafer bonding," *Materials Today*, vol. 10, no. 7-8, pp. 36–43, Jul. 2007.

[58] B. Ren, Y. Hou, and Y. Liang, "Research progress of III–V laser bonding to Si," *Journal of Semiconductors*, vol. 37, no. 12, p. 124001, Dec. 2016.

[59] S. Abadian, "Non-reciprocalwaveguidesbasedonmagnetoplasmonic effects," Ph.D. dissertation, University of Paris-Saclay, Paris, 2021.

[60] F. E. Demirer, Y. Baron, S. Reniers, D. Pustakhod, R. Lavrijsen, J. van der Tol, and B. Koopmans, "An integrated photonic device for on-chip magneto-optical memory reading," *Nanophotonics*, vol. 11, no. 14, pp. 3319–3329, Jun. 2022.

[61] D. C. Hutchings and B. M. Holmes, "A Waveguide Polarization Toolset Design Based on Mode Beating," *IEEE Photonics Journal*, vol. 3, no. 3, pp. 450–461, Jun. 2011.

[62] G. Gabriel and M. Brodwin, "The Solution of Guided Waves in Inhomogeneous Anisotropic Media by Perturbation and Variational Methods," *IEEE Transactions on Microwave Theory and Techniques*, vol. 13, no. 3, pp. 364–370, May 1965.

[63] C. Zhang, P. Dulal, B. J. H. Stadler, and D. C. Hutchings, "Monolithically-Integrated TE-mode 1D Silicon-on-Insulator Isolators using Seedlayer-Free Garnet," *Scientific Reports*, vol. 7, no. 1, p. 5820, Dec. 2017.

[64] R. Wolfe, V. J. Fratello, and M. McGlashan-Powell, "Thin-film garnet materials with zero linear birefringence for magneto-optic waveguide devices (invited)," *Journal of Applied Physics*, vol. 63, no. 8, pp. 3099–3103, Apr. 1988.

[65] D. C. Hutchings, B. M. Holmes, C. Zhang, P. Dulal, A. D. Block, S.-Y. Sung, N. C. A. Seaton, and B. J. H. Stadler, "Quasi-Phase-Matched Faraday Rotation in Semiconductor Waveguides With a Magnetooptic Cladding for Monolithically Integrated Optical Isolators," *IEEE Photonics Journal*, vol. 5, no. 6, pp. 6 602 512–6 602 512, Dec. 2013.

[66] W. Zaets and K. Ando, "Optical waveguide isolator based on nonreciprocal loss/gain of amplifier covered by ferromagnetic layer," *IEEE Photonics Technology Letters*, vol. 11, no. 8, pp. 1012–1014, Aug. 1999.

[67] H. Yokoi, T. Mizumoto, N. Shinjo, N. Futakuchi, and Y. Nakano, "Demonstration of an optical isolator with a semiconductor guiding layer that was obtained by use of a nonreciprocal phase shift," *Applied Optics*, vol. 39, no. 33, p. 6158, Nov. 2000.

[68] S. Yamamoto and T. Makimoto, "Circuit theory for a class of anisotropic and gyrotropic thin-film optical waveguides and design of nonreciprocal devices for integrated optics," *Journal of Applied Physics*, vol. 45, no. 2, pp. 882–888, Feb. 1974.

[69] V. P. Wouter, "Optimization of an Integrated Optical Isolator Based on a Semiconductor Amplifier with a Ferromagnetic Metal Contact," Ph.D. dissertation, Ghent University, Ghent, 2009.

[70] H. Shimizu and Y. Nakano, "First Monolithic Integration of a Waveguide Optical Isolator with a Distributed Feedback Laser Diode," in *2006 IEEE 20th International Semiconductor Laser Conference, 2006. Conference Digest.* Kohala Coast, HI, USA: IEEE, 2006, pp. 17–18.

[71] Y. Shoji, K. Miura, and T. Mizumoto, "Optical nonreciprocal devices based on magneto-optical phase shift in silicon photonics," *Journal of Optics*, vol. 18, no. 1, p. 013001, Jan. 2016.

[72] Y. Shoji and T. Mizumoto, "Magneto-optical non-reciprocal devices in silicon photonics," *Science and Technology of Advanced Materials*, vol. 15, no. 1, p. 014602, Feb. 2014.

[73] Y. Shirato, Y. Shoji, and T. Mizumoto, "Over 20-dB isolation with 8-nm bandwidth in silicon MZI optical isolator," in *10th International Conference on Group IV Photonics*. Seoul, Korea (South): IEEE, Aug. 2013, pp. 136–137.

[74] R. Takei and T. Mizumoto, "Design and Simulation of Silicon Waveguide Optical Circulator Employing Nonreciprocal Phase Shift," *Japanese Journal of Applied Physics*, vol. 49, no. 5, p. 052203, May 2010.

[75] P. Pintus, D. Huang, C. Zhang, Y. Shoji, T. Mizumoto, and J. E. Bowers, "Microring-Based Optical Isolator and Circulator with Integrated Electromagnet for Silicon Photonics," *Journal of Lightwave Technology*, vol. 35, no. 8, pp. 1429–1437, Apr. 2017.

[76] D. Huang, P. Pintus, C. Zhang, P. Morton, Y. Shoji, T. Mizumoto, and J. E. Bowers, "Dynamically reconfigurable integrated optical circulators," *Optica*, vol. 4, no. 1, p. 23, Jan. 2017.

[77] A. R. Adams, "Strained-Layer Quantum-Well Lasers," *IEEE Journal of Selected Topics in Quantum Electronics*, vol. 17, no. 5, pp. 1364–1373, Sep. 2011.

[78] Y. Shoji, A. Fujie, and T. Mizumoto, "Silicon Waveguide Optical Isolator Operating for TE Mode Input Light," *IEEE Journal of Selected Topics in Quantum Electronics*, vol. 22, no. 6, pp. 264–270, Nov. 2016.

[79] Y. Zhang, Q. Du, C. Wang, T. Fakhrul, S. Liu, L. Deng, D. Huang, P. Pintus, J. Bowers, C. A. Ross, J. Hu, and L. Bi, "Monolithic integration of broadband optical isolators for polarization-diverse silicon photonics," *Optica*, vol. 6, no. 4, p. 473, Apr. 2019.

[80] S. Ghosh, S. Keyvaninia, Y. Shirato, T. Mizumoto, G. Roelkens, and R. Baets, "Optical Isolator for TE Polarized Light Realized by Adhesive Bonding of Ce:YIG on Silicon-on-Insulator Waveguide Circuits," *IEEE Photonics Journal*, vol. 5, no. 3, pp. 6 601 108–6 601 108, Jun. 2013.

[81] Y. Shoji, Y. Shirato, and T. Mizumoto, "Silicon Mach–Zehnder interferometer optical isolator having 8 nm bandwidth for over 20 dB isolation," *Japanese Journal of Applied Physics*, vol. 53, no. 2, p. 022202, Feb. 2014.

[82] D. Huang, P. Pintus, C. Zhang, Y. Shoji, T. Mizumoto, and J. E. Bowers, "Electrically Driven and Thermally Tunable Integrated Optical Isolators for Silicon Photonics," *IEEE Journal of Selected Topics in Quantum Electronics*, vol. 22, no. 6, pp. 271–278, Nov. 2016.

[83] W. Yan, Y. Yang, S. Liu, Y. Zhang, S. Xia, T. Kang, W. Yang, J. Qin, L. Deng, and L. Bi, "Waveguide-integrated high-performance magneto-optical isolators and circulators on silicon nitride platforms," *Optica*, vol. 7, no. 11, p. 1555, Nov. 2020.

[84] S. Ghosh, S. Keyvaninia, W. Van Roy, T. Mizumoto, G. Roelkens, and R. Baets, "Adhesively bonded Ce:YIG/SOI integrated optical circulator," *Optics Letters*, vol. 38, no. 6, p. 965, Mar. 2013.

[85] P. Pintus, D. Huang, P. A. Morton, Y. Shoji, T. Mizumoto, and J. E. Bowers, "Broadband TE Optical Isolators and Circulators in Silicon Photonics Through Ce:YIG Bonding," *Journal of Lightwave Technology*, vol. 37, no. 5, pp. 1463–1473, Mar. 2019.

[86] A. W. Fang, H. Park, O. Cohen, R. Jones, M. J. Paniccia, and J. E. Bowers, "Electrically pumped hybrid AlGaInAs-silicon evanescent laser," *Optics Express*, vol. 14, no. 20, pp. 9203–9210, 2006.

[87] G. Roelkens, A. Abassi, P. Cardile, and U. Dave, "III-V-on-Silicon Photonic Devices for Optical Communication and Sensing," *Photonics*, vol. 3, pp. 969–1004, 2015.

[88] O. Zhuromskyy, M. Lohmeyer, N. Bahlmann, H. Dotsch, P. Hertel, and A. Popkov, "Analysis of polarization independent Mach-Zehnder-type integrated optical isolator," *Journal of Lightwave Technology*, vol. 17, no. 7, pp. 1200–1205, Jul. 1999.

[89] M. Fehndrich, A. Josef, and L. Wilkens, "Experimental investigation of the nonreciprocal phase shift of a transverse electric mode in a magneto-optic rib waveguide," *Applied Physics Letters*, vol. 74, no. 20, pp. 2918–2920, 1999.

[90] Y. Shoji, I.-W. Hsieh, R. M. Osgood, and T. Mizumoto, "Polarization-Independent Magneto-Optical Waveguide Isolator Using TM-Mode Nonreciprocal Phase Shift," *Journal of Lightwave Technology*, vol. 25, no. 10, pp. 3108–3113, Oct. 2007.

[91] D. Mathine, "The integration of III-V optoelectronics with silicon circuitry," *IEEE Journal of Selected Topics in Quantum Electronics*, vol. 3, no. 3, pp. 952–959, Jun. 1997.

[92] T. Mizumoto, H. Saito, K. Sakurai, and Y. Shoji, "Wafer Bonding of Magneto-Optic Garnet and its Application to Waveguide Optical Devices," *ECS Transactions*, vol. 3, no. 39, pp. 11–22, Sep. 2007.

[93] K. Sakurai, K. Abe, and T. Mizumoto, "Relaxation of Thermal Stress in Direct Bonding by Partitioning the Bonding Area for Fabrication of Optical Isolator with Semiconductor Guiding Layer," *Japanese Journal of Applied Physics*, vol. 48, no. 11, p. 112401, Nov. 2009.

[94] M.-B. Park and N.-H. Cho, "Structural and magnetic characteristics of yttrium iron garnet (YIG, Ce:YIG) films prepared by RF magnetron sputter techniques," *Journal of Magnetism and Magnetic Materials*, vol. 231, no. 2-3, pp. 253–264, Jun. 2001.

[95] H. Zhou, J. Chee, J. Song, and G. Lo, "Analytical calculation of nonreciprocal phase shifts and comparison analysis of enhanced magneto-optical waveguides on SOI platform," *Optics Express*, vol. 20, no. 8, p. 8256, Apr. 2012.

[96] S. Stanković, D. Van Thourhout, G. Roelkens, R. Jones, J. Heck, and M. Sysak, "Die-to-Die Adhesive Bonding for Evanescently-Coupled Photonic Devices," *ECS Transactions*, vol. 33, no. 4, p. 411, 2021.

[97] S. Stanković, "Hybrid III-V/Si DFB Lasers Based on Polymer Bonding Technology," Ph.D. dissertation, Ghent University, Ghent, 2013.

[98] S. F. G. Reniers, K. A. Williams, J. J. G. M. van der Tol, and Y. Jiao, "An Accurate Characterization Method for Integrated Polarization Converters," *IEEE Journal of Quantum Electronics*, vol. 57, no. 1, pp. 1–6, Feb. 2021.

[99] Y. Xu and J. Xiao, "A Compact TE-Pass Polarizer for Silicon-Based Slot Waveguides," *IEEE Photonics Technology Letters*, vol. 27, no. 19, pp. 2071–2074, Oct. 2015.

[100] D. Dai, Z. Wang, N. Julian, and J. E. Bowers, "Compact broadband polarizer based on shallowly-etched silicon-on-insulator ridge optical waveguides," *Optics Express*, p. 12, 2010.

[101] X. Sun, M. Mojahedi, and J. S. Aitchison, "Hybrid plasmonic waveguide-based ultra-low insertion loss transverse electric-pass polarizer," *Optics Letters*, vol. 41, no. 17, p. 4020, Sep. 2016.

[102] Y. Huang, S. Zhu, H. Zhang, T.-Y. Liow, and G.-Q. Lo, "CMOS compatible horizontal nanoplasmonic slot waveguides TE-pass polarizer on silicon-on-insulator platform," *Optics Express*, vol. 21, no. 10, p. 12790, May 2013.

[103] Y. Jiao, Y. Jiang, and J. van der Tol, "Thermo-optic tuning of wavelength (de)multiplexers on InP membrane," in *Proceedings of the 20th Annual Symposium of the IEEE Photonics Benelux Chapter*, 2015.

[104] D. Huang, "Integrated Optical Isolators and Circulators for Heterogeneous Silicon Photonics," Ph.D. dissertation, UNIVERSITY OF CALIFORNIA Santa Barbara, Santa Barbara, 2019.

[105] F. G. Della Corte, G. Cocorullo, M. Iodice, and I. Rendina, "Temperature dependence of the thermo-optic coefficient of InP, GaAs, and SiC from room temperature to 600 K at the wavelength of 1.5 um," *Applied Physics Letters*, vol. 77, no. 11, pp. 1614–1616, Sep. 2000.

[106] Daoxin Dai, Jian-Jun, and Sailing He, "Elimination of multimode effects in a silicon-on-insulator etched diffraction grating demultiplexer with bi-level taper structure," *IEEE Journal of Selected Topics in Quantum Electronics*, vol. 11, no. 2, pp. 439–443, Mar. 2005.

[107] D. Dai, Y. Tang, and J. E. Bowers, "Mode conversion in tapered submicron silicon ridge optical waveguides," *Optics Express*, vol. 20, no. 12, p. 13425, Jun. 2012.

[108] M. J. Strain and M. Sorel, "Compact Semiconductor Tapers for Deep-to-Shallow Etch Transitions," *IEEE Photonics Technology Letters*, vol. 19, no. 19, pp. 1544–1546, Oct. 2007.

[109] W. K. Burns, A. F. Milton, and A. B. Lee, "Optical waveguide parabolic coupling horns," *Applied Physics Letters*, vol. 30, no. 1, pp. 28–30, Jan. 1977.

[110] Y. Jiao, N. Nishiyama, J. van der Tol, J. van Engelen, V. Pogoretskiy, S. Reniers, A. A. Kashi, Y. Wang, V. D. Calzadilla, M. Spiegelberg, Z. Cao, K. Williams, T. Amemiya, and S. Arai, "InP membrane integrated photonics research," *Semiconductor Science and Technology*, vol. 36, no. 1, p. 013001, Jan. 2020.

[111] T. Mizumoto, Y. Shoji, and R. Takei, "Direct Wafer Bonding and Its Application to Waveguide Optical Isolators," *Materials*, vol. 5, no. 12, pp. 985–1004, May 2012.

[112] X. Luo, Y. Cheng, J. Song, T.-Y. Liow, Q. J. Wang, and M. Yu, "Wafer-Scale Dies-Transfer Bonding Technology for Hybrid III/V-on-Silicon Photonic Integrated Circuit Application," *IEEE Journal of Selected Topics in Quantum Electronics*, vol. 22, no. 6, pp. 443–454, Nov. 2016.

[113] S. Dai, S. A. Bhave, and R. Wang, "Octave-Tunable Magnetostatic Wave YIG Resonators on a Chip," *IEEE Transactions on Ultrasonics, Ferroelectrics, and Frequency Control*, vol. 67, no. 11, pp. 2454–2460, Nov. 2020.

[114] D. O. Ignatyeva, D. Karki, A. A. Voronov, M. A. Kozhaev, D. M. Krichevsky, A. I. Chernov, M. Levy, and V. I. Belotelov, "All-dielectric magnetic metasurface for advanced light control in dual polarizations combined with high-Q resonances," *Nature Communications*, vol. 11, no. 1, p. 5487, Dec. 2020.

[115] X. Luo, Y. Cao, J. Song, X. Hu, Y. Cheng, C. Li, C. Liu, T.-Y. Liow, M. Yu, H. Wang, Q. J. Wang, and P. G.-Q. Lo, "High-Throughput Multiple Dies-to-Wafer Bonding Technology and III/V-on-Si Hybrid Lasers for Heterogeneous Integration of Optoelectronic Integrated Circuits," *Frontiers in Materials*, vol. 2, Apr. 2015.

Acknowledgments

Memories of the past four years come to my mind as I start writing this chapter. Finally, this journey of pursuing a PhD has come to an end, and it is time to express thanks to those who have helped and inspired me.

Jos, thank you for giving me the opportunity to work with you. Your support and guidance encouraged me to do my research independently. Thanks to your open-mindedness and the "open-door policy", I could always walk into your office to share my thoughts without any hesitation. It was a pleasure to have you as my supervisor. Hope you enjoy a comfortable retirement.

Yuqing, from the beginning of my PhD to the end, you were always ready to help, whenever it was needed. I enjoyed having discussions with you during our IMOS meeting, both in the meeting room and in Walhalla. You are a great teacher and friend now, and will be in the future.

Kevin, the PhI group is united under your successful leadership. Although we don't talk much, I benefited a lot from thinking about your feedback on my paper and slides.

I would also like to thank the committee members for providing valuable suggestions and comments, which helped me to improve the quality of this thesis.

Working with the IMOS team was enjoyable. I felt lucky to collaborate with so many experts in the field of photonic integration. Sander, you are more like a big brother of mine, not only because of your age, but also because of your expertise. Having barbecues (especially hongshaorou) and beer at your place made me feel at home. Also, thank you for organizing the unforgettable trip to Valencia. This trip temporarily saved me from the pain of writing this thesis. Yi, I am glad that we started our PhD almost at the same time. I could always share the life in the Netherlands with you. Hope to read your acknowledgment soon. Amir, Vadim, Jorn and Xinran, thank you for all the valuable discussions and guidance. Hope you all the best in your future career. Zhaowei, Yihui, Jasper, David, Ekaterina, Aleksandr and Salim, wish you good luck with your fabrication process and don't forget to make IMOS famous!

Apart from the IMOS team, I would also like thank the members in the big PhI group. Raskto, I enjoyed playing squash with you. Although it made me a bit sad from winning to losing. Joel, I admire your enthusiasm towards work and life. James, your encouragement and drink invitations made my writing process a bit smoother. Martijn, Erwin, Xaveer, Weiming, Victor, and Sylwester, I benefited a lot from all your lectures and presentations. Jolande, thank you for your daily support. Yihui, Wenjing and Xiao, thank you for inviting me to celebrate the Dragon boat Festival together.

The taste of the Zongzi we made is unforgettable. Akanksha, Alessio, Arezou, Bernat, Katia, Irene, Jerald, Kolsoom, Limeng, Lukas, Marc, Marco, Marija, Ozan, Rachel, Tasfia, Tianran, Vikram, Floris, Yunyun, Luding, Florian and Dima, I enjoyed talking with you during coffee break and lunch time.

A bunch of cleanroom work is involved in this thesis. Special thanks to the Nanolab technicians Erik Jan, Tjibbe, Jeroen, Patrick, Stacey. This work cannot be done without your support and guidance.

The help and collaborations outside of the PhI group are also appreciated. Pang, thank you for building the bridge between PhI and me. I truly appreciate your attitude towards research. Yu, Chenhui, Pingzhi, Ece and Hamed, best wishes for your research and career.

Finally, I would like to give a special credit to my wife, Man Li. Thank you for backing me up and bringing the cutest angel to the world during my PhD. May happiness accompany us throughout the journey of life. Wish our daughter growing up happily. Mom and Dad, your endless love and support help me keep moving forward. Love you forever. 爸爸，妈妈，老婆，女儿，我永远爱你们。

Rui Ma 马瑞
November 2022 in Cambridge

List of Publications

Journal articles

- R. Ma, S.F.G. Reniers, Y. Shoji, T. Mizumoto, K.A. Williams, Y. Jiao, and J.J.G.M. van der Tol, "Integrated polarization-independent optical isolators and circulators on an InP membrane on silicon platform," *Optica*, vol. 8, no. 12, pp. 1654-1661, Dec. 2021.

- R. Ma, S.F.G. Reniers, Y. Shoji, T. Mizumoto, Y. Jiao, J.J.G.M. van der Tol, and K.A. Williams, "Demonstration of an on-chip TE-mode optical circulator ," *IEEE J. Quantum Electron.*, in revision.

Conference contributions

- R. Ma, S.F.G. Reniers, Y. Shoji, T. Mizumoto, K.A. Williams, Y. Jiao, and J.J.G.M. van der Tol, "Demonstration of an on-chip optical circulator for TE mode light," EUROPEAN CONFERENCE ON INTEGRATED OPTICS 23 edition, 2022.

- R. Ma, K.A. Williams, Y. Jiao, and J.J.G.M. van der Tol, "Taper Designs for shallow-to-deep etch transitions on an InP membrane on Silicon platform", Proceedings of the 25th Annual Symposium of the IEEE Photonics Benelux Chapter, Mons, Belgium, 2021.

- R. Ma, S.F.G. Reniers, Z.Cao, K.A. Williams, Y. Jiao, and J.J.G.M. van der Tol, "A non-reciprocal polarization converter on InP membrane platform: theory and simulation," in *Proceedings of the Asia Communications and Photonics Conference (ACPC) 2019*, Chengdu, China, Nov. 2019.

- R. Ma, S.F.G. Reniers, Z.Cao, K.A. Williams, Y. Jiao, and J.J.G.M. van der Tol, "Design and simulation of an integrated optical circulator on InP membrane platform", Proceedings of the 24th Annual Symposium of the IEEE Photonics Benelux Chapter, Amsterdam, the Netherlands, 2019.

Patent application

- R. Ma, Y. Jiao, and J.J.G.M. van der Tol,, "An integrated polarization-independent optical non-reciprocal device ". Application number PCT/NL2022/050427.

Curriculum Vitae

Rui Ma was born on April 19, 1993 in Baoji, China. He received his B.Eng. degree from Beijing Institute of Technology, and the M. Sc. Eng. degree from Institute of Semiconductors, Chinese Academy of Sciences in 2015 and 2018, respectively.

He started his doctoral research with the Photonic Integration (PhI) group in the Eindhoven University of Technology in 2018. His research interests include integrated optical nonreciprocal devices, heterogenous integration technology and development of the IMOS platform.

Starting from November 2022, he joined the Centre for Photonic Systems (CPS) in the Universtiy of Cambridge, focusing on the development of co-integration of Si and III-V platforms.